



5-2008

Actuatable Membranes based on Polypyrrole-Coated Vertically Aligned Nanostructures

Benjamin L. Fletcher
University of Tennessee - Knoxville

Follow this and additional works at: https://trace.tennessee.edu/utk_graddiss

 Part of the [Materials Science and Engineering Commons](#)

Recommended Citation

Fletcher, Benjamin L., "Actuatable Membranes based on Polypyrrole-Coated Vertically Aligned Nanostructures. " PhD diss., University of Tennessee, 2008.
https://trace.tennessee.edu/utk_graddiss/383

This Dissertation is brought to you for free and open access by the Graduate School at TRACE: Tennessee Research and Creative Exchange. It has been accepted for inclusion in Doctoral Dissertations by an authorized administrator of TRACE: Tennessee Research and Creative Exchange. For more information, please contact trace@utk.edu.

To the Graduate Council:

I am submitting herewith a dissertation written by Benjamin L. Fletcher entitled "Actuatable Membranes based on Polypyrrole-Coated Vertically Aligned Nanostructures." I have examined the final electronic copy of this dissertation for form and content and recommend that it be accepted in partial fulfillment of the requirements for the degree of Doctor of Philosophy, with a major in Materials Science and Engineering.

Michael L. Simpson, Major Professor

We have read this dissertation and recommend its acceptance:

Mitchel J. Doktycz, E. Ward Plummer, Philip D. Rack, Bin Hu

Accepted for the Council:

Carolyn R. Hodges

Vice Provost and Dean of the Graduate School

(Original signatures are on file with official student records.)

To the Graduate Council:

I am submitting herewith a dissertation written by Benjamin Luke Fletcher entitled "Actuatable Membranes based on Polypyrrole-Coated Vertically Aligned Nanostructures." I have examined the final electronic copy of this dissertation for form and content and recommend that it be accepted in partial fulfillment of the requirements for the degree of Doctor of Philosophy, with a major in Materials Science and Engineering.

Michael L. Simpson, Major Professor

We have read this dissertation
and recommend its acceptance:

Mitchel J. Doktycz

E. Ward Plummer

Philip D. Rack

Bin Hu

Accepted for the Council:

Carolyn R. Hodges

Vice Provost and Dean of the
Graduate School

(Original signatures are on file with official student records.)

**Actuatable Membranes
based on
Polypyrrole-Coated
Vertically Aligned Nanostructures**

A Dissertation
Presented for the
Doctor of Philosophy
Degree
The University of Tennessee, Knoxville

Benjamin Luke Fletcher
May 2008

Copyright © 2008 by Benjamin Luke Fletcher
All rights reserved

Acknowledgements

I would like to thank the many people and organizations that made this dissertation research possible. First, thanks to all of my committee members for your time and for your guidance. Thanks to my advisor, Dr. Michael Simpson, for taking a chance on me many years ago and for providing me with the opportunity to work at Oak Ridge National Laboratory (ORNL). The years of support you and my mentor, Dr. Mitchel Doktycz, have provided me with have made this work possible. Mitch, thanks for your patience and advice. Your door was always open and I took full advantage.

The members of the Molecular Engineering and Nanoscale Technologies (MENT) Research Group have been excellent friends and colleagues. Were it not for Scott Retterer, I might still be working on my dissertation research. You came along at an opportune time and provided invaluable support. Thanks to Jason Fowlkes for all the coffee and for taking FRAP off my hands. Tim McKnight, you've been my sounding board and a fountain of ideas since the beginning. I must also thank Anatoli Melechko for teaching me most of what I know about microfabrication. Thanks for believing in me and for your unwavering support. I owe a debt of gratitude to the staff of the Nanofabrication Research Laboratory, specifically Darrell Thomas and Dale Hensley, for always being there to fix the machines that I broke or found broken. Thanks to Laura Morris Edwards for editing this manuscript and to Gayle Jones for helping organize my committee. I must also mention Kate Klein and Roy Dar, who I came to consider as good friends as well as fellow students. Our shared suffering brought us together.

I would like to acknowledge the Center for Nanophase Materials Science and Oak Ridge National Laboratory where much of this work was conducted. I am also grateful for the support provided by the National Institute of Health, the Tennessee Advanced Materials Laboratory, and the Joint Institute for Advanced Materials Research.

Finally, I want to thank my family and friends for helping me maintain balance in my life and for providing me with many of my more colorful memories of graduate school. You guys are what it's all about. May the circle be unbroken.

Abstract

Nanoporous membranes are an enabling technology in a wide variety of applications because of their ability to efficiently and selectively separate molecules. A great deal of effort is concentrated on developing methods of externally controlling membrane selectivity and on integrating the membranes within multi-scale systems. In this dissertation, synthetic nanoporous membranes that fit the described needs are constructed from vertically aligned nanostructures. Vertically aligned carbon nanofibers and anisotropically etched silicon posts are aligned perpendicular to the substrate and act as obstacles to material flow parallel to the surface. The distances between the outer edges of the nanostructures define the pores of the membranes. Transport through the membranes is controlled by physically selecting species as they pass between the vertically aligned nanostructures. Membrane properties such as permeability and porosity are specified by defining the spatial locations of the membrane components. Subsequent physical and chemical modification of the nanostructures enables further tuning of pore sizes and opens up new methods to controllably modulate the permeability of the membranes. In this dissertation, permeability is externally controlled by electrochemical actuation of the conductive polymer, polypyrrole. Vertically aligned membrane components are coated with the actuatable polymer. Upon electrochemical reduction, the polypyrrole coatings swell in volume, increasing the diameters of the membrane components and decreasing the pore sizes of the membranes. Modulating the physical size of the membrane pores enables size selective transport of species and gating of the nanoscale pores.

Table of Contents

1.	Introduction to Nanoporous Membranes	1
1.1	Literature Review	3
1.1.1	Biological Nanoporous Membranes	3
1.1.2	Synthetic Nanoporous Membranes	9
1.2	Membranes Constructed from Vertically Aligned Nanostructures	17
1.2.1	Vertically Aligned Carbon Nanofibers	18
1.2.2	Silicon Posts	19
1.2.3	Surface Modification by the Electropolymerization of Pyrrole	20
1.3	Scope of Dissertation	21
2.	Vertically Aligned Carbon Nanofiber Membranes	22
2.1	Carbon Nanofibers	22
2.1.1	Physical Properties	23
2.1.2	Synthesis	30
2.1.3	Summary	35
2.2	Membranes Constructed from Stochastic Forests of VACNFs	36
2.3	Conclusions	42
3.	Modification of VACNFs by the Electropolymerization of Pyrrole	44
3.1	Polypyrrole	44
3.1.1	Physical Properties	45
3.1.2	Synthesis	47
3.1.3	Summary	54
3.2	Depositing Nanometer Thin Polypyrrole Films on VACNFs	54
3.2.1	Controlling Polypyrrole Film Growth on Planar Electrodes	55
3.2.2	Controlling Polypyrrole Film Growth on Carbon Nanofibers	59
3.3	Conclusions	64
4.	Actuatable Membranes Constructed from Polypyrrole-Coated VACNFs	65
4.1	Actuation of Polypyrrole	65
4.2	Actuation to Alter the Permeability of VACNF Membranes	71
4.2.1	Actuation of Polypyrrole on Planar Electrodes	72

4.2.2	Actuation of Polypyrrole on VACNFs	75
4.3	Conclusions	84
5.	Capture of Particles within Membrane Structures	85
5.1	Limitations of VACNFs as Membrane Components	85
5.2	Anisotropic Etching	92
5.3	Capture of Particles within Membrane Structures	97
5.4	Conclusions	104
6.	Conclusions	106
	References	109

List of Figures

1-1	Biological cellular membrane	2
1-2	Staphylococcal α -hemolysin transmembrane pore	4
1-3	α -hemolysin chemical valve	5
1-4	MscL channel protein valve	6
1-5	Shaker K ⁺ channel protein valve	7
1-6	DNA membrane	8
1-7	Polycarbonate track etched membrane	10
1-8	Ion beam sputtering process	11
1-9	Electrical double layer potential profiles	12
1-10	Porous alumina membranes and carbon nanotubules	14
1-11	Carbon nanotube membrane	15
1-12	VACNF membrane structure	18
1-13	Gold-coated silicon posts	19
1-14	Carbon nanofibers modified with PPy	20
2-1	TEM of a VACNF	23
2-2	Graphene layers inside a VACNF	24
2-3	Atomic structure of a VACNF	25
2-4	Atomic structure of a grapheme layer	26
2-5	I-V characteristics of a VACNF forest	27
2-6	Cells impaled on a VACNF array	29
2-7	TEMs of a growing nanofiber	31
2-8	PECVD growth process	32
2-9	Kinked nanofibers	34
2-10	Horizontal growth of carbon nanofibers and nanocones	35
2-11	Fabrication process for VACNF cell structures	37
2-12	VACNF cell structures	38
2-13	Fluorescence micrographs of VACNF cell structures	39
2-14	VACNF membrane containment limits	40
2-15	Multiple reagents	40
2-16	Caged <i>E. Coli</i>	41
3-1	Pyrrole monomer	45
3-2	Electron orbitals of pyrrole monomer	45

3-3	Polypyrrole	46
3-4	Electron energy diagrams	46
3-5	Electrochemical polymerization reactions	48
3-6	Chemical polymerization reaction	49
3-7	Three electrode electrochemical cell	50
3-8	Band ultramicroelectrode	53
3-9	PPy film thickness versus polymerization reaction parameters	57
3-10	Electron micrograph and AFM scans of individual VACNFs	60
3-11	Arrays of VACNFs modified with PPy	61
3-12	Individual VACNFs modified with PPy	62
3-13	Polymerization time versus film thickness on VACNFs	63
4-1	Oxidized PPy	66
4-2	Doped and undoped PPy	67
4-3	CVs of PPy	69
4-4	Hysteresis effect	70
4-5	Actuated PPy	72
4-6	Actuation characteristics of PPy	73
4-7	VACNF membrane structure modified with PPy	75
4-8	Fabrication of VACNF membrane structures	76
4-9	Array of VACNF membrane structures	77
4-10	PPy coated VACNF membrane	77
4-11	Experimental setup	78
4-12	Fluorescence micrographs of VACNF membrane structures	79
4-13	PPy actuation induced fluid pumping	80
4-14	Effects of PDMS channel width	81
4-15	50 nm bead VACNF actuation experiment	82
4-16	Limits of VACNF-PPy membrane actuation	83
5-1	Membrane constructed from a stochastic forest of VACNFs	86
5-2	Electron beam pattern	87
5-3	Variability in VACNF growths	88
5-4	Effects of PECVD chamber conditions on VACNF growths	89
5-5	Effects of substrate heater on VACNF growths	90
5-6	VACNFs grown from electron beam pattern	91
5-7	Etch profiles	92

5-8	Step planes from a Bosch etch	93
5-9	Residual polymer from a cryogenic etch	94
5-10	Black silicon	95
5-11	Etch taper	96
5-12	Silicon post membrane structure	97
5-13	Integrated device	98
5-14	Device attached to printed circuit board	100
5-15	PPy modified silicon posts	101
5-16	50 nm bead silicon post actuation experiment	102
5-17	Limits of silicon post membrane structures	102
5-18	Protein capture	103

Chapter 1

Introduction to Nanoporous Membranes

Biological cells are impressive nanoscale machines, capable of performing a wide range of functions using a relatively small number of components. Cells can replicate themselves, sense subtle changes in their environment, communicate with other cells, and synthesize a diverse array of nanomaterials [23-26]. In addition to functional versatility, cells operate at higher efficiencies relative to synthetic nanoscale systems. The DNA of an *Escherichia coli* cell contains roughly 4.6 million base pairs or the equivalent of 9.2 million bits of memory. By contrast, an equivalent area of silicon ($2\ \mu\text{m}^2$) can contain approximately 400 bits of memory or $1/10000^{\text{th}}$ the capacity of an *E. Coli* cell. Furthermore, if the ligation of two DNA molecules is considered a single operation and the Gibbs free energy of this operation is $G = -8\ \text{kcal/mol}$ [27, 28], then 1 J is sufficient for approximately 2×10^{19} operations [29]. This energy efficiency approaches the theoretical maximum dictated by the second law of thermodynamics (34×10^{19} operations per joule at 300 K [30, 31]) and far exceeds the efficiencies of existing supercomputers (10^9 operations per joule).

The functionality gap between synthetic and natural systems cannot be resolved simply by reducing the scale of synthetic components. At a certain point, these components will approach the size of atoms or small clusters of atoms and further reductions will become unfeasible. New approaches to organize and utilize nanomaterials must also be pursued. It follows that nanoscience efforts should focus both on the synthesis of nanomaterials (scale) and their organization into ensembles (complexity).

One logical starting place in emulating cell-like complexity is to duplicate the functionality of the cellular membrane. The cell membrane defines the extents of the biological cell while encapsulating and protecting the cell's internal machinery from the surrounding environment. Furthermore, the small volume of the cell allows for efficient diffusion mediated transport between compartments of the cell, biologically significant

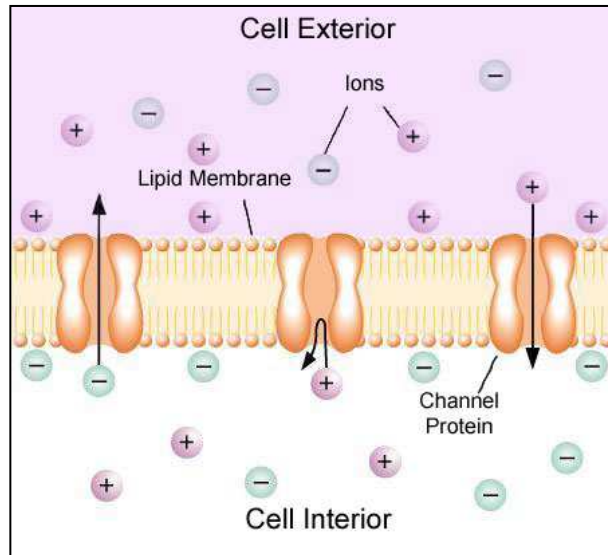


Figure 1-1) A graphical depiction of a simplified biological cellular membrane. Ion channel proteins and the lipid membrane are shown.

changes in concentrations with the production of relatively few molecules, and increased influence of stochastics in cellular function [32, 33].

In addition to small volume containment, the membrane acts as a mediator between the cell interior and the exterior. It is a semipermeable lipid bilayer decorated with channel and transport proteins that regulate molecular transport (see Figure 1-1) [34]. Regulation of transport across the membrane allows cells to modulate, respond, and adapt to changes in their local environment. Transport is dictated by precisely assembled pore structures and selectivity is enabled by subtle changes in protein structure, charge, and surface energy.

The cell membrane performs the functions of small volume containment and biochemical trafficking in parallel, integrating functionality on the nanoscale. To realize this ideal requires precise engineering of nanoscale features within microscale systems. Nanoporous synthetic membranes must also be able to selectively control the transport of molecular species between the encapsulated area and the surrounding environment. Current approaches to address these challenges are briefly reviewed.

1.1 *Literature Review*

Nanoporous membranes are an enabling technology for a variety of applications including separations [35-37], molecular sensing [38-41], and drug delivery [42-44]. The synthetic nanoporous membranes that enable these applications can be classified by the composition of their nanopores. In this dissertation, gate valves are defined as devices for turning on and off molecular transport through nanopores in response to an external stimulus. Several approaches utilize naturally occurring membrane proteins to act as nanoscale gate valves. These proteins have been modified to change between open and closed states in response to specific chemical, electrical, and mechanical stimuli. Alternatively, synthetic analogues that mimic this gating functionality are being developed. Nanoporous membranes have been synthesized using porous alumina [45], by track etching nanopores in polymer films [46, 47], from carbon nanotubes embedded in thin polymer films [48, 49], by ion beam etching of oxide films [50, 51], and using soft lithography [52]. Membranes featuring both types of nanopores are discussed.

1.1.1 *Biological Nanoporous Membranes*

Staphylococcal α -hemolysin (α HL) is a pore-forming protein synthesized by *Staphylococcus aureus*. It is a monomeric water-soluble polypeptide chain which forms homooligomeric pores in lipid bilayers (see Figure 1-2) [53]. The internal diameter of the pore is 1 to 2 nm and molecules as large as 3000 Da can pass through. In natural systems, this pore is only weakly selective for anions versus cations and remains open in normal circumstances [54]. These characteristics are what make α HL a desirable system for protein reengineering. Preferences for the transport of molecules of defined charge, size, and shape can be introduced without disturbing the functionality of preexisting protein features. For instance, it is possible to introduce gating in response to a stimulus without having to eliminate the features that control voltage- or ligand-dependent activation [55].

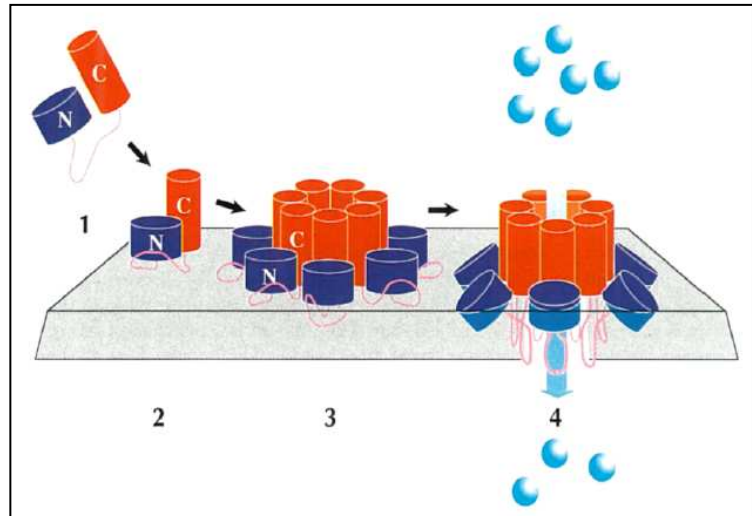


Figure 1-2) Scheme for the assembly of a staphylococcal α -hemolysin transmembrane pore. **(1)** The amino-terminal (N, blue) and carboxy-terminal (C, red) domains of α -hemolysin are separated by a glycine-rich polypeptide chain (pink loop). **(2)** α -hemolysin binds to the lipid bilayer membrane as a monomer, **(3)** which then aggregates to form an oligomeric prepore complex. **(4)** The prepore complex converts to a heptameric pore, allowing molecules up to 3 kDa (blue spheres) to pass through.

Reproduced from Walker *et al.* [13].

Additional benefits for using α HL include its ease of production (gram amounts are readily produced), the simplicity of the polypeptide chain (contains just 293 amino acids with no cysteine and few histidine residues) [56], and its ability to self-assemble on phospholipid vesicles [57], on planar bilayers [54], and in solutions of deoxycholate [58]. Membranes self assemble in the form of two-dimensional sheets of pores and lipids. Site specific chemical modification is enabled by introducing amino acids, such as cysteine and histidine, to the α HL polypeptide chain (pink loops in Figure 1-2).

Three modes gating α HL pores have been developed including by biochemical, chemical, and physical means. The first successfully developed α HL gate valve was a protease-activated biochemical trigger [59]. Molecular complementation mutagenesis was used to generate overlaps in the central loop of α HL. To activate the trigger, redundant pieces of the polypeptide chain in the overlap region of the loop were removed by limited proteolysis in response to the presence of a stimulus. This rendered the pore impermeable to enzyme-specific protease.

Chemical switches were created by placing histidines into the central loop of α HL [60]. The activity of the protein was upset by divalent cations binding at this site (see Figure 1-3). Zn^{2+} and certain other divalent cations can bind to the histidines, blocking the transmembrane channel of the pore. To turn activity of the pore-forming protein back

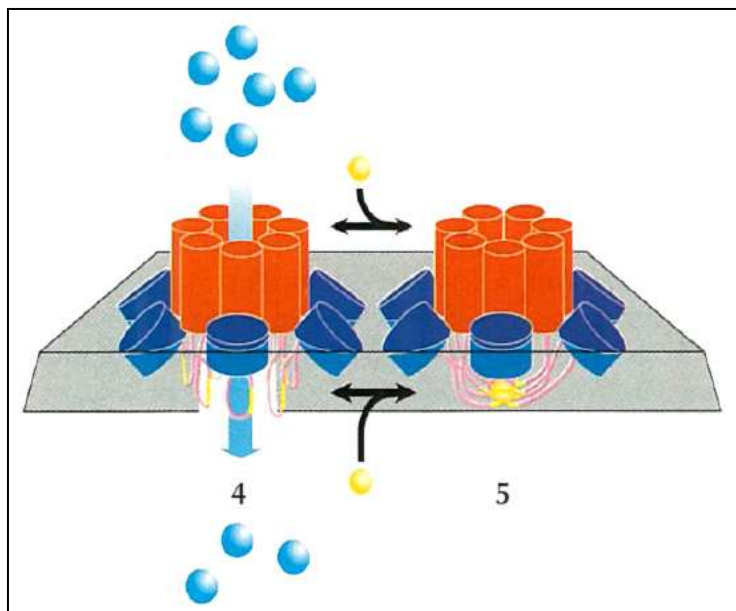


Figure 1-3) Scheme for the blockade of an α -hemolysin pore by Zn^{2+} . **(4)** The histidine residues (yellow part of polypeptide chain) form part of the transmembrane pore. **(5)** The pore can be reversibly blocked by Zn^{2+} (yellow spheres) added from the cis or trans side of the membrane. Reproduced from Walker *et al.* [13].

on, the chelating agent ethylenediamine tetraacetic acid (EDTA) was introduced. EDTA bound to the metal ions attached to the central loop of α HL and sequestered them, clearing the blockage.

Light has been used as a physical stimulus to activate molecular transport through α HL pores. The water-soluble reagent 2-bromo-2-(2-nitrophenyl)acetic acid (BNPA) blocks sulfhydryl groups with the photolabile α -carboxy-2-nitrobenzyl (CNB)-protecting group [61]. When α HL was derivatized with BNPA, pore-forming activity was lost. Exposure to uv irradiation led to regeneration of the sulfhydryl groups and the restoration of pore-forming activity [62]. Using this physical trigger allowed for tight spatial and temporal control with remote activation. Two photon scanning photochemical microscopy was used to activate spots 0.3 μm wide and 1 μm high [63].

A significant advantage of α HL is that it can be chemically engineered using advanced molecular biology techniques such as mutagenesis [64]. It is possible to make targeted local changes to the structure of the protein, enabling sensitivity to a broad range of chemical, biochemical, and physical stimuli. The pores formed by α HL are excellent gateable nanopores, controllable by a variety of external stimuli. However, this is not the only system for producing biological nanopores.

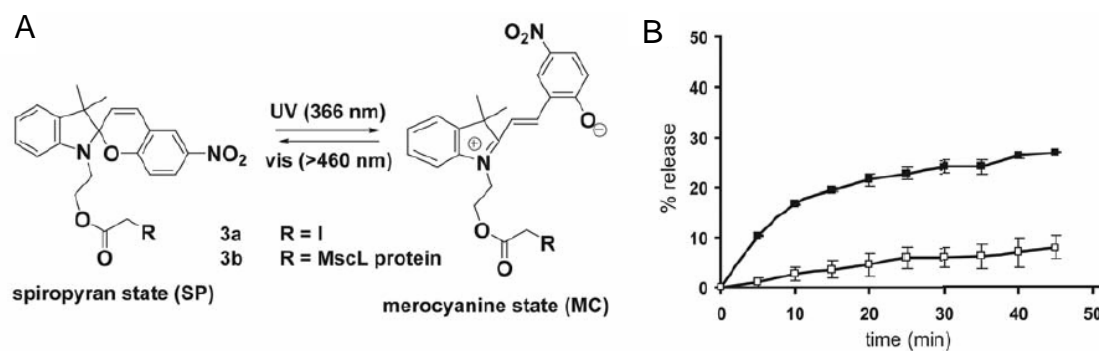


Figure 1-4) A reversible photoswitch, constructed from the MscL channel protein, can be opened and closed by optical signals. **A)** Light-induced switching of compound 3. **B)** Reversible operation of the MscL switch. Open squares represent fluid release without light stimulus and solid squares represent continuous light-actuated MscL-mediated release. Bars indicate error to one standard deviation. Reproduced from Kocer *et al.* [22].

Gateable biological nanopores were created by appending an addressable photosensitive gate to a naturally occurring channel protein [22]. The mechanosensitive channel of large conductance (MscL) from *Escherichia coli* is a relatively large, nonselective pore about 3 nm in diameter. The protein is a homopentamer with two transmembrane helices, M1 and M2, per subunit. The actual pore is formed by five M1 helices. In order to couple a photosensitive actuator to the charge-sensitive portion of the channel, the glycine residue at the 22nd amino acid position in the M1 helices was replaced by cysteine, an amino acid not present anywhere else in MscL. A cysteine-selective alkylating reagent composed of photosensitive spiropyran molecules was attached to the cysteine sites. Illumination at $\lambda = 366$ nm resulted in an opening of the photochemical ring to a polar merocyanine form (see Figure 1-4A). Exposure to visible light (>460 nm) induced a ring-closing reaction, restoring the protein to its original, uncharged state. It should be noted that a lag of about 2 minutes existed between applying the light stimulus and activating the protein pore to an open state. Once activated, the pore remained open without further stimulus (see Figure 1-4B). The channel switched off much more rapidly when irradiated with visible light (within seconds). The rapid deactivation, contrasted with the slow activation, suggests a critical polarity necessary for ion conduction through the pore.

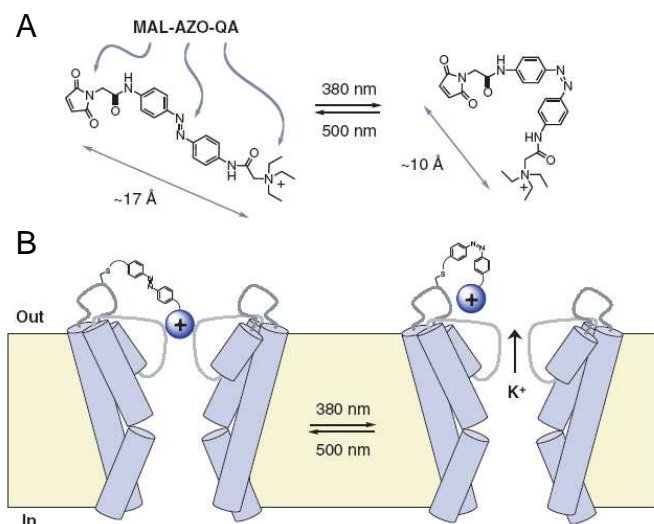


Figure 1-5) Photoisomerization of the tetraalkyl ammonium group gates ionic currents through the Shaker K^+ channel. **A)** The core of the ammonium group, maleimide azo quaternary ammonium (MAL-AZO-QA), shortens by about 7 Å upon photoisomerization. **B)** MAL-AZO-QA blocks ion flow in the *trans* configuration and allows flow in the *cis* configuration. Reproduced from Banghart *et al.* [21].

A similar photoactuated gate valve was synthesized using a light-switchable Shaker K^+ ion channel [21]. These ion channels are composed of voltage dependent channel proteins that form a pore about 3 nm in diameter. Cysteine was introduced to the channel at a site exposed to the extracellular solution (see Figure 1-5). A blocker compound, composed of a tetraalkyl ammonium group appended to a photoisomerizable arm, was covalently attached to the sulfhydryl groups in the exposed cysteine [65]. In the *trans* configuration, the appended blocker was allowed access to a binding site on the opposite side of the external mouth of the channel, closing the pore. Upon irradiation at 380 nm, *trans-cis* isomerization occurred and the blocker could no longer reach the opposite binding site. The pore was opened and flow was allowed through. Irradiation at 500 nm caused *cis-trans* isomerization. The blocker would reattach to the opposite side of the channel, closing the valve and blocking flow again. There was a lag of about 2 minutes between stimulus and activation. Upon activation, the pore was also not entirely closed but ~90% blocked.

The ion channel formed by the peptide gramicidin has been modified to respond to changes in voltage [66, 67]. A channel is formed when two gramicidin monomers associate in an N-terminal to N-terminal fashion. The structure of the peptide provides a pore 28 Å long and 4 Å in diameter [68-70]. Like the other biological nanopores, gramicidin pores readily incorporate within lipid membranes. To enable voltage

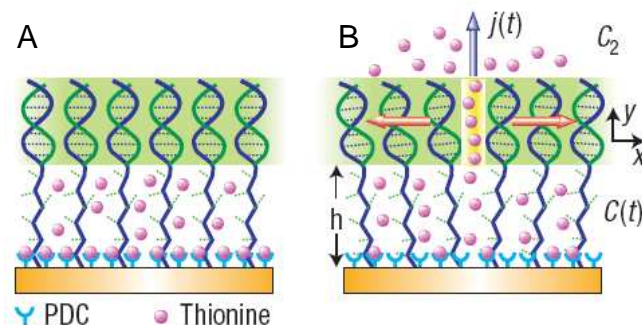


Figure 1-6) A) Schematic of a DNA membrane tethered to a 1,4-phenylenediisothiocyanate (PDC) self-assembled monolayer. **B)** Single-file transport of thionine molecules through a transiently opened DNA channel. Reproduced from Mao *et al.* [2, 3].

sensitivity, the C-terminal ends linked to the gramicidin backbone via carbamate linkages were derivatized with amino acid groups. Carbamate bonds are known to have barriers to rotation on the order of 55 – 70 kJ/mol [71, 72]. Applying a potential of -200 mV was sufficient to initiate *cis-trans* isomerizations of the carbamate linkages and open the pore. To close the pore, -200 mV was again applied to initiate *trans-cis* isomerizations. Gating of the channel was enabled by changes in the location of the protonated amino acid groups after isomerizations. The responses were almost immediate, taking only a few seconds to change between open and closed states. However, the pores were not entirely closed by the isomerizations. Instead, the difference in permeability between open and closed states was about 50%.

Nanopores have been synthesized from short segments of double-stranded DNA. In this system, DNA arrays, with an active DNA nanocompartment nanostructure and channel diameters of $\sim 9 - 20 \text{ \AA}$, were embedded within a 1,4-phenylenediisothiocyanate (PDC) self-assembled monolayer [2]. The DNA channels were shown to gate in response to the level of concentration of thionine molecules in solution. Higher concentrations of thionine led to increases in stress on the DNA channel from permeating thionine molecules acting on the inner surface. At a critical level of stress, the DNA channels opened to allow transport through the membrane (see Figure 1-6). Gating was induced by altering the concentrations of thionine. Actuation was relatively difficult to control, with significant changes in thionine concentration taking ~ 30 min to occur.

In applications such as molecular sensing, biological nanopores remain the gold standard by which other nanopores are judged. A major advantage of these kinds of membranes is their ability to self-assemble with little direction during synthesis. These

nanoscale structures are produced using relatively simple techniques and readily available equipment. However, membranes constructed from biological components are relatively fragile compared to synthetic components. They are damaged by relatively low levels of mechanical stress and are extremely sensitive to changes in pH, temperature, and pressure. As a result, membranes featuring biological components can not survive most conventional micro- and nano-scale fabrication processes. This makes their incorporation within multi-scale systems and devices difficult. Further, biological nanopores provide pores of fixed dimensions, limiting their versatility and application. Synthetic analogues that mimic the gating functionality of biological nanopores are being developed as alternatives.

1.1.2 *Synthetic Nanoporous Membranes*

Nanoporous membranes have been synthesized from a variety of materials including from porous alumina [73], by track etching nanopores in polymer films [46, 74], from carbon nanotubes [75, 76], by ion beam etching oxide films [20, 77], and using soft lithography [52]. A polymer-protein hybrid membrane was synthesized from channel proteins incorporated within polymer vesicles [78]. The polymer vesicles were synthesized from a reactive amphiphilic ABA triblock copolymer comprised of a flexible, hydrophobic poly (dimethylsiloxane) (PDMS) middle block and two water soluble poly (2-methyloxazoline) (PMOXA) side blocks. The PMOXA-PDMS-PMOXA triblock copolymer exhibited similar phase behavior to that of bilayer-forming lipids like lecithin [79], forming vesicular structures in dilute aqueous solutions. The size of the vesicles can be controlled in the range of 50 to 500 nm in diameter. An outer membrane protein, OmpF, found in the cell wall of Gram-negative bacteria was incorporated within the copolymer matrix. While the tendency of the copolymer to form membrane-like superstructures closely resembles the behavior of lipid molecules, the copolymer membranes were much thicker than lipid membranes (10 nm vs 3-5 nm). The flexibility of the polymer molecules allowed them to adapt to the dimensions of the OmpF membrane proteins. OmpF is a channel protein that can be closed by applying a transmembrane voltage [80, 81]. To demonstrate this phenomenon, a relatively large enzyme, β -lactamase, was encapsulated within the polymer-protein hybrid vesicles. The OmpF channels were opened by applying a Donnan potential across the vesicle shell and β -lactamase was

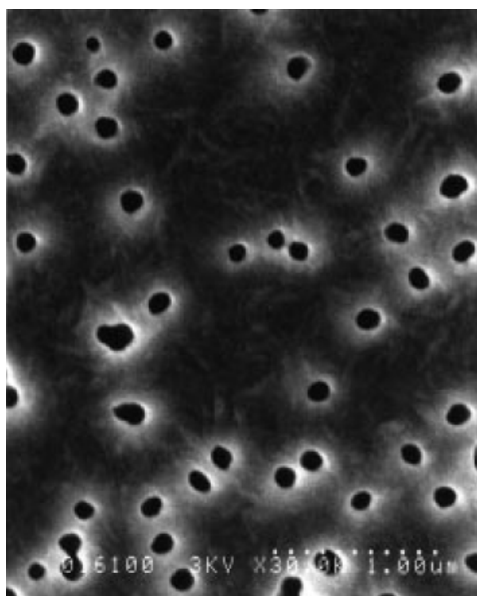


Figure 1-7) Scanning electron micrograph of a Zn-coated polycarbonate track etched membrane. The membrane is 7 μm thick, featuring pores with an average diameter of 200 nm. Reproduced from Kemery *et al.* [19].

released. There was a lag time between the application of the transmembrane voltage and the opening of the protein channels of about 6 minutes.

A common technique of synthesizing nanoscale membranes is to bore holes through synthetic materials. Three methods to do this are by anodic oxidation, track etching, and ion beam etching. Porous alumina membranes with high pore densities and parallel non-intersecting pores can be prepared by anodic oxidation. In this process, a piece of aluminum acts as the anode in an electrolytic cell containing an electrolyte, such as phosphoric acid. A porous film forms on the surface of the aluminum anode when a voltage is applied. The pore size and pore density of the film is determined by the charge passed through it. A voltage reduction sequence is then conducted to detach the film from the aluminum electrode. Alumina membranes featuring pores with diameters as small as 10 nm are commercially available (US Filter, FL).

Track etching polymer films is a two step process [46, 47]. First, the polymer film is irradiated with high-energy particles generated by a nuclear reactor or other radiation source. These particles can be α -particles, accelerated heavy ions, or thermal neutrons [82-84]. The high-energy particles pass through the polymer film, breaking chains and leaving damaged tracks behind them. Next, the polymer film is etched in a solution that etches along the tracks left by the high energy particles. Etching the polymer produces

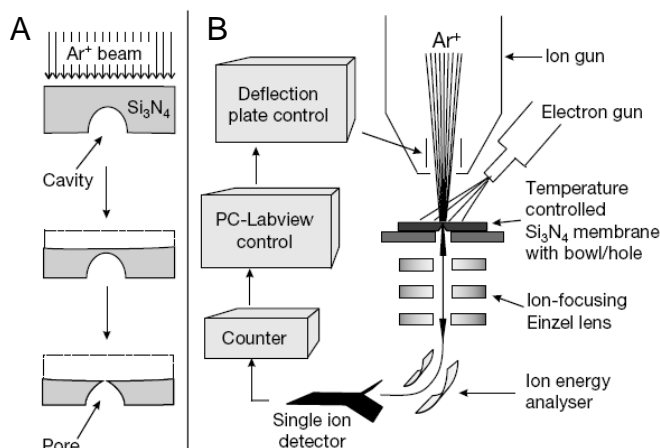


Figure 1-8) Strategy to make nanopores using argon ion-beam sputtering. **A)** Sputtering removes material from a Si_3N_4 membrane. **B)** The feedback controlled ion-beam sculpting apparatus. Reproduced from Li *et al.* [20].

channels or pores through the film (see Figure 1-7). The number and diameter of these pores can be controlled by the exposure time to the radiation source and by the time in etching solution. Holes have been etched in polycarbonate the width of a single ion (~ 10 nm) [85].

Ion beams can be used to carve holes through oxide films [50, 51]. In this process, massive ions with energies of several thousand electron-volts impinge on the oxide film surface, causing sputtering of surface atoms at a rate of approximately one atom per incident ion [86]. An ion detector is positioned below the substrate to count the ions that are transmitted through the oxide. This provides a feedback mechanism to help determine when to stop the sputtering process (see Figure 1-8). Other process parameters such as the sample temperature, the time the beam is cycled between on and off, and the ion beam flux are also carefully monitored. Pores have been etched through Si_3N_4 films with diameters as small as 5 nm using this method.

Membranes synthesized from porous alumina, track etched polymers, and ion beam etched oxides share many similarities in design. Nanoscale pores are bored through synthetic materials in a relatively monodisperse distribution of pore diameters at preselected pore densities. Because of their similarities, several gating strategies have been developed that are adaptable to each of these three synthetic nanoporous membranes. One approach exploits a phenomenon caused by electric double layers and the nanoscale dimensions of the pores [19, 87]. The important parameter to consider is the product of the pore radius, a , and the inverse Debye length, κ . When $\kappa a \leq 1$, an

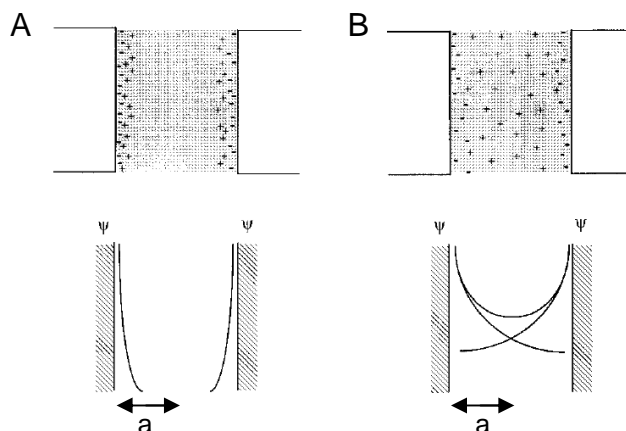


Figure 1-9) Schematic of the electrical double layer potential profiles within a nanopore at extreme conditions where A) $ka \geq 1$ and B) $ka < 1$. Reproduced from Kemery *et al.* [19].

electrical double layer extends across the entire pore (see Figure 1-9). Selectivity is electrochemical and according to the charge of each molecular species passing through the electric double layer. The double layer can be extended entirely across the pore, limited to the walls, or exist anywhere in between by adjusting the ionic strength of the buffer solution. κ^{-1} is very large in aqueous systems, so the double layer can only span across the entire pore for diameters of several hundred nanometers or less. Gating of nanoscale pores can be achieved by altering the surface charge density of the pore walls. One method of doing this requires gold to be electrolessly plated onto the pore walls. Propanethiol is then chemisorbed to the gold to protect it from adsorption of ions that could result in charges on the pore walls. Charge selectivity is then manipulated by applying electrical potentials to the gold [88]. Applying a positive potential limits the electrical double layer to the channel walls (see Figure 1-9A) and opens the pores to the flow of anions. Applying a negative potential extends the electrical double layer across the channel (see Figure 1-9B) and closes the pores. Switching between open and closed states is rapid (>1 s) and, when closed, the flux through the pore is virtually zero.

Electrolessly plating gold to these nanoporous membranes enables other approaches to introduce gating functionality. Self-assembled monolayers (SAMs) were formed from functionalized alkanethiols onto gold coated nanopores. These SAMs imparted a high pH-dependence to the membrane [88, 89]. The charge of the functional head group of the thiol (carboxylic acid) is pH dependent. Changes in solution pH have a profound effect on the electrostatic interactions between the pore walls and ionic species

within the pore channel. As a result, transport of species within the surface-modified pores is highly dependent on the pH. For instance, at the isoelectric point of the protein, bovine serum albumin, electrostatic interactions between the protein and the membrane surface were minimized and the flux of the protein was maximized. Changing the external solution pH altered the surface charge of the pores and the charge of the proteins. This, in turn, altered the strength of the electrostatic interactions between the proteins and the membrane surface and, thus, the flux of protein flow through the pore. Gating was achieved by controlling the external pH to impart changes in the charge of the SAMs. Flux of bovine serum albumin was three times higher in experiments where the solution was acidic (pH = 4.7) than in experiments where the solution was basic (pH = 8.35).

DNA hairpins were attached to the inside pore walls of gold plated polycarbonate template membranes to impart molecular recognition capabilities and single base transport selectivity [90]. The membranes were commercially available filters, 6 μm thick, with 30 nm diameter pores at a density of 6×10^8 pores cm^{-2} . Electrolessly plating gold onto the membranes reduced the pore diameter to 12 ± 2 nm. The DNA hairpins contained complementary base sequences at each end of the molecules. This made the DNA sensitive to complementary strands that were almost perfect complements, with few to no mismatches. The DNA hairpins were covalently tethered to the inner walls of the gold plated pores. In experiments where perfect complement DNA (PC-DNA) was flowed through the pores of the membrane, flux was shown to be much higher through membranes functionalized with the hairpin DNA. The hairpin DNA acted as a molecular recognition agent to facilitate transport of the PC-DNA through the pores. Flux was ~6 times higher through functionalized membranes as opposed to control membranes. The increased flux of the PC-DNA was likely due to sequential binding and unbinding events with the hairpin DNA. Hybridization and dehybridization reactions between the permeating PC-DNA and the hairpin DNA facilitated transport through the membrane pores.

Controlled transport of water through a nanoporous alumina membrane was demonstrated by modifying the surface of the membrane with light-sensitive photochromes and hydrophobic molecules [91]. An alumina membrane was first derivatized with an alkoxysilane, 3-aminopropyl-triethoxysilane. Then, the photosensitive molecule, spiropyran, was covalently attached to the surface bound amino groups. Spiropyran is a well known photochrome that reversibly isomerizes between metastable

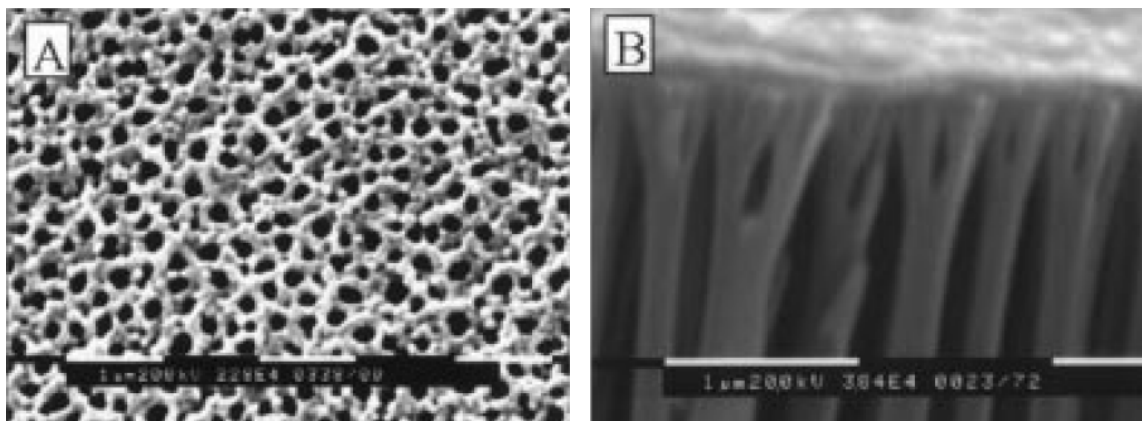


Figure 1-10) SEM images of **A)** the face of the membrane after deposition of carbon and **B)** the cross section of carbon nanotubes after dissolution of the alumina membrane. The pores are 200 nm in diameter on average. Reproduced from Che *et al.* [18].

states under light stimulation. The speed of photoinduced switching was a function of the light flux employed. Irradiation by UV light (337 nm, 3.7 mW/cm²) resulted in photoisomerization to a merocyanine form within 10 minutes. Reversion to the native spiro form occurred within 10 minutes, at ambient temperatures by exposure to visible light (532 nm, 5.8 mW/cm²). The spiro form of spiropyran is relatively hydrophobic while the merocyanine form is relatively hydrophilic. These changes in hydrophobicity enabled gating of the nanoscale pores by light. The amount of impedance to the flow of water through the pores was dependent on the metastable state of the tethered spiropyran. When the majority of tethered spiropyran was in the native spiro form, impedance was found to be ~1 MΩ. While when the majority was in the merocyanine form, the impedance was ~36 Ω.

An alternative approach to synthesizing nanoporous membranes combines two nanostructured materials: carbon nanotubes (CNTs) and porous alumina membranes [18, 92]. Alumina membranes were used as a template for the synthesis of CNTs in a chemical vapor deposition (CVD) process. Alumina was placed in a CVD reactor and heated to 900 °C. Ethylene gas was then introduced to the chamber and decomposed within the pores and on the faces of the alumina membrane to form the carbon nanotubes. The thickness of the deposited carbon was controlled by deposition time. A 30 minute deposition time resulted in 20 nm diameter hollow carbon nanotubes that coalesce as they extend down the membrane into 200 nm diameter nanotubes (see Figure 1-10). Actuation was achieved by electrochemical lithium intercalation and deintercalation. During intercalation, the carbon in the alumina membrane flexes

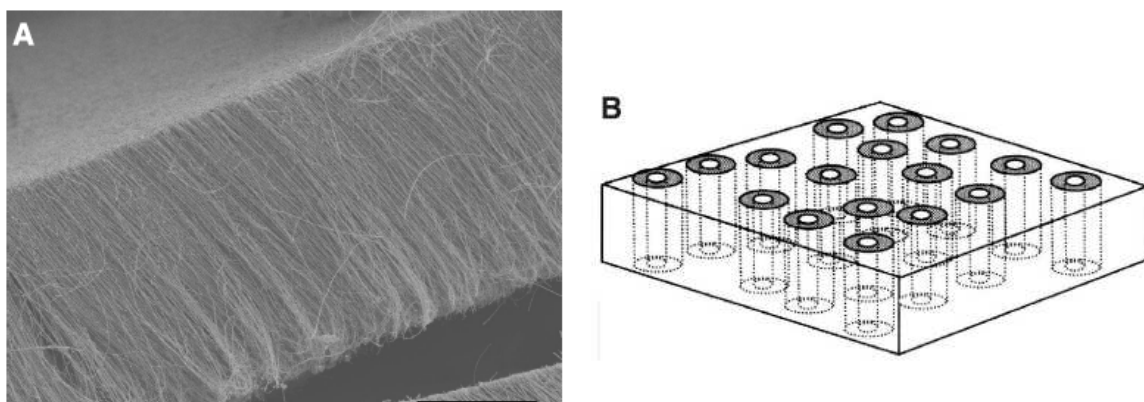


Figure 1-11) A) SEM image of an as-grown, dense, multiwalled CNT array produced in an Fe-catalyzed chemical vapor deposition process (scale bar is 50 μm). **B)** Schematic of the target membrane structure, with polymer embedded between the CNTs. Reproduced from Hinds *et al.* [17].

proportional to the applied potential. Electrochemically deintercalating the carbon returns it to its relaxed state. The carbon was shown to expand and contract by $\sim 12\%$ in volume.

Carbon nanotubes have been used in other strategies to produce nanoporous membranes. Nanotubes have been embedded in a polystyrene matrix to form membrane structures with nanometer-scale pores [17, 93]. The CNTs were grown on a quartz substrate in a CVD process using a ferrocene-xylene-argon-hydrogen feed at 700 $^{\circ}\text{C}$. A mixture of polystyrene and toluene was spin coated over the surface and dried at 70 $^{\circ}\text{C}$. Hydrofluoric acid was then used to remove the CNT-polymer composite from the quartz substrate (see Figure 1-11). The density of CNTs embedded in the film was $6 (\pm 3) \times 10^{10}$ CNTs per cm^2 with about 70% of these CNTs functional as nanoscale pores. The membrane had an average pore diameter of 7.5 (± 2.5) nm, a diffusion length of 5 (± 1) μm , and a calculated permeability of 2.4 (± 1.9) $\mu\text{mol}/(\text{m}^2\text{s Pa})$. Excess polymer was removed and the tips of the CNTs were opened in a H_2O plasma-enhanced oxidation process. The newly opened tips terminate in carboxyl end groups that readily functionalize with a wide range of biomolecules [94-96]. To demonstrate, a selectively functional molecule, (+)-biotinyl-3,6 dioxaoctanediamine, was reacted with the end groups by a carbodiimide-mediated reaction. Transport through the pores was switched off when streptavidin bound to the functionalized molecule at the end tips of the CNTs and was switched on when the streptavidin was released by incubating in a biotin buffer solution. Flux through the nanotubes was 4.8 $\text{nmol cm}^{-2} \text{h}^{-1}$ when streptavidin was bound to the functionalized tips and 0.2 $\text{nmol cm}^{-2} \text{h}^{-1}$ when it was not.

Other polymer membranes are commonly synthesized using soft lithography techniques. Channels and porous membranes have been formed by micromolding

PDMS. In this procedure, patterns are transferred (using micro- or nano- scale lithography) and etched onto a substrate (usually silicon). Next, degassed PDMS resin is poured over the patterned substrate and cured. The resin cures around the etched pattern on the substrate and leaves an impression in the resin. A wide variety of different patterns can be transferred in this way. Membranes formed from PDMS have been described with pores as small as 30 nm [97, 98]. One strategy to control transport through these PDMS pores incorporates a metal electrode within the sidewalls of the pores. By applying a voltage, it is possible to extend the electrical double layer across the entire pore width, allowing for separation by ionic species. Response times to applied stimulus are almost immediate (< 1 s). Another approach to achieve gating of PDMS pores uses the thermal expansion properties of certain microspheres (Expancel 820DU). The microspheres are spun into the PDMS resin prior to curing so that they are evenly distributed. Microspheres ~ 20 nm in diameter experience a maximum volume change of $\sim 270\%$. When incorporated within the PDMS matrix, PDMS pores and channels open and close according to the shrinking and swelling of the embedded microspheres. Volume changes are induced by applying power to the PDMS through an external electrode, thus heating the microspheres. Response times are proportional to the applied power and range from 3 to 45 seconds.

The strategies used to impart gating functionality on synthetic nanoporous membranes can be classified in broad categories according to the type of selectivity achieved: chemical, electrochemical, or physical. Gating by chemical selectivity typically involves functionalization of the surfaces of the nanopores with a reactive molecule. The molecules impart chemical selectivity to enable gating of flow through the nanopores. The reactive molecules will bind specific species at the entrance of the nanopore channels to block or allow flow through them. Strategies that use electrochemical selectivity to enable gating take advantage of a fluidic phenomenon that arises at the nanoscale. At this scale, the widths of the fluidic channels are comparable to the size of the electric double layer that develops around the fluidic channel walls. In cases where the electric double layer extends entirely across the width of the fluidic channel, flow through the channel is selective according to the charge of the permeating species. Electrochemical gating strategies take advantage of this phenomenon by controlling the extent to which the electric double layer extends across the channel. This is achieved by changing the surface charge of permeating species and/or the surface charge of the channel walls by applying electric potentials, by controlling the external pH, or by

controlling the ionic strength of the solution. Physical gating is achieved by physically restricting (blocking) flow through the pores. Molecules have been attached to the channel entrance capable of rotating to block it in response to an external stimulus. The inner channel surfaces have been modified with molecules that change volume according to applied stimuli. Flow through the channel is restricted or blocked by physically impeding it.

Synthetic membranes are advantageous because they are fairly robust when compared to membranes featuring biological components. Synthetic components can typically withstand a broader range of temperatures, pHs, and pressures and are capable of handling larger stress loads. As a result, synthetic membranes more readily integrate within micro- and macro-scale systems and devices. Typically, they can better withstand the harsh environmental conditions imposed during conventional micro- and nano- fabrication techniques. Furthermore, it is possible to fabricate synthetic membranes with a high degree of specificity over their dimensions, design, and material composition. This makes synthetic membranes extremely versatile and amenable to a much broader range of applications than their biological counterparts. The challenge remains to approach the efficiencies, specificity, and multifunctionality that biological components and systems typically exhibit using synthetic components and systems.

1.2 *Membranes Constructed from Vertically Aligned Nanostructures*

To realize the ideal represented by the biological cell membrane with synthetic materials requires the ability to define nanoscale features within a microscale system. Such systems are possible through the epitaxial growth of metal oxide nanowires [99-101], by deep reactive ion etching nanoscale features from a silicon substrate, or through the deterministic growth of vertically aligned carbon nanofibers (VACNFs). The latter two methods of synthesizing vertically aligned structures are discussed in depth below.

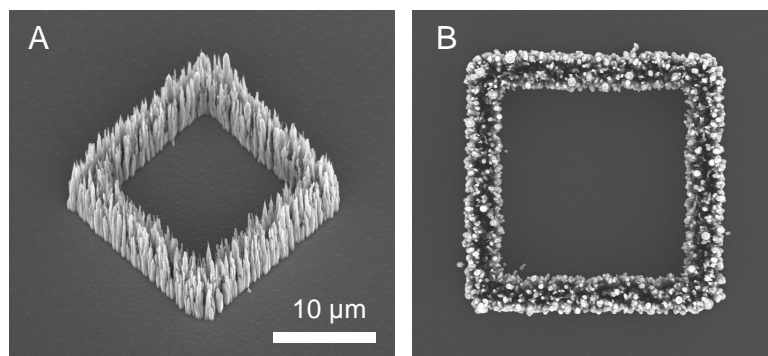


Figure 1-12) Electron micrographs of a VACNF membrane structure **A)** from a 45° angle and **B)** from the top. Prior to growth, the nickel catalyst was patterned using microscale lithography techniques. The membrane structures were then grown as 25 μm cells with walls 2 μm wide. Carbon nanofibers were generally 8.5–9.5 μm tall.

1.2.1 *Vertically Aligned Carbon Nanofibers*

Synthetic membranes, fabricated using VACNFs as the principle membrane component, have been previously described by our group [102-104]. The spatial positioning of VACNFs can be controlled by patterning the nickel metal catalyst using micro- or nano- scale lithography. The sample is then placed on a heated cathode in an evacuated vacuum chamber. Ammonia is introduced into the chamber, causing the catalyst to break up and then coalesce into discrete nanoparticles. Acetylene is added then a DC plasma is struck. VACNF growth begins with the absorption and decomposition of acetylene on the surfaces of the nickel nanoparticles. The carbon diffuses through (or around) the nickel particles and precipitates on the bottom surfaces, eventually lifting the nickel particles off the substrate. As growth proceeds, the VACNFs align along the applied electric field.

VACNFs can be grown with control over individual fiber length, diameter, shape, position, orientation, and chemical composition [1]. Within an ensemble of fibers that make up a microscale membrane structure, such control allows for precise engineering of critical dimensions such as interfiber spacing and membrane thickness, which dictate membrane permeability and size selectivity. Furthermore, the catalytic growth of carbon nanofibers allows for nanoscale functionality to emerge from simple microscale lithography techniques. VACNF growth typically yields individual nanofibers up to several hundred nanometers in diameter, spaced several hundred nanometers apart (see Figure 1-12). As a result, membranes of carbon nanofibers, patterned using

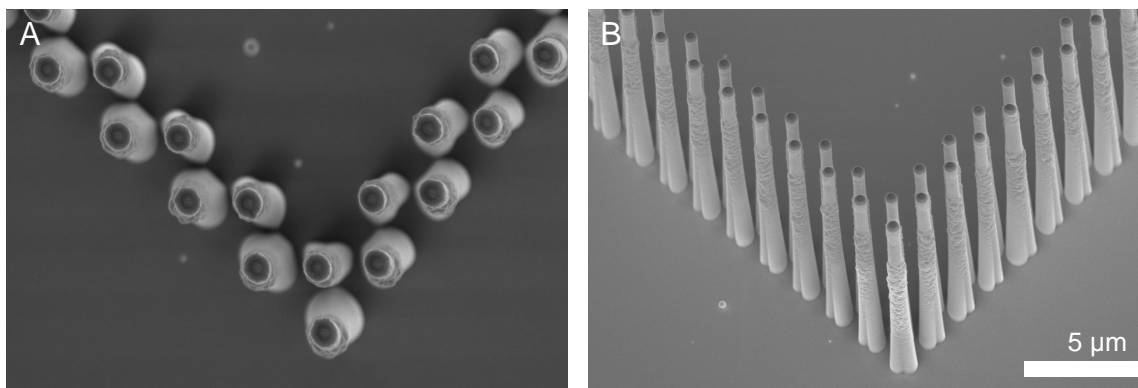


Figure 1-13) SEM images of gold-coated silicon posts **A)** from the top and **B)** at a 45° angle. Silicon posts were etched ~11 μm tall at an interfiber spacing of 1.5 μm.

techniques such as contact photolithography, have nanoscale features that emerge during synthesis.

1.2.2 *Silicon Posts*

Metal-coated silicon posts can function in a similar capacity to VACNFs in synthetic membrane structures. The spatial positioning of etched silicon posts is determined by micro- and nano- scale lithography. Metal is patterned onto a silicon substrate to act as a protective mask during subsequent etch processes. The sample is then loaded onto a cryogenically cooled cathode in an evacuated vacuum chamber. Oxygen and sulfur hexafluoride (SF_6) are introduced to the chamber and a plasma is struck. Silicon is selectively removed from areas of the substrate unprotected by the patterned metal mask. SiO_xF_y functional groups condense on the resulting sidewalls, protecting them from lateral etching. The result is a highly anisotropic etch, with aspect ratios of 30:1 or more and sidewalls virtually perpendicular to the substrate (88°-92° to substrate) [105].

Lithographically defined metal masks, combined with high rate deep reactive ion etching processes, can produce silicon posts of similar dimensions and aspect ratios to VACNFs. Further, these structures can be coated with metals to make them electrically addressable. To do so, silicon substrates with etched silicon posts are first passivated with an oxide. Samples are loaded into a PECVD system and silicon dioxide is deposited onto the substrate. Then, metal is selectively deposited onto the substrate to coat the silicon posts and make them electrically addressable. The silicon posts essentially act as

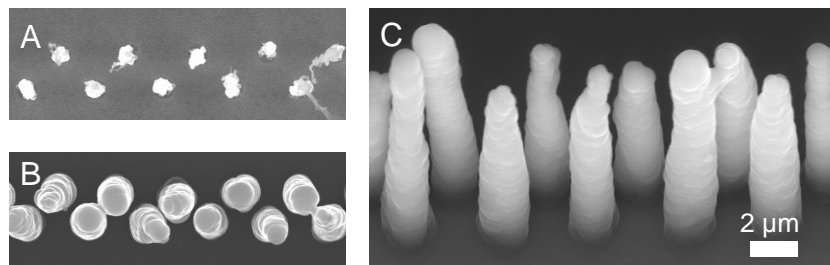


Figure 1-14) E-beam patterned carbon nanofibers, **A)** before PPy polymerization and **B and C)** after. Nanofibers are shown **A and B)** from the top and **C)** from a 45° angle.

a template for the three dimensional patterning of electrodes. Gold-coated silicon posts are shown in Figure 1-13. While silicon posts are more inflexible and, thus, more vulnerable to mechanical shearing than VACNFs, there is less variability in the dimensions of the silicon posts. This allows for more precise definitions of membrane properties which dictate permeability and size selectivity.

1.2.3 Surface Modification by the Electropolymerization of Pyrrole

Interfiber spacing, and resultant membrane pore size, can be further tuned through physical modification or coating. VACNFs possess electrochemical properties typically found in carbon-based electrodes. This allows for physical modification of the surface of the membrane components using electropolymerization techniques. Conductive polymers, such as polypyrrole, have been electrochemically synthesized on the electrically active surface areas of vertically aligned, electrically addressable nanostructures to controllably modify their dimensions and surface energy (see Figure 1-14) [106]. In addition to passive adjustment of pore sizes, the PPy coating can be actuated, providing a means to dynamically modulate membrane permeability and size selectivity.

Polypyrrole is an electrically conductive, biocompatible polymer with well understood physical and chemical properties [107-110]. High quality, stable films are relatively easy to prepare at low temperatures (25°C) and under aqueous conditions. Anodic oxidation of the monomer results in a polymer film forming on the cathodic electrode. Actuation is initiated when the oxidation level of the polymer film is changed in the presence of an electrolyte. The mechanics of this reaction have been extensively

described [111-113]. In experiments described within this dissertation, the large anion dodecylbenzenesulfonate (DBS) is incorporated within the PPy matrix during polymerization to balance the positive charge resulting from protonation of the monomer. The anion is relatively large and becomes trapped within the polymer matrix. When the polymer/anion matrix is reduced, cations from the surrounding electrolyte rush in to balance the charge, resulting in an increase in volume and swelling of the polymer. Coating membrane components with polypyrrole enables modulation of membrane permeability by physically modulating the interfiber spacing and resultant pore sizes, facilitating dynamic switching between “open” and “restricted” flow states. Flow through the membranes is “restricted” when the PPy coating is swollen by applying a negative bias to the film.

1.3 *Scope of Dissertation*

The goal of this dissertation is to describe the synthesis and demonstrate the application of vertically aligned nanostructure-actuable polymer hybrid membranes that represent the first steps towards the creation of a dynamic “cell mimic” structure. Selective transport of species was achieved by depositing the actuable polymer, PPy, onto the vertically aligned nanoscale membrane components. Actuating the polymer enabled dynamic control of membrane permeability and size selectivity.

Chapter 2 provides a description of the techniques used to construct carbon nanofiber membranes. Chapter 3 is about the electropolymerization of polypyrrole to controllably modify the surface properties of carbon nanofibers. In Chapter 4, the methods used to controllably alter membrane permeability are outlined. Chapter 5 discusses the use of polypyrrole-coated nanofiber membranes to selectively capture and release nanoscale species. Finally, concluding remarks are presented in Chapter 6.

Chapter 2

Vertically Aligned Carbon Nanofiber Membranes

The first step to creating vertically aligned nanofiber-actuable polymer hybrid membranes requires the controlled synthesis of nanoscale features within structures that are microns to millimeters in size. To this end, vertically aligned nanoscale post structures were patterned and synthesized within microfluidic channels to create physical obstacles to fluid flow perpendicular to the substrate. The distance between the outer edges of the obstacles defined the “pores” of the membrane. In this chapter, the vertically aligned nanoscale post structures were created through the deterministic growth of carbon nanofibers. The synthesis, testing, and application of coupled arrays of semipermeable membranes constructed from these vertically aligned carbon nanofibers are described.

2.1 *Carbon Nanofibers*

Carbon nanofibers are conical structures with diameters ranging from a few to hundreds of nanometers and lengths from less than a micron to several millimeters [1]. In this dissertation, CNFs are distinguished from other carbon nanostructured materials by their unique internal structure. CNFs are composed of curved graphene sheets, stacked to form quasi-one dimensional filaments [114, 115]. Other carbon nanostructures, referred to as fullerenes or nanotubes, are essentially graphene sheets rolled up into closed cages or hollow cylinders. Structures oriented perpendicular to the substrate on which they are grown are called vertically aligned. In the case of carbon nanofibers, this means the structures are straight and their axes are normal to the substrate.

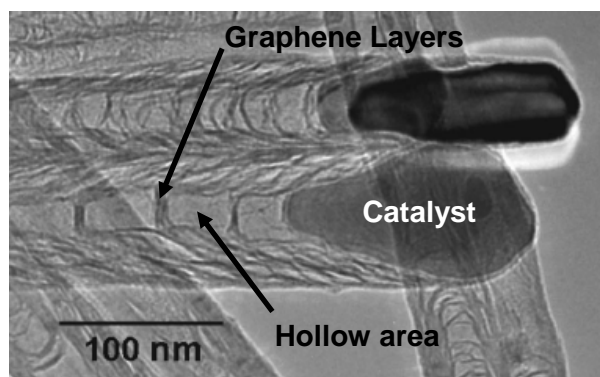


Figure 2-1) High-resolution TEM image of VACNFs grown by PECVD. The VACNFs have a “bamboo” structure. Reproduced from Merkulov *et al.* [5].

2.1.1 Physical Properties

Carbon nanofibers are composed of a catalyst particle, located at the VACNF tip, supported by stacks of graphene layers which are separated by hollow spaces within the nanofiber (see Figure 2-1). The graphene layers form an angle α with the fiber axis [1]. This angle is predominantly determined by the shape of the catalyst nanoparticle during nanofiber synthesis [7]. Two types of nanofibers are defined by α : “herringbone” fibers, with dense conical graphene layers and large α , and “bamboo” fibers, with cylindrical cup-like graphene layers and small α [10]. True carbon nanotubes have an α equal to zero. The names “herringbone” and “bamboo” are derived from structural similarities to the herring fish’s skeleton and the compartmentalized structure of a bamboo stem.

High-resolution transmission electron microscopy (TEM) observations made by Cui *et al.* show that the graphene sheets in carbon nanofibers form an angle with the fiber axis for most of its length [7]. However, this ordered structure disappears at the interface between the nanofiber and the substrate. The base of a carbon nanofiber consists of a thick graphite layer, 1-2 graphene layers thick. The graphitic planes are almost parallel with the substrate (see Figure 2-2). As a result, nanofibers are relatively weak and subject to shearing at their base as compared to the more stable, stacked-cone geometry found through the rest of their length [116].

The small size of carbon nanofibers makes them mechanically stronger than the bulk material [117]. The probability of critical surface flaws decreases as specimen volume decreases. In addition, the vast majority of commercially available carbon has more or less disordered graphitic microstructures. By contrast, the ordered microstructure of carbon nanofibers enhances its strength, stiffness, and toughness



Figure 2-2) Schematic representation of the graphene layers in a VACNF and the catalyst tip. Layers are nearly parallel to the substrate at the base. Reproduced from Cui *et al.* [7].

[118]. The mechanical properties of a single nanofiber were observed in a TEM by Gao *et al.* [119]. An oscillating voltage with a tunable frequency was applied to the nanofiber and resonance was induced by changing the frequency. From the resonance frequency, it was possible to calculate the bending modulus of the nanofiber. The resonance frequency and bending modulus depended on the diameter and length of the nanofiber. Bending moduli from 23 – 32 GPa were measured for nanofibers 33 – 64 nm in diameter and 4.6 – 5.7 μm in length.

In general, carbon nanofibers are robust enough to be chemically and mechanically resistant to many standard microfabrication processes. These include nitric acid and hydrofluoric acid etches, photoresist development, fluorine-based dry etches, and a wide variety of metal, oxide, and nitride depositions. VACNFs can be etched by using oxygen-containing plasmas, electrochemical oxidation, or calcination. By limiting the etch rates and times, these etch processes can also be used to enhance the number of oxygen-rich moieties on the nanofiber surface for surface functionalization strategies [1].

The edges of the graphene layers in carbon nanofibers terminate on the sidewalls. Depending on growth conditions, these edges can be terminated by hydrogen, carboxylic acid, or primary amine groups. Under some growth conditions, the surface of the nanofibers can be modified to include amorphous carbon films and/or materials sputtered from the substrate. The wide variation in surface properties of as-synthesized nanofibers enables a variety of functionalization schemes for immobilizing species. One approach previously described by our group is to adsorb certain heterocyclic aromatic compounds on to the surface of carbon nanofibers [120]. In this strategy, solutions of aromatic compounds are spotted onto the carbon nanofibers and allowed to adsorb for ~10 minutes before unabsorbed species are washed away with distilled water.

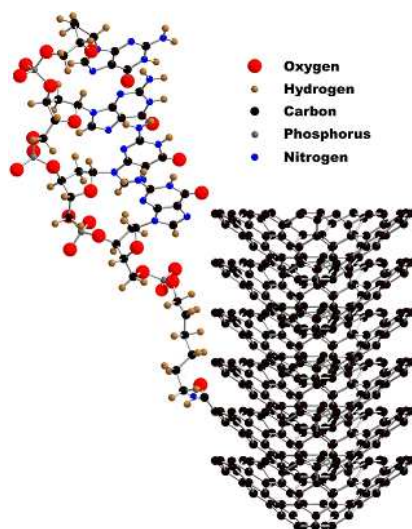


Figure 2-3) A graphical depiction of biomolecular functionalization of a CNF with an amine-terminated oligonucleotide. Reproduced from Klein *et al.* [10].

Rhodamine dyes and conjugated proteins were tethered to the surfaces of VACNFs using this method. Rhodamine is structurally similar to other fluorescent molecules, such as fluorescein. The primary distinction is the replacement of the side-chain hydroxyls in fluorescein with amine functionalities. This difference allows for specific coupling between the amine side-chains present in rhodamine dyes with the carboxylic acid moieties on the VACNFs. Rhodamine dyes were experimentally shown to interact strongly with VACNFs while fluorescein did not. High ionic strength washes or high urea concentrations were needed to displace the rhodamine dyes from the carbon nanofibers while fluorescein was easily removed with distilled water. Tethering molecules using the adsorption technique has the advantage of being a fairly gentle means of immobilizing species.

Our group has also reported a functionalization strategy that involves covalently coupling amine-containing materials, such as DNA and proteins, to carboxylic acid sites on the surfaces of carbon nanofibers (see Figure 2-3) [120]. The number of carboxylic acid sites on the nanofibers' surfaces is usually enhanced prior to functionalization by oxygen plasma treatments. Reactive intermediates, such as 1-ethyl-3-(3-dimethylaminopropyl) carbodiimide (EDC), attach to the carboxylic acid sites and react with available amines to form amides or to hydriyls to form thiol ester linkages. Molecules covalently tethered to carbon nanofibers using this technique remain attached even under stringent washes with high ionic solutions or high urea concentrations. Proteins

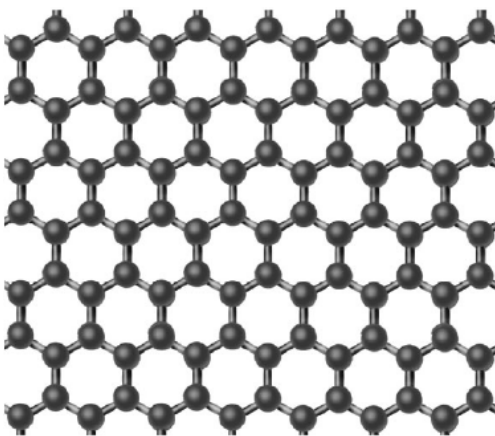


Figure 2-4) Schematic structure of a graphene layer. Atoms are arranged in a hexagonal network. Reproduced from Melechko *et al.* [1].

such as avidin and biotin, functional enzymes such as glucose oxidase [121], single-stranded oligonucleotides [96], and whole plasmids [122] have all been immobilized on the surfaces of carbon nanofibers by covalent coupling.

Carbon-based materials have unique electrical properties due to the various bonding arrangements and electronic configurations that carbon atoms form with their nearest neighbors [123]. In graphite, each carbon atom is sp^2 bonded to three other surrounding carbon atoms to form a hexagonal network of atoms (see Figure 2-4). The electrons located in the pi molecular bonding orbitals are delocalized around the hexagonal rings. Some of these electrons reside in very large molecular orbitals that cover entire graphene sheets and are, thus, free to move and conduct electricity in the sheet plane like a metal. As a result, carbon nanofibers are highly conductive nanoscale materials. They have demonstrated electrical applications as electrochemical probes [16, 122, 124, 125], field effect transmitters [126-128], and ultramicroelectrodes [129].

Lee *et al.* evaluated the electrical characteristics of individual nanofibers by measuring I-V characteristics using a two-point probe technique [130]. Nanofibers were suspended within PMMA, with their ends left exposed. Contact was made to these exposed ends, allowing for I-V characteristics to be measured. The CNFs had diameters of ~95 nm. To test the current carrying capabilities of the nanofibers, a constant bias of 350 mV was applied over 15 days. The current density was found to be relatively stable ($\sim 2 \times 10^6$ A/cm²) over this period of time, demonstrating the reliable current carrying capabilities of the carbon nanofibers. The current density limit of the CNFs was tested by applying a continuously increasing bias. Beyond a critical voltage (~12 V), the current

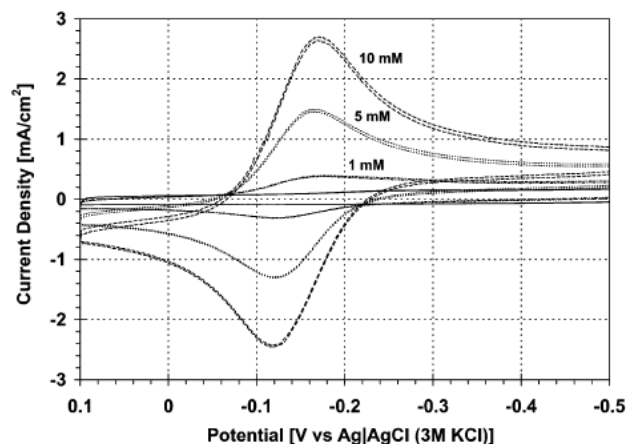


Figure 2-5) Responses of 5 mm diameter nanofiber forest electrodes to varying concentrations of ruthenium hexamine trichloride. Reproduced from McKnight *et al.* [12].

response of the nanofibers became nonlinear. The maximum current density at this voltage was determined to be $\sim 1.8 \times 10^7 \text{ A/cm}^2$. Current-voltage characteristics of the nanofibers indicate that at higher applied biases, the nanofibers change physically. This may be due to electrical breakdown of the outer surfaces of the nanofibers.

The nanofiber resistance measured by Lee *et al.* was 1 k Ω per μm of nanofiber length [130]. Assuming that conduction is through the entire cylindrical cross-section of a nanofiber, the two-probe measurements provide an estimate of the resistivity between 10^{-5} and $10^{-6} \Omega\cdot\text{m}$. A later study made by Zhang *et al.* used a four-point probe technique to exclude contact resistance contributions and to provide better resistivity measurements [131]. The results of this study showed that the resistivity of carbon nanofibers is approximately $4.2 \times 10^{-5} \Omega\cdot\text{m}$. This value is comparable to the value for multiwalled nanotubes, which have calculated resistivities of $9 \times 10^{-6} \Omega\cdot\text{m}$ for 350 nm long sections of 20 nm diameter nanotubes, and to the value of other arc-grown graphite fibers and ropes, whose resistivities are $\sim 10^{-6} \Omega\cdot\text{m}$. Furthermore, the maximum current densities of carbon nanofibers is much higher than that of metal wires ($\sim 10^6 \text{ A/cm}^2$), demonstrating an advantage of covalently bonded organic conductors over metal conductors.

Carbon based electrodes generally feature relatively wide potential windows in aqueous media, are cheap to synthesize, and have low chemical reactivity [1]. Following appropriate surface treatments, carbon electrodes also provide reproducible electrochemical responses. The electrochemical properties of VACNF forest electrodes of different dimensions were characterized by McKnight *et al.* [12]. VACNF forests were

patterned in a variety of sizes, from 250 μm to 5 mm. Several outer sphere, quasi-reversible analytes, including $\text{Fe}(\text{CN})_6^{3-/4-}$ and $\text{Ru}(\text{NH}_3)_6^{2+/3+}$, were used to evaluate the electrodes at 0.5, 1, and 5 mM concentrations in 100 mM KCl. The cyclic voltammograms in Figure 2-5 are representative of the electrochemical responses of a large surface area (5 mm diameter) VACNF forest. The response shows fast electron-transfer kinetics, with cathodic and anodic peak separations very near the ideal 59 mV for a single electron-transfer reaction. The anodic/cathodic peak ratio is also near unity. As expected, the CVs indicate diffusion-limited electrode responses, but with peak currents 10-15% greater than expected from a 5 mm diameter planar electrode [132]. Carbon nanofiber electrodes exhibit a capacitance current of 560 $\mu\text{F}/\text{cm}^2$, dramatically higher than for planar carbon electrodes of the same geometric surface area (20-100 $\mu\text{F}/\text{cm}^2$) [133]. This is due to the large increase in surface area provided by the vertical orientation of the individual nanofiber elements of the forest. The surface area is approximately 10 times greater for forests of nanofibers 5 μm tall than for planar electrodes.

Sparse arrays of carbon nanofibers have been used as ultramicroelectrodes. In one study by Tu *et al.*, low density arrays of VACNFs were grown from randomly electrodeposited Ni on a Cr-coated silicon substrate [134]. SiO_2 , followed by thick layers of epoxy, were deposited to insulate the substrate. The structure was then polished to expose the nanofiber tips. The exposed nanofiber tips responded to the $\text{Fe}(\text{CN})_6^{3-/4-}$ couple as the sum of many ($10^6/\text{cm}^2$) individual ultramicroelectrodes. The response indicated that diffusion to the active nanofiber sites was radial. A second study by Li *et al.* compared the responses of sparse nanofiber arrays to closely packed forests [135]. Nanofibers were grown from Ni and insulated in SiO_2 so that only the tips were exposed. Individually addressed pads of closely packed forests of nanofibers exhibited similar diffusion-limited redox responses to planar electrodes while sparser arrays of nanofibers produced the sigmoidal response of radial diffusion. The sparser arrays provided higher sensitivities of response to surface-immobilized ferrocene compared to the more densely packed nanofiber forests.

McKnight *et al.* demonstrated the ability to individually address carbon nanofibers by using a multistep microfabrication process [124]. Individual nanofibers were electron-beam patterned and grown on tungsten interconnects. Then, the nanofibers were passivated by SiO_2 except at the tips. The redox response of the nanofibers to $\text{Fe}(\text{CN})_6^{3-/4-}$, $\text{Ru}(\text{NH}_3)_6^{2+/3+}$, and $\text{IrCl}_6^{2-/3-}$ was found to be dependent on the amount of exposed

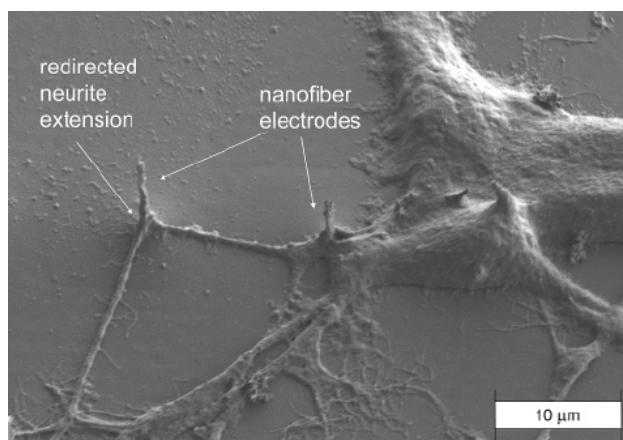


Figure 2-6) Scanning electron micrographs of differentiated PC-12 cells on a nanofiber array. The cells were fixed in 2% glutaraldehyde and dehydrated prior to imaging. The cells are in close proximity to the nanofibers. Reproduced from McKnight *et al.* [16].

nanofiber at the tip, indicating that electron transfer occurs along the entire length of the nanofiber. Longer electrodes ($>10\ \mu\text{m}$ of exposed nanofiber surface area) began to act like cylindrical ultramicroelectrodes, with slight diffusion-limited peaking of the oxidation and reduction curves at scan rates of $200\ \text{mV/s}$ for $\text{Ru}(\text{NH}_3)_6^{2+/3+}$ in $100\ \text{mM KCl}$. Shorter electrodes behaved like point source ultramicroelectrodes. The electrode interfacial capacitance was found by performing voltammetry at multiple scan rates in $100\ \text{mM KCl}$. This capacitance was found to be $\sim 140\ \mu\text{F/cm}^2$ for nanofibers $2 - 12\ \mu\text{m}$ in length.

An important property of carbon nanofibers is their compatibility with biological systems. Correa-Duarte *et al.* showed that the vitality of cells and tissue grown on carbon nanofibers and nanotubes was at least the same as cells grown in a control group [136]. Webster *et al.* described composites made from carbon nanofibers that promoted the growth of neurite extensions (see Figure 2-6) [16, 137]. McKnight *et al.* embedded carbon nanofibers within biological cells to microinject DNA [125]. Arrays of vertically aligned carbon nanofibers were functionalized with DNA and inserted through the cell membrane into the cell nucleus. After a recovery period of about 36 hours, the cells began to reproduce again. Both the impaled cells and their progeny were shown to express the inserted DNA. Cells impaled by nanofibers were observed for up to 7 days and still showed activity at the end of this period.

2.1.2 *Synthesis*

Carbon nanostructured materials have been synthesized by arc discharge [138, 139], laser vaporization [140], catalytic chemical-vapor deposition (C-CVD), and catalytic plasma-enhanced chemical-vapor deposition (C-PECVD) [1, 5, 11, 15, 114, 141-143]. In the arc discharge method, carbon nanotubes are grown on the negative end of a carbon electrode in a dc arc-discharge evaporation of carbon in an argon-filled vessel (100 torr). Buckminsterfullerenes have been synthesized by vaporizing carbon species from a solid disk of graphite using a focused pulsed laser. The carbon species were vaporized into a high-density helium flow, cooled, and carried in the resulting molecular beam to an ionization region. Carbon clusters were then ionized by one-photon excitation with a carefully synchronized excimer laser pulse. Arc discharge and laser vaporization are efficient means of synthesizing large quantities of carbon nanostructured materials. However, these methods do not offer control over the spatial arrangement of the resulting material and complex purification processes must be undertaken to remove amorphous carbon particles and catalyst. The spatial arrangement of carbon nanotubes and nanofibers grown by C-CVD and C-PECVD can be controlled and purification is unnecessary.

During the catalytic growth of carbon nanostructures in a chemical-vapor deposition process, a reactant hydrocarbon molecule first adsorbs then decomposes on the surface of a catalyst. Adsorbed carbon species dissolve and diffuse through the metal nanoparticle and precipitate on the opposite surface [144, 145]. The carbon deposits on one side of the surface of the catalyst particle, limiting the growing carbon film in two dimensions to the size of the nanoparticle. The third dimension is not bound, leading to quasi-one dimensional growth. As the carbon nanostructure grows, the catalyst particle is lifted off the substrate and remains at the tip throughout growth. The nature of the catalyst, the reaction temperature, and the composition of reactant gases dictate the morphology, crystallinity, and growth rate of the resulting nanofiber [1].

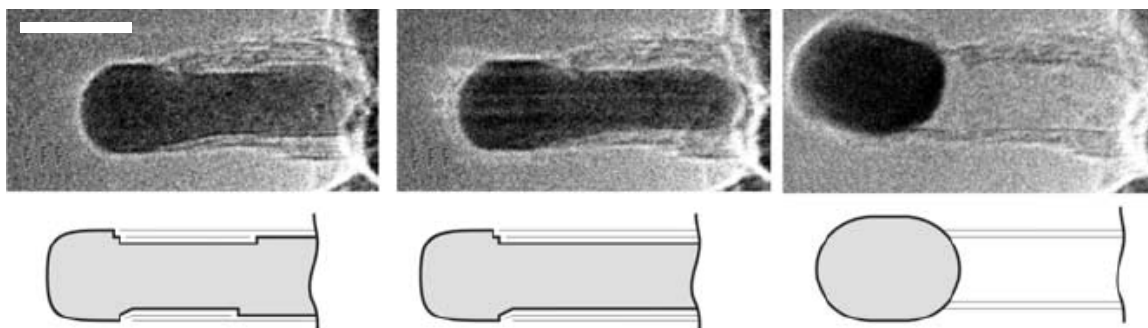


Figure 2-7) Image sequence showing a growing nanofiber. The nickel catalyst is the dark portion of the image and is elongated in the first two images. The catalyst particle snaps back to a more circular shape in the third image, leaving behind a void. Drawings are included to illustrate the C-Ni interface. Scale bar is 5 nm. Reproduced from Helveg *et al.* [14].

Ajayan used atomic resolution *in situ* TEM to show the development of carbon nanofibers during growth [14, 146]. Carbon nanofibers were observed to develop through a reaction-induced reshaping of the catalyst nanoparticle (see Figure 2-7). The initial shape of the catalyst transforms into a highly elongated shape, where graphene sheets form more rapidly parallel to the elongated catalyst surface. At a certain aspect ratio (length/width) of about 4, the catalyst particle abruptly contracts to a spherical shape, leaving behind a void in the interior of the carbon nanofiber (and sometimes residual catalyst material). Elongation/contraction continues until catalytic growth ceases or the catalyst nanoparticle becomes encapsulated in graphene.

The primary distinction between CVD and PECVD is that in CVD processes thermal energy is used to activate gases, whereas in PECVD processes molecules are activated by electron impact. The plasma enhancement effectively reduces the activation energy necessary for deposition. Thus, decomposition of carbonaceous species on the surface of a catalyst benefits from plasma enhancement. One of the most important benefits of PECVD processing is the ability to control the alignment of carbon nanofibers. The carbon nanofibers align to the applied electric field during PECVD growth.

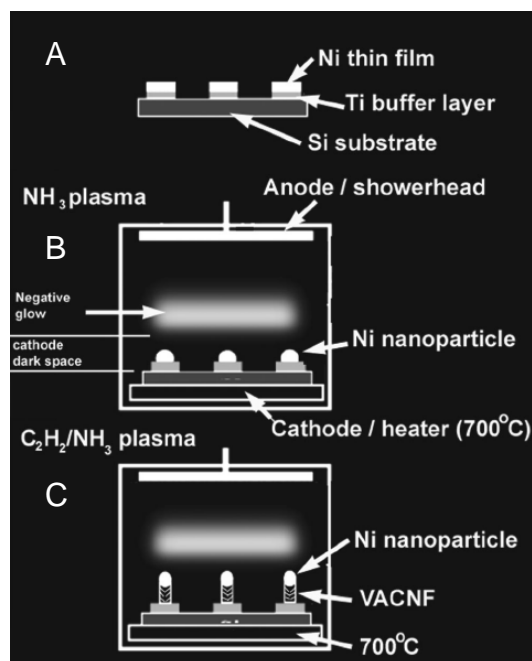


Figure 2-8) Schematic representation of the PECVD process for growing VACNFs. **A)** Catalyst deposition, **B)** catalyst pretreatment in an NH_3 plasma, and **C)** growth of VACNFs. Reproduced from Melechko *et al.* [1].

PECVD synthesis of carbon nanofibers is conducted in a vacuum chamber. Gas flow to and from the chamber is controlled by a pressure control system consisting of gas manifolds and mass flow controllers. Within the chamber is a substrate heater controlled by an external temperature control system and a showerhead for uniform gas mixing and distribution over the substrate. In the case of dc-PECVD, the substrate heater also acts as a cathode and the showerhead as an anode. It is crucial that the substrate be electrically conductive or severe arcing will occur [1]. If growth on an insulating substrate is desired, either a radio frequency (RF) power source must be used, which changes the polarity of the electrodes fast enough to avoid surface charging, or a thin metal must be deposited under the catalyst film to establish contact between the cathode and the metal surface.

Patterning and depositing catalyst material is essential to the synthesis of isolated VACNFs. The most common method of patterning catalyst materials begins by spin coating a substrate with a photosensitive polymer. Catalyst sites are patterned by exposing the polymer to UV light through a photomask or by writing the pattern in the polymer with an electron beam gun. Either way, the solubility of the polymer is changed by exposure to photoexcitations. Then, polymer at the catalyst sites is developed away,

while the rest of the substrate remains masked by the remaining polymer from subsequent processing. Catalyst metals are then deposited on to the substrate by one of a number of different methods including evaporation, sputtering, and electroplating [147]. After metal deposition, the remaining photosensitive polymer is removed. Excess metals are lifted off with the polymer, leaving catalyst metals on the substrate only at the defined catalyst sites (see Figure 2-8A).

The substrate is then placed in the vacuum chamber on the heated cathode and the chamber is pumped down to an acceptable base pressure ($\sim 1 \times 10^{-5}$ Torr). The substrate is heated to the growth temperature (typically between 500 to 700 °C), gases are introduced, and a plasma is struck. As an example, carbon nanofibers have been synthesized in a dc-PECVD from a 40 nm layer of patterned nickel catalyst on a Si substrate. The substrate was heated to 700 °C and then ammonia (NH_3) was introduced to the vacuum chamber (flow rates typically between 50 – 200 sccm). A dc plasma was struck to pretreat the sample with NH_3 plasma, breaking up the catalyst into discrete nanoparticles (see Figure 2-8B). After this pretreatment step, acetylene (C_2H_2) was introduced into the chamber (flow rates typically between 20-150 sccm) while maintaining the NH_3 plasma, immediately initiating the growth of VACNFs (see Figure 2-8C). Gases were maintained at a constant pressure (typically between 2 – 10 Torr) over the entire synthesis process (10 minutes to 10 hours).

In PECVD synthesis of carbon nanofibers, process parameters such as substrate temperature, total gas pressure, total gas flow, the carbon source to etchant gas flow ratio, plasma power (current and voltage), and electrical field distribution all play a role in shaping the outcome of the growth process. PECVD processes are typically used for both the deposition of thin films and for etching, depending on process conditions. It should be noted that carbon nanofiber synthesis is conducted in the etching regime, to avoid thin carbon film formation. As a result, special consideration is always given to find the balance between etching and deposition to avoid the detrimental formation of carbon while enabling the synthesis of carbon nanofibers [1].

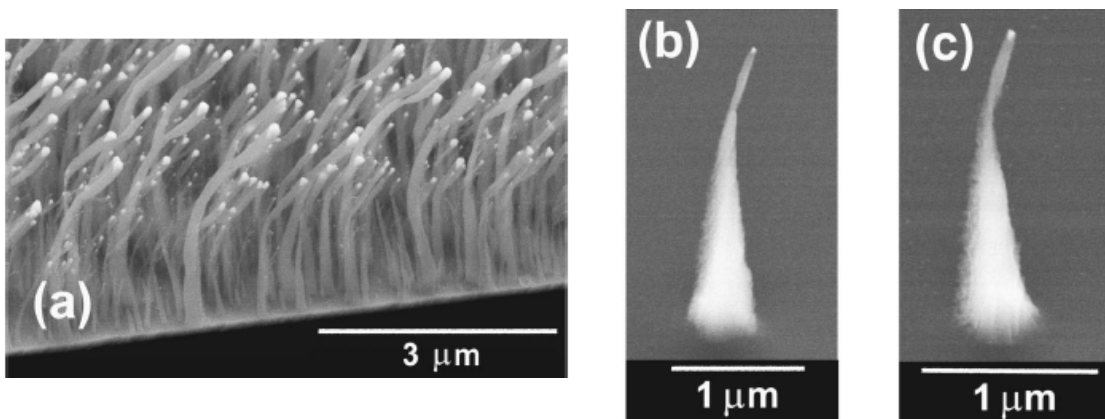


Figure 2-9) SEM images of **A)** a forest and **B,C)** individual kinked nanofibers. The kink was the result of changing the direction of the applied electric field mid-growth. Reproduced from Merkulov *et al.* [11].

A significant electrostatic force is exerted on the fibers by the electric field during growth [148]. The field is enhanced at the tip of the growing nanofibers, with the enhancement factor roughly equal to the ratio of the fiber length to the tip radius of curvature [141]. Because of this enhancement, the vast majority of the electrostatic force experienced by the nanofiber is at the tip, essentially directed perpendicular to the substrate. A uniform tensile stress is applied across the entire nanofiber/catalyst particle interface [11]. As a result, carbon precipitates uniformly across the bottom of the catalyst nanoparticle and the fiber grows vertically. If there were a fluctuation in the carbon adsorption on the surface of the nanoparticle (by changing the alignment of the electric field or the alignment of the substrate), CNF growth would deviate from vertical alignment. In fact, the alignment of CNFs was changed by Merkulov *et al.* mid-growth by changing the direction of the applied electric field. Carbon nanofibers were grown in an electric field perpendicular to the substrate (see Figure 2-9). Midway through the growth process, the substrate was shifted on the holder so that the electric field was at an angle to the substrate. The result was ‘kinked’ nanofibers, with the base vertically aligned and the tip at an angle (see Figures 2-9B and 2-9C).

VACNF growth rate is proportional to the number of radicals impinging on the catalyst surface and on the decomposition rate of these radicals. One way to increase growth rate is to change the gas mixture or plasma power to create more radicals. Plasma power is affected by process parameters such as applied bias, current, temperature, and pressure. Another way to affect the growth rate is to increase the number of molecules with higher decomposition rates. This is accomplished by adjusting the gas flow rates and/or the ratio of carbon source to etchant gas. However, increasing

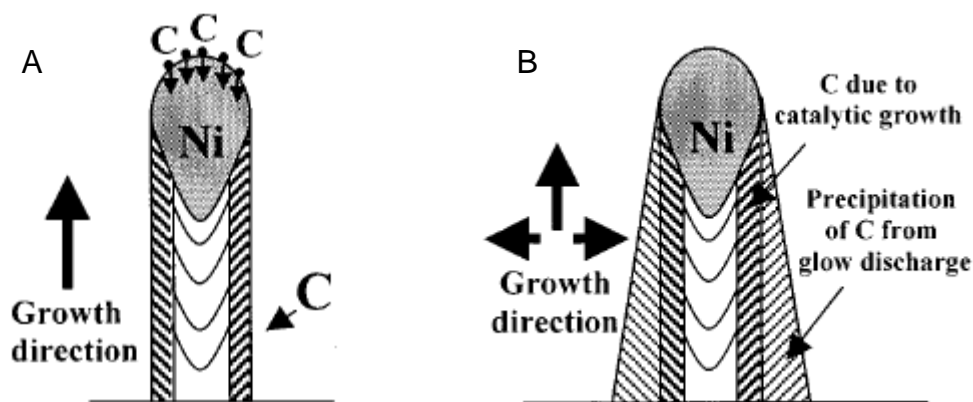


Figure 2-10) Schematic representation of the growth of **A)** a conventional vertically aligned carbon nanofiber and **B)** a carbon nanocone formed from additional precipitation of C on the outer walls during growth. Reproduced from Merkulov *et al.* [15].

the number of molecules with higher decomposition rates may lead to a shell forming around the catalyst particle, limiting access to it and halting growth. Further increases may result in the formation of a film covering the entire substrate [142, 149]. If too many of the molecules in the gas mixture have low decomposition rates, growth of carbon nanofibers may be extremely slow or totally inhibited.

The aspect ratio of carbon nanofibers is dependent on the ratio of carbon source to etchant gas molecules [15]. While the tip diameter of a CNF is limited by the diameter of the catalyst nanoparticle, the base of the nanofiber is not. As growth proceeds, the base diameter of a carbon nanofiber increases at a rate dependent on the carbon to etchant gas ratio. In carbon-rich gas mixtures, precipitation occurs on the side walls of the growing carbon nanofibers in addition to precipitation on the bottom of the catalyst nanoparticle. The net result is growth in two directions: vertically and laterally (see Figure 2-10B). Thus, nanofibers with a wide variety of heights and aspect ratios can be synthesized.

2.1.3 Summary

A remarkable degree of control over the shape, location, and chemical composition of carbon nanofibers can be exerted by adjusting the plasma growth parameters during synthesis. Within an ensemble of nanofibers that make up a microscale membrane structure, such control allows for precise engineering of critical

dimensions such as interfiber spacing and membrane thickness. VACNF growth typically yields individual nanofibers up to several hundred nanometers in diameter, spaced several hundred nanometers apart. As a result, the catalytic growth of carbon nanofibers allows for nanoscale functionality to emerge from simple microscale lithography techniques. Furthermore, carbon nanofibers are chemically and mechanically robust enough to survive the rigors of microfabrication processing. Thus, carbon nanofibers can act as modifiable three-dimensional surfaces in combination with microfluidic, electronic, and biological structures. The unique physical properties of carbon nanofibers allow for the design of robust membrane structures that enable rapid, diffusion-based transport and integration within other synthetic devices.

2.2 *Membranes Constructed from Stochastic Forests of VACNFs*

Nanoporous membranes were constructed from stochastic forests of vertically aligned carbon nanofibers [102]. First, microfluidic channels were patterned and etched from a silicon wafer. Photoresist was spun and baked on a 100 mm silicon wafer. Then, channels were patterned by exposing the photoresist to UV light through a contact mask. After development, residual photoresist was removed in an oxygen plasma. This left the underlying silicon wafer exposed where the microfluidic channels were patterned while the rest of the wafer remained coated by photoresist (Figure 2-11A). Inductively coupled (ICP) SF₆-based plasma reactive ion etching (RIE) was used to etch the channels out of the silicon. Channels were typically etched to depths of 8 – 15 μm (Figure 2-11B).

Catalyst was then patterned and deposited on the bottom of the microfluidic channels. Without removing the photoresist from the previous etch, a second layer of photoresist was spun on the wafer and baked. It was necessary to preserve the photoresist from the previous etch in order to protect the wafer's non-planar features. A grid was patterned in the bottom of the channel by exposing the photoresist to UV light through a contact mask. An image reversal was then performed by baking the wafer in NH₃ at 90 °C. After flood exposure, the pattern on the wafer was developed and cleaned of residual resist in an oxygen plasma (Figure 2-11C). Ti (100 Å) wetting layers and a Ni (400 Å) catalyst layers were then deposited by electron beam evaporation. The sacrificial photoresist was lifted off in acetone, leaving only the patterned catalyst behind

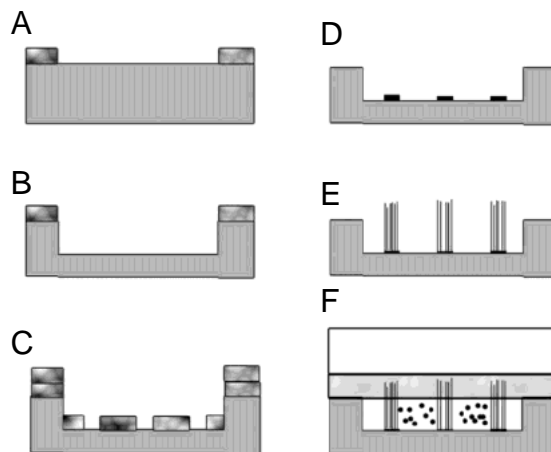


Figure 2-11) Diagram of the microfabrication process.

A) The channel is patterned in photoresist. **B)** Microfluidic channels are etched into the Si substrate. **C)** The catalyst pattern is defined in a second layer of photoresist. **D)** Ni catalyst is deposited. **E)** VACNFs are grown in a PECVD. **F)** The structure is sealed with a PDMS-glass slide lid.

(Figure 2-11D). The catalyst was patterned as an array of cells 250 μm by 250 μm , with grid lines 2 μm wide.

Vertically aligned carbon nanofibers were grown from the patterned nickel catalyst using a dc-PECVD process (Figure 2-11E). The nickel catalyst lines were broken up into nanoparticles in an NH_3 plasma prior to growth. The spacing and size of the resulting Ni nanoparticles defined the pore sizes of the membrane. Individual nanofibers grew from each Ni nanoparticle by the catalytic decomposition of C_2H_2 . The growth conditions produced nanofiber forests with densities of 1 to 4 nanofibers/ μm^2 and interfiber spacings of 250 – 500 nm. The nanofibers were slightly conical in shape and were $\sim 8 \mu\text{m}$ taller than the etched channel depth (Figure 2-11F). Electron micrographs of the resulting structures are shown in Figure 2-12.

Fluorescent species were dispensed within each 250 μm by 250 μm carbon nanofiber cell using a piezo-based reagent jetting system. The dispensed volumes were on the order of 15 pL. Aqueous solutions of this volume would evaporate within minutes, complicating experimentation. Drying also harmed biological reagents and would cause species to become fixed to the silicon surface. Reagents were diluted in 25% aqueous glycerol to reduce the evaporation rate of the dispensed solutions. Solutions including dimethyl sulfoxide (DMSO) were also found to reduce the evaporation rate, but DMSO would cause the droplet to spread after dispensing. The glycerol also kept particles from falling out of suspension. Latex beads as large as 750 nm remained suspended, even

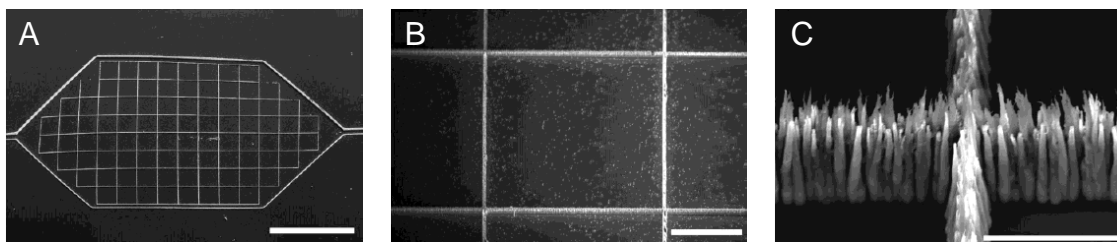


Figure 2-12) SEM images of the VACNF cell structures. A) The entire structure in a microfluidic channel. The inlet and outlet channels are 50 μm wide. The channels are 10 μm deep. B,C) The VACNF structures viewed at a 45° angle, showing close-ups of a single cell and the component nanofibers. Scale bars are 1 mm, 100 μm , and 10 μm on A, B, and C respectively.

after centrifugation of 1% bead solutions in 25% glycerol for five minutes at 9300 x g. Although the addition of glycerol helped to keep the beads suspended, they would still adhere strongly to the silicon substrate because of an electrostatic attraction. Adding phosphate buffered saline to the dispensing solution would partially alleviate this problem. Blocking the silicon surface with bovine serum albumin (1%) further reduced the adhesion to acceptable levels.

Several approaches to sealing the membrane structures were considered. The choices were limited by the need to protect the integrity of the dispensed reagents. As a result, adhesives, high temperature sealing techniques, and solvents had to be avoided. A further challenge was created by the minor variations in nanofiber height, making it difficult to create an effective seal with hard, planar materials acting as the lid. Sealing with a soft polymer, such as poly-(dimethylsiloxane) (PDMS) was advantageous because the nanofibers could be grown to extend above the channel walls and could pierce into the PDMS to create a sealed structure. PDMS alone had a tendency to sag into the channels and adhere to the silicon substrate, effectively pinching off fluid flow. To remedy this problem, a glass slide was coated with PDMS and placed on edge to allow gravity to thin the coating as it dried. This created a thin PDMS layer of about 40 μm , with the slide providing a rigid backing. After curing, the PDMS-coated glass slide was clamped onto the carbon nanofiber structures using paper binder clips (9.5 mm capacity). The enclosed fluidic structures formed an array of cells with individual volumes on the order of 250 pL.

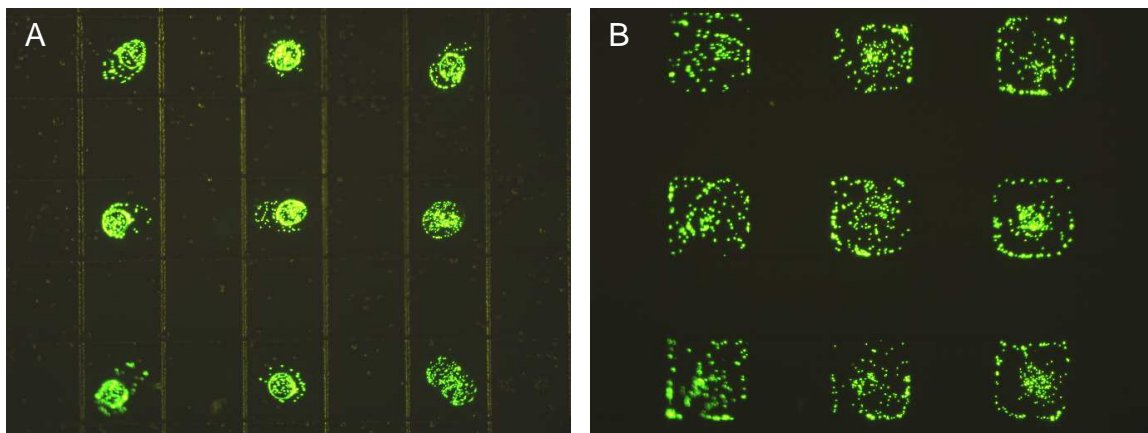


Figure 2-13) Fluorescence micrographs of the VACNF cell structures. **A)** Individual cells were filled with 0.02% solutions of 750 nm fluorescein-labeled latex beads. **B)** The same cell structures after sealing and wetting.

Devices were tested by dispensing 750 nm fluorescently labeled latex beads into selected cells. Figure 2-13 shows fluorescent micrographs of the structures before and after wetting of the device. Before sealing, the fluorescent spots show the locations where beads were dispensed (Figure 2-13A). After sealing, the structures were wetted with buffer solution (100 mM Tris, pH 8.0) by capillary action. As shown in Figure 2-13B, the beads were dispersed but remained contained within their individual cells even after fluidic exchange. Individual beads were observed to move freely within their cells and only occasionally would aggregate or adhere to the cell walls. Wetted structures were observed to effectively contain fluorescent species even after several weeks of storage and multiple fluid exchanges. A PDMS glass slide lid was removed after experimentation and imaged in an electron microscope. Electron micrographs showed that the nanofibers pierced the PDMS lid and that some of them even remained in the PDMS after removal.

Fluorescent species of a range of sizes were dispensed within the structures to test their size dependent containment limits. Shown in Figure 2-14 are a series of images of the structures filled with latex beads 500 (Figure 2-14A), 400 (Figure 2-14B), and 300 nm (Figure 2-14C) in diameter. Beads with diameters greater than 500 nm were completely contained within their cells, consistent with measurements of the nanofiber density and pore sizes. Partial containment was observed for beads as small as 100 nm (smallest size tested). However, for the experiments involving beads smaller than 500 nm, there was leaking at discrete locations within the membrane walls. The stochastic placement of the nanofibers prevented precise definition of the membrane elements and led to leaking at the less dense areas of the membrane.

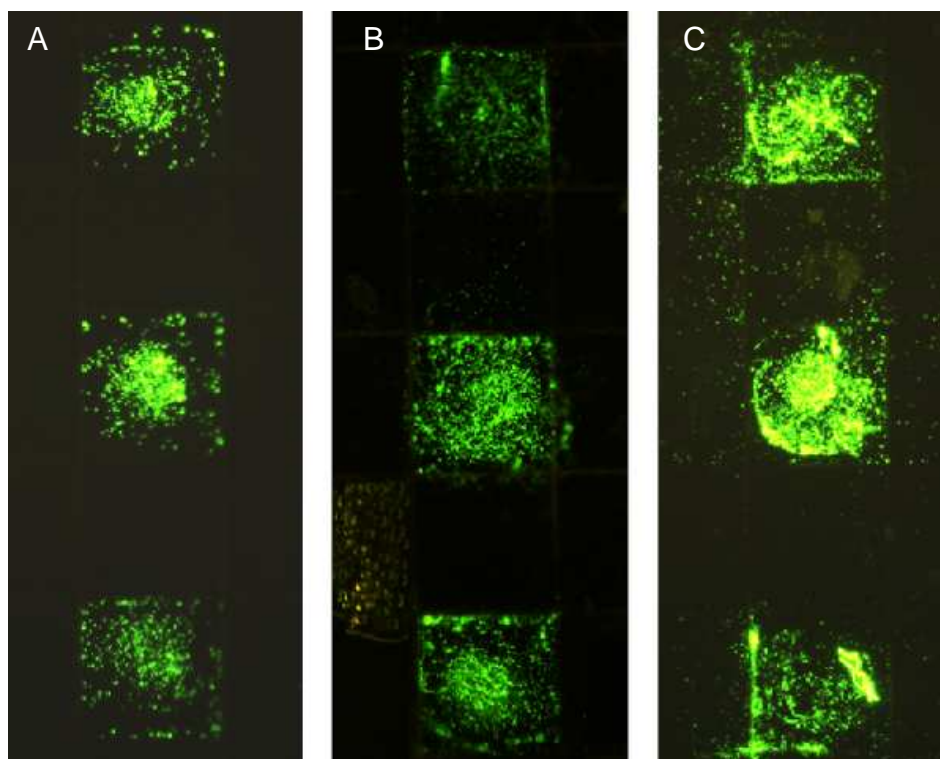


Figure 2-14) Fluorescent micrographs demonstrating the VACNF membrane containment limits. Structures were filled with **A)** 500 nm, **B)** 400 nm, and **C)** 300 nm fluorescein-labeled latex beads. Complete containment was observed for 500 nm beads, but some leaking was observed for the smaller beads.

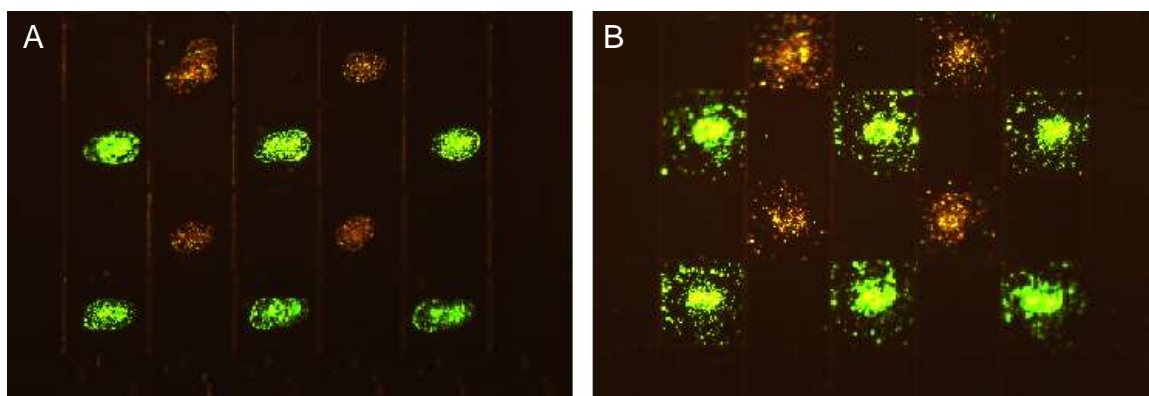


Figure 2-15) A section of the VACNF cell structure selectively filled with either 500 nm fluorescein-labeled or 500 nm tetramethylrhodamine-labeled latex beads. The structures are shown **A)** before sealing and wetting and **B)** after.

Dispensing reagents by ink jet allowed for specific addressing of individual cells within the array. In turn, this enabled patterning of multiple types of reagents within a single structure. To demonstrate this ability, latex beads with either red or green fluorescent labels were dispensed in specific cells of the structure. As seen in Figure 2-15, different reagents can be contained within individual cells with little inter-exchange, while fluid diffuses freely throughout the entire structure. This arrangement allowed for

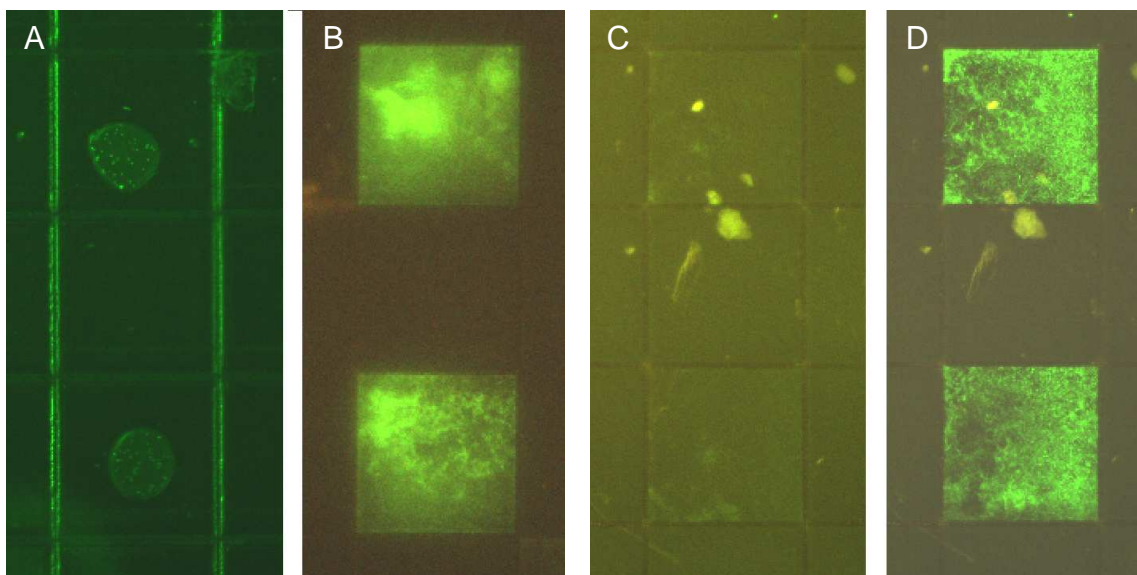


Figure 2-16) *E. coli* were **A)** deposited into individual cells of the VACNF structures **B)** and were grown in the presence of growth media. In **A)** and **B)**, the *E. coli* strain BL21(DE3) expressed GFP from a plasmid. In **C)** and **D)**, *E. coli* strain BL21(DE3) expressed GFP under control of the pBAD promoter. The *E. coli* in **C)** are shown prior to induction and **D)** after arabinose induction.

transport of solutions through the device while larger species remain contained, analogous to cellular structures where chemicals are transmitted in cell-to-cell communication.

To demonstrate the ability to contain species within the cells while still retaining the ability to communicate with the interiors of the cells, *Escherichia coli* were dispensed in individual cells of the array (Figure 2-16A). The *E. coli* were diluted in a solution of 25% glycerol and Luria broth to prevent dehydration and promote growth. The bacterial cells in Figures 2-16A and 2-16B were modified with a plasmid that encodes for a green fluorescent protein (GFP). After dispensing the bacterial cells, the structures were sealed and wetted with growth media and the bacteria were incubated overnight. The *E. coli* divided to fill their nanofiber cages, yet stayed contained within them (Figure 2-16B). Observation through a fluorescence microscope showed that the majority of bacteria were still mobile within their carbon nanofiber containers, while a small number appeared to settle on the silicon substrate. *E. coli* cells are generally rod shaped and 1 – 3 μm in length. These dimensions are significantly larger than the pore sizes of the carbon nanofiber membranes and, thus, the bacterial cells would remain caged within their containers.

Possible applications of these structures include for studies of chemical signaling between biological cells and for live cell based sensing systems. To illustrate, *E. coli*

cells modified with a plasmid expressing a GFP fusion protein under the control of an inducible promoter were dispensed within individual cells of the structure. The promoter controlled GFP production and was sensitive to the presence of arabinose. After dispensing the bacteria, the structures were sealed and wetted with growth media. The bacterial cells were allowed to incubate overnight before observation under a fluorescence microscope. As shown in Figure 2-16C, fluorescence was not detected due to the lack of gene expression. Media containing arabinose was then flowed through the microfluidic channels, inducing the expression of the GFP fusion promoter. The fluorescence micrograph in Figure 2-16D shows *E. coli* cells expressing the GFP fusion promoter.

2.3 Conclusions

Nanoporous membranes were constructed from patterned stochastic forests of vertically aligned carbon nanofibers. Experiments were then conducted to demonstrate the ability of the nanofiber membranes to act as size selective barriers. Carbon nanofiber membranes were patterned and grown as four-walled cells, 250 μm by 250 μm . The membranes were synthesized in microfluidic channels 8 – 15 μm deep and the nanofibers were grown to be ~ 4 μm taller than the channel depth, with densities of 1 – 4 nanofibers/ μm^2 and interfiber spacings on the order of 250 – 500 nm. Size selective containment was demonstrated by containing 750 nm beads within individual cells, while smaller species were allowed to freely flow through. The containment limits of the nanofiber membranes were then tested. Total containment for species as small as 500 nm was demonstrated, with the nanofiber barriers at least restricting flow for species as small as 100 nm. Bacterial cells were caged within individual containers. The ability to chemically communicate through the nanofiber membranes was demonstrated by inducing the expression of GFP in the caged bacterial cells with the introduction of arabinose. Arabinose freely flowed throughout the membrane structure, while the *E. coli* cells remained caged.

Constructing membranes from stochastic forests of carbon nanofibers allows for the synthesis of nanoscale features using microscale fabrication techniques. However, the stochastic placement of the nanofibers within the membrane prevents precise definition of the membrane pore sizes and can lead to leaking at specific sites. The

membrane pores are also too large to contain molecules such as proteins. Several approaches can be considered to reduce the pore size of the membrane. Electron beam lithography can be used to precisely define the catalyst sites. Membranes of predefined thickness and porosity could then be constructed. It may be possible to reduce interfiber spacings down to 10 – 20 nm and to produce membranes from a single row of nanofibers using this technique. An alternative approach would be to reduce the free space between nanofibers in the stochastic forest by coating them with oxides, metals, or polymers. The ability to specifically address nanofibers through chemical, electrochemical, or lithographic means can allow for modification of specific nanofibers or regions of nanofibers within the membrane.

Chapter 3

Modification of VACNFs by the Electropolymerization of Pyrrole

One approach to controllably modify the pore size of membranes composed of vertically aligned carbon nanofibers is through physical modification or coating of the nanofibers. In this chapter, the conductive polymer, polypyrrole (PPy), was electropolymerized on the surfaces of carbon nanofibers. Mechanisms for controlling the formation of PPy films were evaluated under a variety of growth conditions. Then, tunable PPy coatings were deposited on the sidewalls of individual, electrically addressable carbon nanofibers. Polypyrrole was chosen for its biocompatibility, commercial availability, and ability to effect volume change in response to electrical stimuli. The combination of PPy with VACNF membranes can enable advanced functionality, such as nanoscale valving of materials and morphological control at the nanoscale.

3.1 *Polypyrrole*

Since Shirakawa *et al.* first reported that doping with iodine could convert the non-conductive polymer, polyacetylene, into a highly conductive material with conductivity $> 10^4$ S/cm [150], conjugated polymers have garnered a significant amount of interest. In most cases, conductive polymers can transfer electrical charges as efficiently as metal conductors and semiconductors [4]. The metal-like conductivity properties of conductive polymers, combined with their polymeric characteristics, specifically flexibility, low density, and ease of modification, have driven the intensity of interest in them. In spite of their short history, conductive polymers already find applications as the electrically active components in organic electronics [151-158], the electrodes in rechargeable batteries [4], and solid electrolytes in capacitors [159, 160]. Of particular interest is the use of conjugated polymers as microactuators. Some conductive polymers can affect controllable volume changes in response to externally

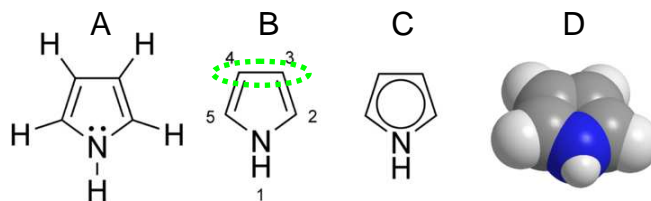


Figure 3-1) Schematic representations of the pyrrole monomer. Pyrrole is a heterocyclic aromatic compound. Reproduced from Wikipedia.com.

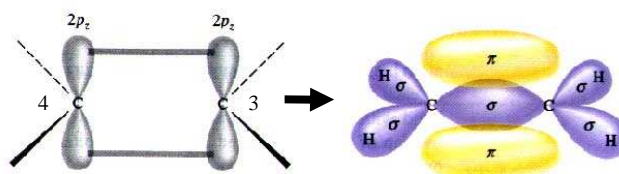


Figure 3-2) A graphical depiction of the formation of a π orbital (RIGHT, yellow) by the overlap of the p orbitals of the two carbon atoms at positions 3' and 4' (LEFT). Reproduced from Wikipedia.com.

applied electrical stimuli [112, 161, 162]. One of the better studied of these polymers is polypyrrole. Polypyrrole is particularly popular because of its chemical stability, high electrical conductivity, ready availability, and ease of synthesis.

3.1.1 Physical Properties

The monomer, pyrrole (C_4H_5N), is a heteroaromatic organic compound, featuring a central ring structure composed of four carbon atoms and one nitrogen atom (see Figure 3-1). Upon oxidation, the pyrrole monomer undergoes a series of polymerization reactions to form polypyrrole. The resulting polymer chain consists of linked pyrrole monomer units, coupled primarily between the carbon atoms at the 2' and 5' positions of the central ring (see Figure 3-1B). The carbon atoms at the 3' and 4' positions are held together by a π bond, created by sideways overlap of the p atomic orbitals of each carbon atom (see Figure 3-2 and the green circled bond in Figure 3-1B) [163]. It is this particular bond that gives conductive polymers, such as polypyrrole, their special properties.

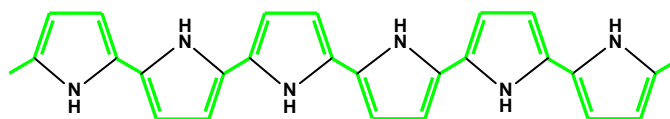


Figure 3-3) Schematic representation of a section of the polypyrrole chain. The green bonds represent the π -conjugated backbone of the polymer.

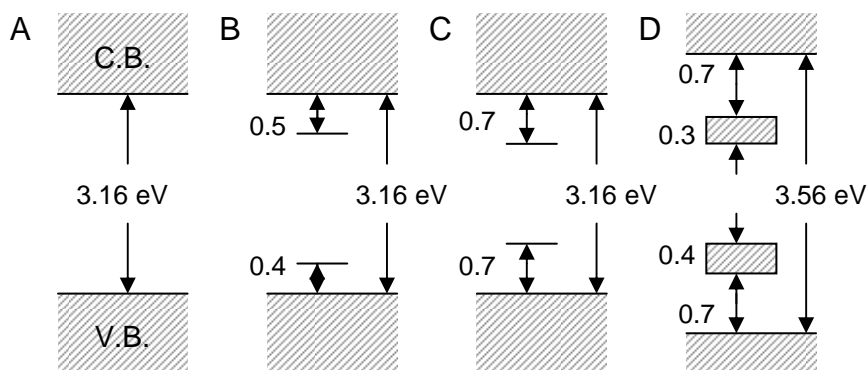


Figure 3-4) Electron energy diagrams for **A)** neutral PPy, **B)** polaron, **C)** bipolaron, and **D)** fully doped polypyrrole. Adapted from Cho *et al.* [4].

Conjugated polymers are distinguished by the system of alternating single and double covalent bonds that form the backbone of the polymer. For polypyrrole, the backbone is formed by the double bonded carbon atoms at positions $5' = 4'$ and $3' = 2'$, by the π bonded carbon atoms at position $4' - 3'$, and by the single bonded atoms at position $2' - 5'$ (see Figure 3-3). This system of bonded atoms is referred to as the π -conjugated backbone structure. It provides polypyrrole with chemical stability and enables its ability to conduct electricity. However, the π -conjugated backbone alone is not sufficient to produce conductivity. As Shirakawa *et al.* discovered, the PPy chain must be doped with ions to change the polymer from an insulating to conducting form.

The electronic and band structures of PPy are changed by the doping levels of the polymer chain [164, 165]. Neutral PPy is an insulator and has the band structure shown in Figure 3-4A. The reported band gap of 3.16 eV is too wide for electrons to cross from the valence to conduction bands. During polymerization, anions in the monomer solution are incorporated into the growing PPy chain to maintain electrical neutrality within the polymer. This doping leads to the extraction of a negative charge from surrounding sections of neutral PPy and local deformations to quinoid structures. A single quinoid structure and the net positive charge (along with the unpaired spin) are referred to as a polaron. The creation of the polaron induces the creation of intermediate bonding and anti-bonding states within the band gap (see Figure 3-4B). The unpaired

electron resides in the bonding state and gives the polaron a spin of $\frac{1}{2}$. As the polymer is further oxidized during the polymerization process, a second electron is eventually removed from the portion of the polymer chain containing the polaron. Rather than forming a second polaron, a bipolaron is created that extends over about four pyrrole monomer units. The bipolaron state lies further from the bandgap edges and has zero spin (see Figure 3-4C). As the polymer eventually becomes fully doped, the bipolaron energy states overlap, creating narrow intermediate band structures (see Figure 3-4D). The intermediate band structures enable electrons to cross from the valence band to the conduction band when an electric field is applied to the polymer.

The electrical conductivity of a material is dependent on its concentration of charge carriers and carrier mobility. The concentration of carriers in a fully doped conducting polymer, such as PPy, is in the range of 10^{21} to 10^{23} cm^{-3} (4-5 times higher than for inorganic semiconductors) [4]. However, the mobility of these carriers is merely comparable to the mobility of carriers in an inorganic semiconductor. The mobility is relatively low in comparison to metal conductors because of the disordered crystal structure and high numbers of defects characteristic of polymers. The overall mobility of carriers in conducting polymers is dependent on intrachain and interchain mobilities. Intrachain mobility is a measure of the charge transfer rate along the polymer chain. Interchain mobility is a measure of the rate at which electrons hop or tunnel from one chain to another. When an electric field is applied to PPy, carriers (polaron and bipolaron) move along the polymer chain by the rearrangement of the double and single bonds on the backbone. When the carriers reach a defect or the end of the polymer chain, the carriers have to hop or tunnel to the next chain. Thus, the net mobility of charge carriers is dominated by intrachain and interchange mobilities.

3.1.2 *Synthesis*

The most widely accepted description of the polypyrrole polymerization process depends on the coupling of radical cations [166]. The polymerization reactions are shown in Figure 3-5. Polymerization is initiated by oxidation of the monomer, using chemical or electrochemical techniques, to yield a radical cation (see Figure 3-5A) [8, 161]. Two radical cations then combine to form a dimer [167] (see Figure 3-5B). This dimer is then, in turn, oxidized and couples with other oxidized oligomers (see Figure 3-

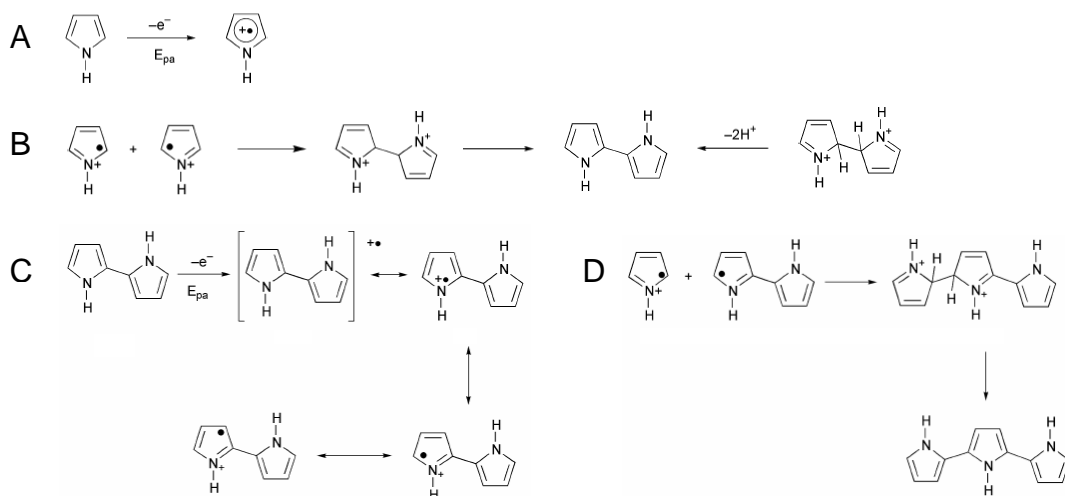


Figure 3-5) Polymerization reactions for the synthesis of polypyrrole. **A)** Oxidation of the monomer. **B)** Coupling of radical cations to form a dimer. **C)** Oxidation of the dimer. **D)** Coupling of the dimer to form an oligomer. Adapted from Sadki *et al.* [8].

5C). The polymer chain continues to propagate by reoxidation and coupling to form oligomers (see Figure 3-5D). During polymerization, anions from the electrolyte are incorporated within the polymer matrix. The anions are held in place by forming a hydrogen bond with the NH moiety of the pyrrole ring [163]. The final polymer chain possesses a positive charge every 3-4 monomer units, balanced by the incorporated anions. Once the chain length exceeds the solubility limit, polypyrrole precipitates out of solution.

Polypyrrole has been prepared in both solution and vapor phases using chemical techniques [168]. In general, an oxidizing agent is added to an ionic solution containing diluted pyrrole monomer. As polymerization proceeds, doped PPy powder precipitates out of solution. Perhaps the most popular oxidizing agents for pyrrole polymerization are oxidative transition metal ions, such as $FeCl_3$, $Fe(NO_3)_3$, $Fe(ClO_4)_3$, $Fe_2(SO_4)_3$, $K_3Fe(CN)_6$, $FeBr_3$, etc [169]. These ferric salts are typically preferred because they result in polymers with higher conductivities. The polymerization process, using $FeCl_3$ as the initiator, can be seen in Figure 3-6.

In general, the resulting polymer's conductivity is dependent on the solution temperature, solvent, reaction time, and concentration of monomer to oxidant. The optimum ratio of $FeCl_3$ to pyrrole monomer has been reported by Armes to be ~ 2.4 [170]. Conductivities as high as 190 S/cm were reported for PPy synthesized at these ratios. Increases in the amount of ferric salt resulted in decreases in conductivity. A similar relationship exists between reaction time and conductivity. Bocchi *et al.*

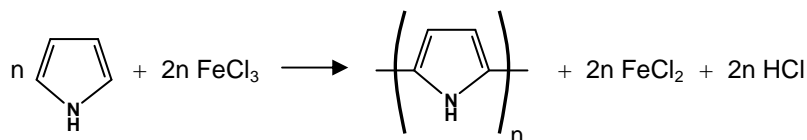


Figure 3-6) Summary of the chemical polymerization of polypyrrole using FeCl₃ as an initiator.

suggested that these relationships are due to copolymerization reactions of secondary products with the same oxidation potential as pyrrole. For solutions containing ferric salts, low temperature synthesis resulted in PPy with the highest conductivities [171]. The reaction rate was lower at lower temperatures, suggesting that the increased conductivity was due to the slower reaction rates.

Surfactants are sometimes also added to solution to improve the conductivity and stability of the resulting PPy or to improve the solubility of monomer in organic solvents. Surfactants such as sodium dodecylbenzenesulfone, sodium alkyl naphthalenesulfonate, and sodium alkylsulfonate have all been used to enhance conductivity, increase yield, and accelerate polymerization reaction rates [172]. Polypyrrole synthesized in a solution containing p-nitrophenol as an additive showed increased doping with a more regular polymer backbone [173, 174]. The electron-withdrawing nitro group in p-nitrophenol strongly interacts with the pyrrole monomer, reducing the number of defects in the resulting polymer chain. Omastova *et al.* believe the increased doping level is due to the large size of the anions that participate in the polymerization reaction.

Polypyrrole can be synthesized using chemical techniques in large quantities, with a great deal of control over the molecular weight and structural features of resulting polymers. Though chemical techniques typically produce polymer in the form of powders, films can also be produced by allowing oxidation to take place at the surface of a solid [168, 175]. However, these films are typically of poor quality and, in some cases, hardly resemble what is commonly referred to as polypyrrole. An alternative method of producing PPy films is by electrochemical oxidation of the pyrrole monomer. Film synthesis using this method is fast and easy and the resulting films have much higher conductivities than films synthesized by chemical methods.

Electrochemical polymerization is performed in an electrolytic solution, composed of pyrrole monomer and an electrolyte salt dissolved in an appropriate solvent. The choice of solvent and electrolyte are important because both must be stable at the oxidation potential and must be conductive [8]. The monomer solution is typically subjected to electrochemical oxidation in a three electrode cell, containing an anode

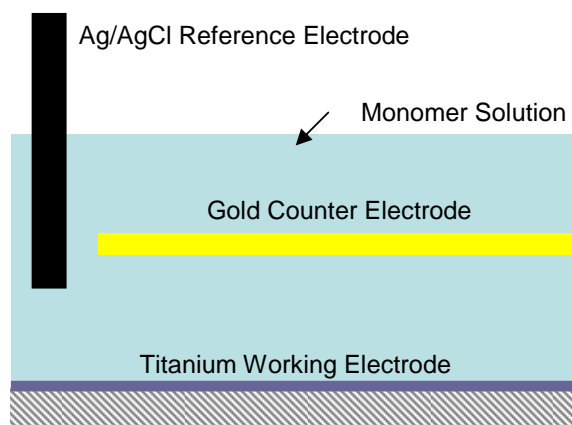


Figure 3-7) Graphical representation of a three electrode electrochemical cell. Polypyrrole films form on the working electrode surface by applying a potential between the reference and working electrodes while controlling current through the counter electrode.

(working), a cathode (reference), and a counter electrode (see Figure 3-7). An oxidizing potential is galvanostatically or potentiostatically applied between the anode and cathode while current to the anode is controlled through the counter electrode. The oxidizing potential varies, depending on the solvents and electrolytes present in solution, but is generally on the order of ~ 0.60 V. Pyrrole monomer is oxidized to a radical cation form (see Figure 3-5A), which then reacts with a second radical cation of the monomer to produce a dimer (see Figure 3-5B). Since dimers and oligomers oxidize at roughly the same potential as the monomer, the oligomers also become oxidized to a radical cation form (see Figure 3-5C) and the polymerization reaction continues to extend the polymer chain (see Figure 3-5D). A PPy film forms on the anode a few seconds after anodic current flow is initiated. The film continues to grow until the applied potential is reduced below the oxidizing potential.

While the thickness of the resulting PPy film is typically controlled by controlling the amount of electric charge passed through the working electrode during polymerization [176], other reaction parameters also have an impact on the process. The polymerization reaction is sensitive to a wide range of parameters including solution temperature, the concentration of solvents and ions, and the shape, size, and material composition of the working electrode. One major complication in the electropolymerization of polypyrrole is the fact that all of these reaction parameters are interdependent. Difficulties arise in correlating polymer properties with the conditions of synthesis. A great deal of effort has been exerted to understand the interdependency of reaction parameters during polymerization.

Films have been synthesized at a wide range of temperatures, from -20 °C to 75 °C [169, 177]. Otero *et al.* found a linear relationship exists between solution temperatures and polymer production [178]. Experimental chronoamperograms showed increased current densities flowing through the working electrode at increased temperatures. The increased current densities resulted in more charge passing through the working electrode and, thus, more polymer being synthesized. The maximum current density was found at 40 °C. Further increases in temperature resulted in decreases in the current density. While polymerization occurs at a higher rate at higher temperatures, films formed at lower temperatures have a more regular polymer structure [8]. At higher temperatures, there are an increased number of side reactions and nucleophilic attacks on radical cations that cause the formation of structural defects. Resulting films have lower conductivities.

Otero *et al.* found that increases in monomer concentration produce non-linear increases in the polymerization rate [178]. The polymerization rate (R_p) can be related to monomer concentration by the equation:

$$R_p = k_p[\text{pyrrole}]^{0.6},$$

where k_p is the propagation rate constant of radical polymerization and $[\text{pyrrole}]$ is the concentration of monomer. The relationship between monomer concentration and polymerization rate might be dependent on the availability of monomer to participate in the polymerization reaction.

The choice of electrolyte is important because 30% of the weight of the resulting polymer film is made up of dopant [8]. The anion can be organic or inorganic and can be a range of sizes (from chloride to sodium dodecylbenzenesulfonate). The electrolyte should be soluble in the chosen solvent and the anion's oxidation potential should be higher than the monomer's. Otero *et al.* reported that increases in electrolyte concentration had a non-linear effect on the polymerization rate. The polymerization rate is related to electrolyte concentration by:

$$R_p \propto [\text{Electrolyte}]^{0.8},$$

where [Electrolyte] is the concentration of electrolytic salt in solution. Changes in concentration could have an effect due to changes in the conductivity of the electrolyte [179].

Monomer and electrolytic salts are typically dissolved in aqueous solutions. However, non-aqueous solutions are sometimes used to prepare PPy films with different conductivities and morphologies [166, 180]. The main requirement of the solvent is that it must minimize nucleophilic reactions [8]. A commonly used non-aqueous solvent is acetonitrile. Pyrrole diluted in acetonitrile has an oxidation potential 200 mV higher than in water. Ko *et al.* believe this difference is most likely due to the fact that pyrrole molecules dissolve more completely in acetonitrile while radical cations dissolve more completely in water. Cyclic voltammograms (CVs) during polymerization show that PPy films synthesized in acetonitrile have higher electrochemical reversibility than films synthesized in water. This suggests that electron transfer is slower in water than in acetonitrile. Preparation in aqueous and non-aqueous solutions appears to result in films of virtually the same mass for the same amount of charge. Thus, solvents do not have a significant effect on the coulombic efficiencies of PPy film formation [180]. In general, PPy films synthesized in non-aqueous solutions have better conductivities and are more crystalline. Films prepared in acetonitrile feature a well-defined π -conjugated backbone. By contrast, films prepared in water are more porous and contain hydroxide and/or carbonyl groups along the backbone. These films have higher resistances due to the shorter chain lengths and higher number of defects. Imanishi *et al.* suggest that the influence of the solvent on the polymerization reaction is due to its basicity and polarity [181]. Film formation is affected by the interactions between solvent and cation radicals. Solvent polarity affects the strength of these interactions while solvent basicity affects film formation.

Because PPy films nucleate on the surface of the working electrode, the films are constrained by the size and shape of the electrode. Furthermore, electrodes of micro- and nano-scale dimensions produce responses that are dependent on their geometry. Larger electrodes ($> 1 \text{ mm}^2$) have a large surface area compared to the solution volume. This allows them to effect compositional changes on bulk concentrations of electroactive species. Micro-scale electrodes ($< 1 \text{ mm}^2$) have a relatively small surface area as compared to solution volume, allowing them to probe the system while not substantially disturbing it. Ultramicroelectrodes (UMEs) are electrodes having one dimension, called the critical dimension, less than $25 \text{ }\mu\text{m}$ in size [132]. This critical dimension is smaller

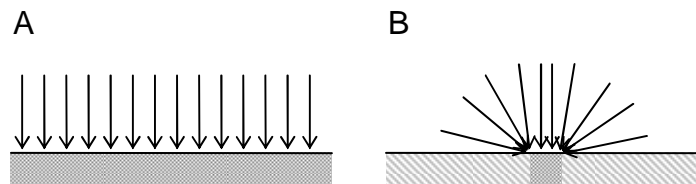


Figure 3-8) Graphical representation of A) a planar electrode and B) a band ultramicroelectrode. The arrows represent the direction molecules may diffuse to and from the electrode surface.

than the volume of solution the electrode perturbs in unmixed solutions. Large electrodes and microelectrodes are large enough to be considered infinite or semi-infinite planes. Diffusion to the electrode surface is limited to the normal direction (see Figure 3-8A). By contrast, UMEs allow for diffusion from a wider range of directions. The critical dimension of band UMEs is the electrode width, with the length considered infinite. Diffusion to the band UME surface is semicircular, approaching 2π (see Figure 3-8B). This leads to steady state or quasi-steady state diffusion controlled currents that resemble the response of hemispherical (2π) or spherical (4π) electrodes [132]. The range of directions that species can diffuse to and from the surface of UMEs is increased as the electrode size decreases. This suggests increased reaction rates at the electrode surface for diffusion-limited reactions such as the electropolymerization of PPy [129]. Radical cations generated during electropolymerization at the surface of a band UME will diffuse into the bulk solution more readily for smaller electrodes. These products are removed from participating in further chemical and electrochemical reactions at the electrode surface, having a profound effect on PPy polymerization with nano-scale electrodes.

In some cases, the electrode material can have an effect on the polymerization reaction rate. If the electrode does not uniformly conduct electricity, PPy will nucleate and propagate in the less resistive areas of the electrode. This might affect film uniformity or might slow PPy film formation at the electrode surface. Sometimes metal electrodes develop oxides on the surface that can slow or inhibit current flow through them. In turn, this phenomenon will slow or inhibit the polymerization reaction at the electrode surface. If active metals are used as electrode material, anodic polarization of the anode can lead to dissolution of material and passivation of the electrode [182]. In this case, metal dissolution and passivation occur more quickly than polymer can be electrodeposited. As a result, polymer films cannot form on the electrode surface. However, if the electrode is an inert metal such as Au, Pt, or glassy carbon, and if the

electrode conducts current uniformly, its participation in the polymerization reaction is negligible [182, 183].

3.1.3 *Summary*

Polypyrrole is a conjugated polymer that is chemically stable, easy to prepare, and highly conductive. Using electrochemical methods, high quality films can be synthesized at room temperature and under aqueous conditions. An electrically active scaffolding material is required to act as a template for the formation of the PPy films. Carbon nanofibers are one possible scaffolding material for the synthesis of PPy nanocomposites. Tunable PPy films on the surfaces of arrays of carbon nanofibers would be particularly useful for the selective modification of features in membrane devices. Reducing the spacing of the CNFs within a membrane device by increasing their diameters might enable molecular-scale size selectivity. To achieve this goal, a greater understanding of the deposition of PPy films of nanometer thicknesses is necessary. The electropolymerization of PPy on the surfaces of nanoscale structures, such as CNFs, requires particular attention.

3.2 *Depositing Nanometer Thin Polypyrrole Films on VACNFs*

Examples of polypyrrole electropolymerization on the surfaces of carbon nanotubes exist in the literature. Stochastically grown forests of bulk addressed vertically aligned carbon nanotubes have been modified with thin polypyrrole coatings (10 – 93 nm) to alter electrical properties or surface chemistries [184, 185]. However, the issue of depositing PPy films of tailored nanometer thicknesses has largely been ignored in these studies. In order to explore this issue, certain reaction parameters were first evaluated by synthesizing PPy films on gold planar electrodes [106]. This allowed for accurate film measurements to be made using an atomic force microscope (AFM). After evaluating the reaction parameters and selecting the variable that offered the most reproducible and tunable PPy coatings, the polymer was deposited on the sidewalls of CNFs.

3.2.1 *Controlling Polypyrrole Film Growth on Planar Electrodes*

The effects of polymerization reaction time, monomer concentration, and applied bias on film formation were evaluated to determine the relative degrees of control afforded by each parameter on the electropolymerization of pyrrole. The variables were judged by the degree to which each variable induced reproducible and linear responses in growth rate and quality. Variables such as pH and temperature were also considered as mechanisms to control electropolymerization, but both of these variables can only be applied within a narrow range of values. If this range is exceeded, the experimental conditions have deleterious effects on biomolecules and detrimental effects on the resulting polymer films.

PPy has a tendency to shrink when dehydrated and swell when hydrated. There is a significant difference between the two states (~7% volume) [162]. As a result, it was desirable to study the PPy films in the environment in which they would typically be used, i.e. in aqueous solution. However, characterizing PPy films in aqueous solution prevented the use of many commonly available characterization instruments, such as conventional electron microscopy tools. The sub-micron thicknesses of the films added further restrictions and made the use of tools such as the profilometer impractical. The AFM was chosen as the PPy film characterization tool because it can be used to examine samples in aqueous media at sufficiently high resolutions.

To construct planar electrodes, metal layers were first deposited on SiO₂ wafers using electron beam evaporation (100 Å Ti, 2000 Å Au). Then the wafers were diced with a wet dicing saw into strips 0.5 cm wide and 4 cm long. Monomer solutions were prepared in 300 mM KCl and 10 mM H₂SO₄ in 1.5 mL centrifuge tubes. A coiled platinum wire was used as the counter electrode and a Ag/AgCl (3M KCl) electrode with a glass frit membrane was used as the reference. The counter, reference, and diced gold strips were placed in the monomer solution. A constant potential was then applied using an electrochemical workstation with the reference electrode acting as the cathode and the diced gold strips acting as the anode. The effects of three electropolymerization growth parameters were explored: polymerization time, monomer concentration, and applied potential. Films were synthesized in a range of experimental conditions by varying these three growth parameters. For variable polymerization time experiments, the monomer concentration was held at a constant 20 mM of pyrrole. The applied potential was 0.65 V for polymerization times ranging from 15 to 180 seconds. For variable monomer

concentration experiments, a potential of 0.65 V was applied for 15 or 45 seconds in monomer solutions containing 10 to 500 mM pyrrole. For variable potential experiments, a 20 mM monomer solution was prepared. Potentials covering a range of 0.7 to 1.0 V were applied for 15 seconds.

To assess the polypyrrole films on the gold electrodes, an area of polymer was typically scraped from the electrode using forceps. This provided the abrupt change in height necessary for thickness measurements. PPy film thicknesses were determined by measuring the difference in heights between the film and the underlying gold substrate. AFM measurements were made in aqueous solution (300 mM KCl, 10 mM H₂SO₄) in three separate areas of each film and on multiple samples (n = 2 – 4). Figure 3-9 shows a collection of data collected in this manner.

The graph in Figure 3-9A illustrates the relationship between PPy film thickness and polymerization time. The reaction time was found to significantly affect the resulting polymer films. Polymer films appeared to form relatively slowly before the growth rate stabilized and became linear with time. This matches previously reported behavior, which attributes the slow initial growth to the relatively slow rate at which polypyrrole will nucleate on the surface of the anode. Once a layer of polymer forms on the anode, the electrode essentially becomes a PPy electrode irrespective of the underlying electrode material. At this point, the film formation rate at the surface is much higher and roughly equivalent to the rate at which the polymer chains extend [178]. After the initial “lag”, film thicknesses increased at a linear rate of 2.6 nm/s. Film thicknesses varied across the electrode surface by about 7% of the total thickness. Measurements between samples showed a variance of about 8%, closely matching the intra-sample variance. This variance remained virtually constant over the range of polymerization times investigated.

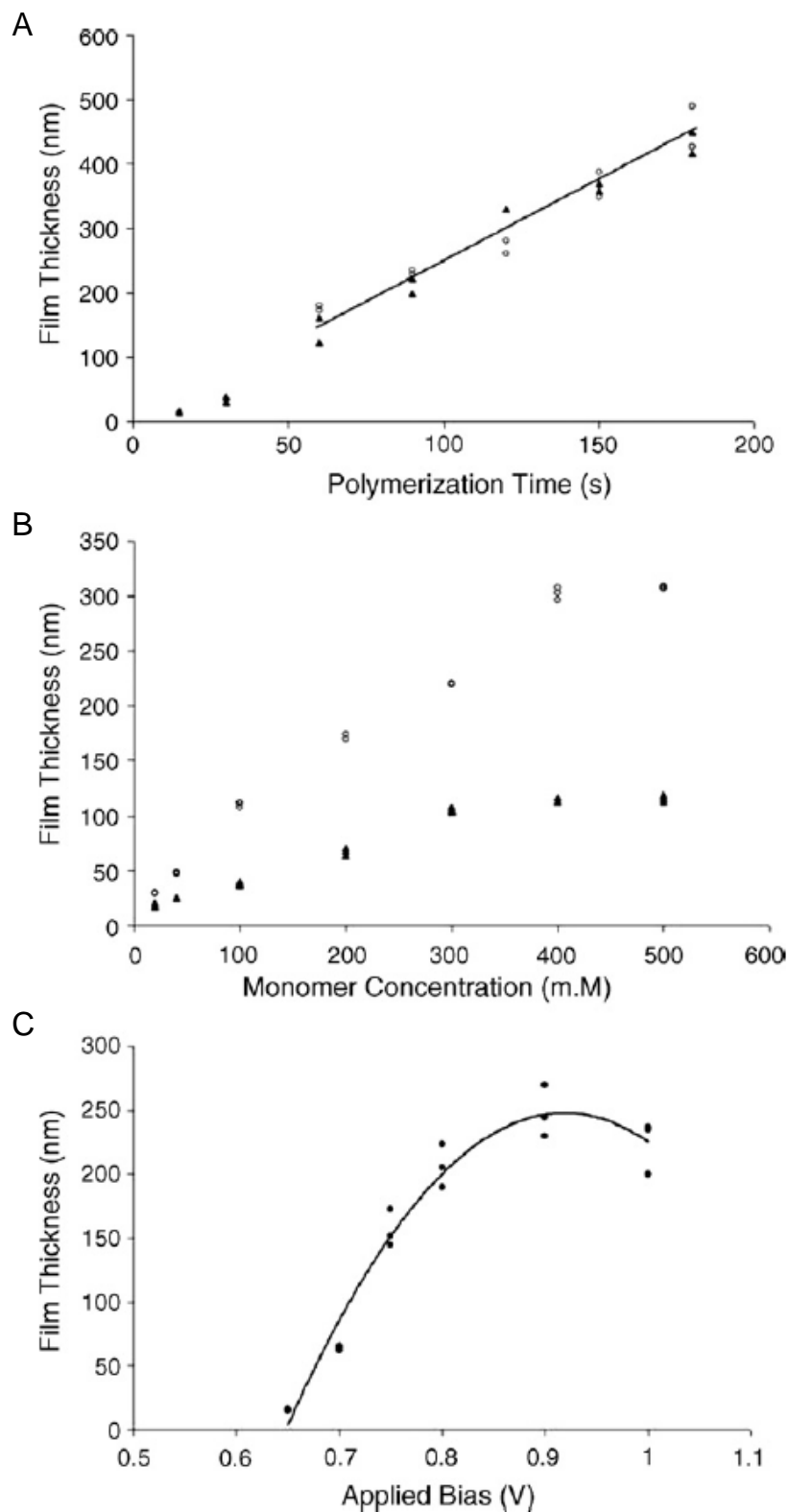


Figure 3-9) Planar PPy film thickness vs. **A)** polymerization time, **B)** monomer concentration, and **C)** applied bias. Data points in **A)** represent two separate PPy films (sample 1 (\circ) and sample 2 (\blacktriangle)). Data points in **B)** were from samples polymerized for 45 s (\circ) and 15 s (\blacktriangle). A second order polynomial trend line was fitted to data in **C)**.

Variations in monomer concentration also had an effect on polypyrrole film formation. Polymerization times of 15 seconds and 45 seconds were used at an applied bias of 0.65 V to synthesize the PPy films. Figure 3-9B shows resulting film thicknesses plotted as a function of monomer concentration. At the lower monomer concentrations, film thickness linearly increased with increases in monomer. The rate of film formation was 3 Å/mM monomer for the 15 second reactions and 7 Å/mM monomer for the 45 second reactions. As the polymerization time increased, the variations in monomer concentration had a more pronounced effect. There was a noticeable leveling off in the growth rate at the highest monomer concentrations, likely due to the limited solubility of the monomer in aqueous solutions. The pyrrole monomer concentrations depicted in Figure 3-9B are based on the assumption that monomer was completely solubilized in aqueous solution, but the higher monomer concentrations approach the solubility limit of 45 milligrams of pyrrole per gram of water [186]. As a result, the monomer in the solutions of indicated higher concentration was likely not completely solubilized.

Figure 3-9C shows resulting PPy film thicknesses over a range of applied voltages. The films were polymerized in 20 mM monomer for 15 seconds. At applied potentials greater than 0.8 V, film thicknesses decreased with further increases in potential. Either the polymer films began to degrade as the voltage increased or electrolytic species became oxidized resulting in side reactions that interfered with film growth. Previous reports suggest that the decrease might be due to the polymer becoming overoxidized and degrading [187-189]. Films grown at the higher potentials were also less uniform than those grown at lower potentials. Intersample thickness variances for films grown at 0.9 V were twice as large as height variances for films grown at 0.65 V.

The monomer concentration and applied potential had a demonstrated effect on the polymerization process. By increasing the concentration of monomer in solution, it was possible to increase the rate of polymerization at the anode surface. Resulting films showed a linear dependence between monomer concentration and film thickness. The effect became more pronounced at longer polymerization times. Varying the amount of monomer concentration in solution might be an effective method of controlling the deposition of thicker films (< 1 μm). For nanoscale PPy films, varying solution compositions is cumbersome. Variations in applied bias appeared to produce a linear response in the film growth rate over a limited range of values (0.6 V – 0.85 V). In the linear regime, growth rates increased at a relatively high rate with small changes in

applied potential. Controlling film formation at the nanoscale by controlling applied potentials would require an extremely accurate reference electrode and potentiostat. It is much preferable to control the reaction times as a means of controlling the resulting polymer film thickness. The relationship between polymerization time and film thickness is linear and easily adjusted. However, because of the complexity of the electropolymerization reactions and because of the dependence of the reactions on the geometry and physical properties of the electrodes and the electrochemical cell, the relationship between polymerization time and film thickness must be quantified for different experimental set ups. Once this relationship is established, PPy films of reproducible thickness can be repeatedly synthesized.

3.2.2 *Controlling Polypyrrole Film Growth on Carbon Nanofibers*

By adjusting growth parameters during synthesis, carbon nanofibers can be grown with a great deal of control over their resulting shape, location, and chemical composition [1, 5, 11, 143]. However, it is not possible to selectively modify the geometry of specific nanofibers within a group of nanofibers by altering growth parameters, as these changes affect the entire population. The electrodeposition of PPy is one method of modifying the geometry of individual or groups of VACNFs within a larger array.

To demonstrate the ability to selectively modify the geometry of VACNFs, nanofiber microelectrode devices were constructed. First, 100 Å Ti, 2000 Å W, 100 Å Ti, and 50 Å Si were deposited on SiO₂ wafers using electron beam evaporation. Then, photoresist was spin coated and nickel catalyst sites were patterned using a UV-optical projection lithography system. Catalyst sites were 500 nm in diameter at a 5 µm pitch. After a post-exposure bake and development, residual resist was cleaned from the wafer in an oxygen plasma. Nickel catalyst metal (500 Å) was deposited using electron beam evaporation and then excess metal was lifted off in acetone. Carbon nanofibers were grown in a dc-PECVD as previously described in Chapter 2. The resulting fibers were 10 µm tall and were 500 nm thick at the point 5 µm above the substrate. After PECVD growth, the wafers were spin coated with a layer of photoresist; metal interconnects were then patterned using contact lithography. After development, residual resist was removed in an oxygen plasma. Metal in the exposed areas of the wafer was etched away using a SF₆/O₂/CF₃ based plasma. This allowed for electrical addressability to

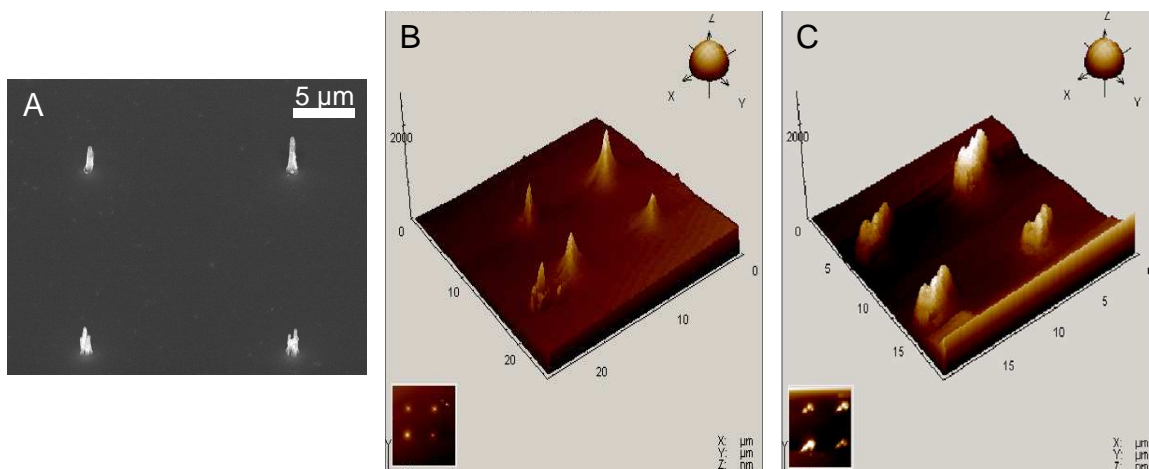


Figure 3-10) A) Electron micrograph of an array of VACNFs. AFM scans of the same VACNFs B) prior to polymerization of PPy and C) after.

specific VACNFs, while leaving other VACNFs unaddressed. The wafer was stripped of excess photoresist and the interconnects were wire bonded to a printed circuit board. A fluidic well was painted on the device using a circle of epoxy.

The conditions for PPy film deposition on the VACNFs were selected based on the results from the planar PPy film experiments. Pyrrole monomer was diluted at a 20 mM concentration in 300 mM KCl and 100 mM H₂SO₄. Monomer solution was then pipetted (~100 μL) into the epoxy fluidic wells of the VACNF microelectrode devices. A single lead of these devices would be connected to the electrochemical circuit as the working electrode. An Ag/AgCl reference electrode and platinum wire counter electrode were positioned above the droplet of monomer so that the tips were immersed but not touching the device. Then, 0.75 V was applied for a range of polymerization times, from 15 to 105 seconds. The structures were then washed in deionized water, dried, and examined in a scanning electron microscope (SEM).

Initial attempts to analyze the PPy-coated CNFs were pursued using an AFM in aqueous solution (see Figure 3-10). The probe tip of an AFM is what allows the tool to collect nanoscale measurements. However, commonly used probe tips are not sharp enough to record accurate measurements from tall, high aspect ratio structures such as VACNFs. High aspect ratio AFM tips are available and do produce improved results, but these probes are significantly more expensive and more fragile than conventional tips. Furthermore, to receive a response from the AFM's scanner, the high aspect ratio tips have to be rastered at a relatively slow 0.1 lines/s (~10 times slower than conventional tips).

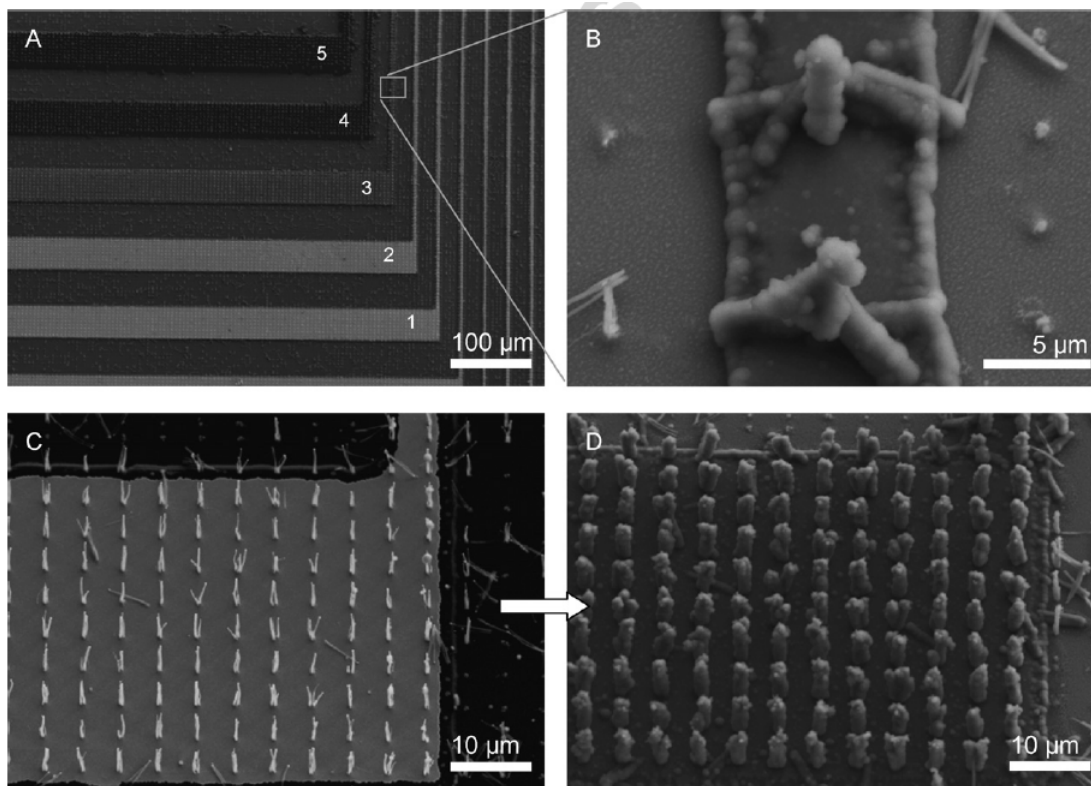


Figure 3-11) SEM images of VACNFs selectively modified by polypyrrole. **A)** The electrical lead labeled 1 has not been polymerized. Leads 2-5 are progressively darker because they are coated with a progressively thick layer of PPy. **B)** CNFs on the metal lead are polymerized while surrounding CNFs on the SiO₂ substrate are not. **C)** CNFs prior to polymerization and **D)** after.

To reduce the aspect ratio and allow for the use of conventional AFM tips, VACNFs were buried in a photoresist layer that left ~500 nm of exposed carbon nanofiber. Variations in nanofiber heights, and thus the amount of exposed tip, made it necessary to characterize the same individual nanofibers prior to polymerization and after. Additional complications resulted from the photoresist itself. Typical solvents for photoresists, such as methanol and acetone, have detrimental effects on many organic polymers like PPy. The photoresist also appeared to reduce the amount of polymerized pyrrole being produced and decreased the observed oxidation currents. This could have been due to partitioning of the pyrrole into the photoresist matrix. As a result of these complications, many conventional processing techniques that involve photoresist patterning and electropolymerization of pyrrole have to be avoided. Furthermore, even after burial in photoresist, the nanofibers still have aspect ratios too high for accurate measurements to be made with conventional AFM tips. Attempts to use an AFM to characterize PPy-CNF nanocomposites were abandoned because of the inefficiencies, complications, and high associated costs.

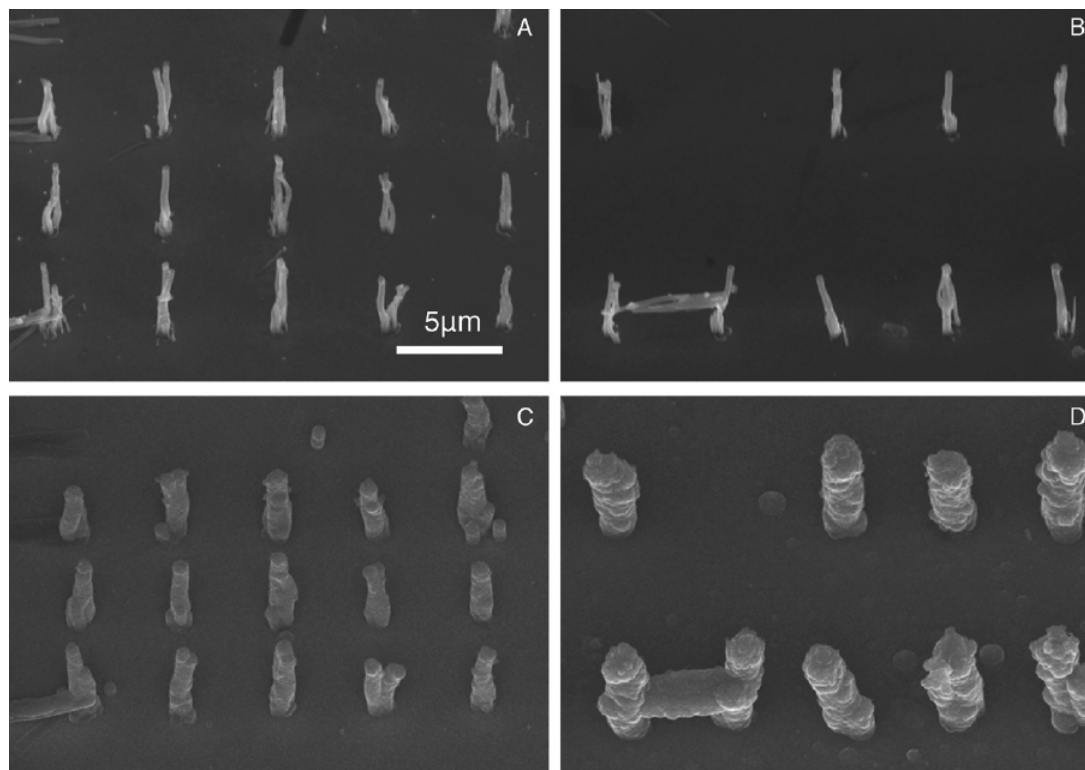


Figure 3-12) SEM images of individual VACNFs **A,B)** before polymerization and **C,D)** after. Polymerization time was 75s for the fibers in **(A)** before the image in **(C)** was collected. Polymerization time was 115s for the fibers in **(B)** before the picture in **(D)** was collected.

Instead, PPy films deposited on individual CNFs were dried and then characterized by SEM. While differences do exist between hydrated and dehydrated PPy films, the geometric differences are predictable [162]. Applied bias and monomer concentration were held constant during experiments, while a range of polymerization times were used. PPy films were synthesized on specific groups of VACNFs by applying potentials to the metal leads addressing them. This restricted PPy synthesis to the CNFs on the metal leads, while surrounding CNFs remained unchanged. As seen in Figure 3-11, the CNFs on metal leads could be selectively modified with PPy coatings. In Figure 3-11A, electrical leads are coated with PPy films of varying thicknesses. The darker colored leads have a thicker coating of PPy than the lighter colored leads, due to their different polymerization times. Surrounding VACNFs, grown on the SiO_2 substrate, are not electrically addressed and have not been modified by PPy (see Figures 3-11B – 3-11D).

Polypyrrole films were analyzed by comparing individual carbon nanofibers prior to PPy deposition and after (see Figure 3-12). As observed from studies of PPy films deposited on planar gold electrodes, polymerization time induced a reproducible, linear

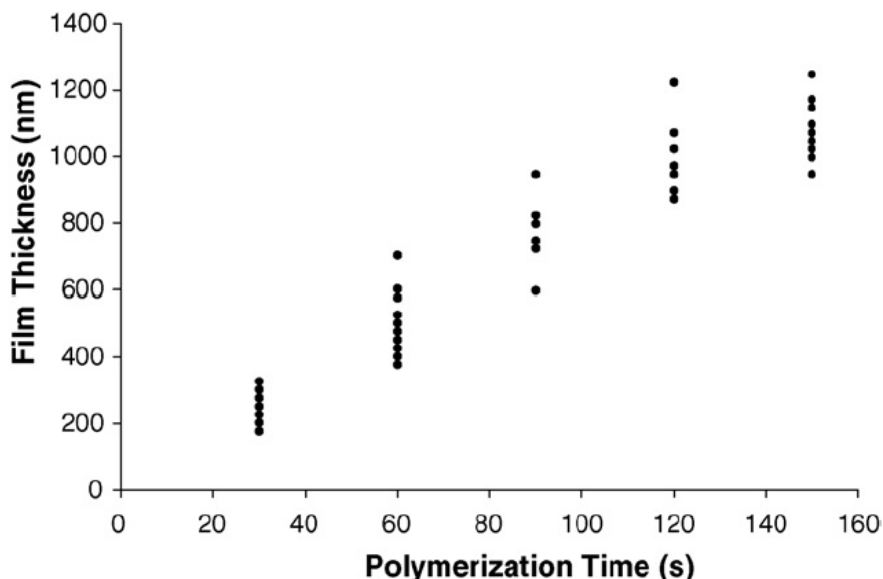


Figure 3-13) A graph depicting the relationship between polymerization time and resulting PPy film thickness. Data points represent measurements made on individual CNFs.

response in polymer film thickness. The PPy films deposited on the CNFs appeared to become rougher (more non-planar) as polymerization time and film thickness increased. This could have been due to the relatively high bias applied during polymerization. CNF surface defects might also have become exaggerated as the PPy films became thicker. A third factor might have been due to sputtering of the substrate on to the CNFs during nanofiber growth. This would lead to passivation of certain areas of the nanofiber surface, resulting in areas of higher electrochemical activity and non-planar film formation.

The relationship between polymerization time and PPy film thickness on CNF electrodes can be seen in Figure 3-13. The data points on the plot represent PPy film thicknesses measured from individual nanofibers in the SEM. A linear relationship between film formation and polymerization time was observed. PPy films increased in thickness at a rate of 9 nm/s, nearly three times faster than the rate of film formation on planar gold electrodes. The range of directions that species can diffuse to and from the carbon nanofiber microelectrodes is greater than for planar electrodes. This means that reactants are replenished and byproducts are removed more quickly from the electrode surface [129]. The result is an increase in reaction rates and, thus, polymer film thickness.

Once the relationship between polymer film thickness and polymerization time was established, PPy films were deposited with reproducible thicknesses. The sub-

micron films were surprisingly consistent, given the variability in the surface chemistry and geometry of the nanofibers. The variability in film thicknesses observed in Figure 3-13 is largely due to these physical differences. Visual inspection of the nanofibers showed that the polymer films were becoming progressively rougher as they became thicker. The roughness might be diminished by polymerizing at slower reaction rates or by subjecting the carbon nanofibers to further microfabrication processing to improve the uniformity of their electrical conductivity.

3.3 *Conclusions*

The ability to control the electrodeposition of nanoscale coatings of polypyrrole by controlling certain reaction parameters was evaluated. Experiments on gold planar electrodes demonstrated that monomer concentration, applied bias, and polymerization time are all important factors in determining the rate of polypyrrole film formation on the surface of the anode. However, polymerization time was found to have a relatively large, linear relationship with polymer film thickness (2.6 nm/s at 0.65 V, 20 mM monomer), as compared to applied bias or monomer concentration. As a result, this reaction parameter was chosen to direct the deposition of nanoscale coatings of PPy on the surface of specific VACNFs within an array. The ability to controllably and reproducibly modify selected individual VACNFs was then demonstrated and quantified.

The ability to tailor the size of nanostructures in a highly controllable way is extremely desirable in constructing membrane structures. The interfiber spacings of vertically aligned carbon nanofibers within a membrane might be tuned to desired dimensions, enabling the construction of nanoscale pores capable of trapping molecules as small as proteins and DNA. Polypyrrole also effects volume changes in response to applied electrical stimuli. By actuating PPy-coated carbon nanofibers, it might be possible to create gateable nanopores.

Chapter 4

Actuatable Membranes Constructed from Polypyrrole-Coated VACNFs

Constructing and integrating nanoporous membranes within multi-scale systems, while retaining the ability to regulate the transport of particles with precision, selectivity, and control, remains a difficult challenge. In the work for this chapter, synthetic membranes were created by the deterministic growth of vertically aligned carbon nanofibers. Interfiber spacing was modified by coating the VACNFs with polypyrrole. The resulting PPy-VACNF membrane devices were integrated within a microfluidic manifold. Transport of species through the VACNF membranes was affected by actuating the PPy-coating to alter the size of the membrane pores. The synthesis of PPy-VACNF membranes, integrated within multi-scale devices, is described. The ability to alter the permeability of the PPy-VACNF membranes by actuation of the polypyrrole coating is demonstrated.

4.1 *Actuation of Polypyrrole*

The π -conjugated polymer backbone of polypyrrole is composed of alternating single and double bonds (see Figure 4-1A). If electrons are removed from the polymer, resulting free electrons become delocalized along this backbone (see Figure 4-1B) [6]. Removal of electrons (oxidation) occurs during electropolymerization when an oxidizing potential is applied to pyrrole monomer to initiate polymerization. In its oxidized state, PPy has 0.25 – 0.33 cation centers per pyrrole monomer. This positive charge on the polymer backbone is balanced during polymerization by the incorporation of anions from the electrolytic solution. Anions are held in place by a hydrogen bond at the NH moiety of the pyrrole ring (see Figure 4-1C). After electropolymerization, resulting polypyrrole films are removed from the monomer solution. To actuate, the polymer is immersed in an electrolytic solution. Three electrodes (counter, reference, and working) are also

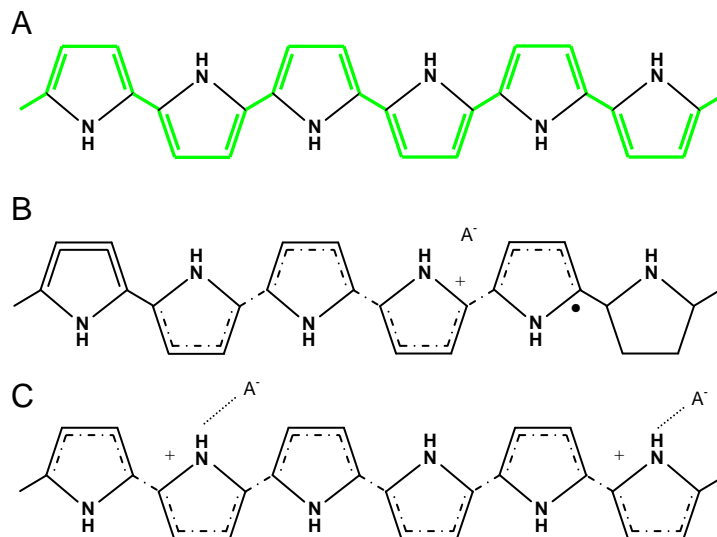
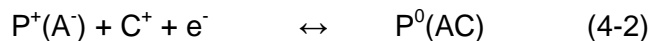
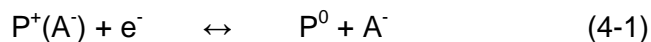


Figure 4-1) Polypyrrole at different oxidation levels. **A)** Undoped (neutral), **B)** partly oxidized, **C)** and highly doped (oxidized) PPy. Anions (A^-) are incorporated within the polymer matrix to balance the positive charges on the polymer backbone. The single and double bonds that make up the backbone are highlighted in green.

immersed in solution and are used to galvanostatically or potentiostatically apply potentials to the polypyrrole films.

Polypyrrole volume expansion and contraction is related to the insertion and expulsion of ions that occurs when the oxidation level of the polymer is changed. An extremely important factor in the actuation of polypyrrole is the nature of the electrolytic salts present when electric potentials are applied to the polymer. The electrolyte can be composed of cations and anions of a wide range of sizes. These ions enter the polymer matrix in either the oxidized (equation 4-1) or reduced (equation 4-2) states:



where P^+ represents the oxidized state and P^0 represents the reduced or neutral state of the polymer. $P^+(A^-)$ indicates that the anion A^- is incorporated within the polymer matrix as a dopant and $P^0(AC)$ indicates that a cation is inserted into the matrix. When the polymer is oxidized, anions from solution are incorporated within the polymer matrix. When the polymer is reduced to a neutral state, it either expels the anions from the matrix (equation 4-1) or incorporates cations into it (equation 4-2).

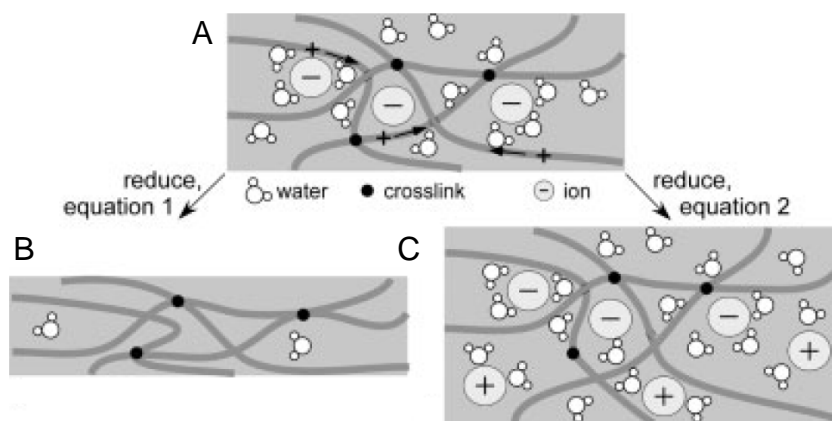


Figure 4-2) A graphical depiction of the **A)** oxidized state of the polymer. Positive charges on the polymer backbone are balanced by anions. Solvent is also present due to osmotic pressure. **B)** Reduced, uncharged state if the anions are small. **C)** Reduced state if anions are large and immobile. Adapted from Smela [6].

The mobility of ions within polypyrrole is dependent on the hydrophobicity of the polymer matrix and on the size of the ions, typically described by their Stoke's radius [9]. Large ions cannot enter the polymer matrix because their physical size does not allow them to fit through the gaps in the intertwined polymer chains. Smaller ions can enter the polymer but their mobility may be limited by the hydrophobicity of the polymer.

Anions in solution are incorporated within the oxidized polymer during electropolymerization to balance charge. As polymerization proceeds, polymer chains grow around the anions and encapsulate them (see Figure 4-2A). The hydrophobicity and the sizes of the pathways into the polymer matrix are greatly affected by these incorporated anions. For instance, the long aliphatic carbon chain present in dodecylsulfate promotes hydrophobicity in the surrounding polypyrrole material. This, in turn, facilitates rapid incorporation of cationic molecules within the polymer matrix upon reduction [190]. If the incorporated anions have large Stoke's radii, like sodium dodecylbenzenesulfonate (NaDBS), then the anions become trapped and are effectively immobilized within the polymer matrix. When a polymer that incorporates large anions is reduced, the anions cannot be expelled. Instead, small cations from the surrounding solution must rush into the polymer matrix to compensate for the charge. The polymer matrix swells to create spaces for the cations and the polymer volume increases (see Figure 4-2C). Upon a return to the neutral or oxidized state, cations are ejected from the polymer and the free spaces and voids left behind are filled in by adjacent polymer chains, leading to a decrease in polymer volume [9]. For large, immobile anions, the process in equation 4-2 dominates.

If the anions incorporated during electropolymerization are small and mobile, like chloride (Cl^-), then they readily move in and out of the polymer. When polypyrrole is oxidized, small anions insert into the polymer matrix, swelling it and leading to an overall increase in polymer volume. Upon reduction to a neutral or reduced state, anions are expelled from the polymer and the spaces they vacate are filled in by the surrounding polymer chains leading to a corresponding decrease in polymer volume (see Figure 4-2B). For small, mobile anions, the process in equation 4-1 is dominant. For medium sized anions, both processes in equations 4-1 and 4-2 occur. This causes the actuating polymer to behave erratically, vacillating uncontrollably between expanded and contracted states. As a result, medium sized anions are typically avoided for applications requiring polypyrrole actuation.

When an oxidizing or reducing potential is applied to polypyrrole in a solution with low electrolyte concentration, the appropriate ions will move in and out of the polymer to balance charge. However, a small number of counter-ions will also move in and out of the polymer if they are sufficiently small enough [3]. If an oxidizing or reducing potential is applied in a high electrolyte concentration, large numbers of both cations and anions will move in and out of the polymer matrix so long as their mobility is not limited by their size or polymer hydrophobicity. The uncontrolled movement of cations and anions into and out of the polymer is undesirable. When a reducing potential is applied, it is preferable to only have cations be mobile within the polymer. Likewise, when an oxidizing potential is applied, it is desirable to only have the anions be mobile. Thus, careful planning is required in selecting which anions to incorporate within the polymer matrix during electropolymerization and which electrolytic salts to use in polymer actuation. If a large, immobile anion is captured within the polymer during polymerization then an electrolyte with a small cation and large anion is preferable for actuation. When a reducing potential is applied to the polymer, the small cations will rush into the polymer matrix to balance the charge and the large anions will remain in solution outside the polymer (equation 4-2). If a small, mobile anion is used to balance charges during electropolymerization then an electrolyte with a large cation and small anion is preferred for actuation. When an oxidizing potential is applied to the polymer, the small anions will rush into the polymer to balance the charge and the large cations will remain outside the polymer (equation 4-1).

Pei *et al.* illustrated the differences in ionic movements into and out of polypyrrole doped with small, mobile anions versus polypyrrole doped with large anions [9]. Cyclic

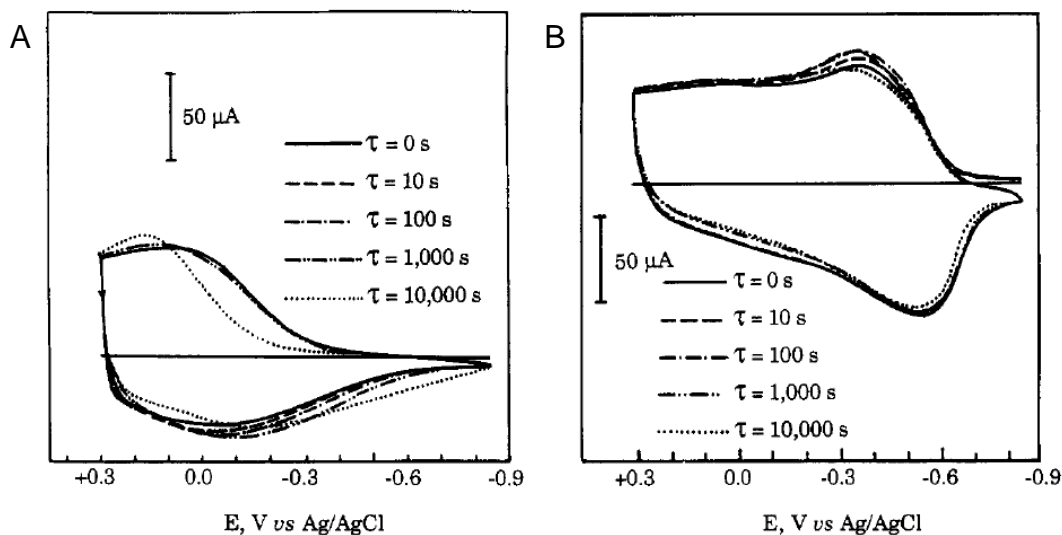


Figure 4-3) Cyclic voltammograms of **A)** PPy doped with Cl^- (small, mobile anion) in 0.1 M Et_4NCl (large cation, small anion) after being held at the positive potential 0.30 V for a certain time, τ , and **B)** PPy doped with DBS^- (large, immobile anion) in 0.1 M NaDBS (small cation, large anion) after being held at the negative potential -0.85 V for time, τ . Adapted from Pei *et al.* [9].

voltammetry was conducted in a three-electrode cell with a Pt wire counter and a Ag/AgCl reference electrode. Polypyrrole films incorporating the small, mobile anion, Cl^- , were immersed in 0.1 M Et_4NCl and were subjected to voltage sweeps at scan rates of 100 mV/s. The electrolyte contained the large cation, Et_4N^+ , and the small anion, Cl^- , to prevent cation insertion while allowing anion insertion during voltage sweeps. Resulting cyclic voltammograms can be seen in Figure 4-3A. An oxidation peak is observed in the range of ~ 0.0 to 0.3 V, due to the contributions from anion insertion/ expulsion. A reduction peak does not exist because cation insertion is negligible at reducing potentials (< -0.3 V). Polypyrrole films incorporating the large, immobile anion, DBS^- , were immersed in 0.1 M NaDBS and subjected to voltage sweeps at scan rates of 100 mV/s. The electrolyte contained a large anion and small cation, to prevent insertion of the anion at oxidizing potentials. The resulting cyclic voltammograms in Figure 4-3B show a reduction peak at -0.3 to -0.7 V, due to the insertion and expulsion of cations into and out of the polymer matrix. An oxidation peak is not observed.

Pei *et al.* observed a hysteresis effect in the first few cyclic potential sweeps applied to newly deposited PPy. This “break-in” phenomenon is caused when solvents and ions are first ejected from the polymer after electropolymerization. The polymer chains surrounding the voids left by the evacuated ions and solvents slowly relax to fill the spaces in. When ions are later reinserted into the matrix, the polymer must reopen free spaces to accommodate, causing a hysteresis in the responses. After opening,

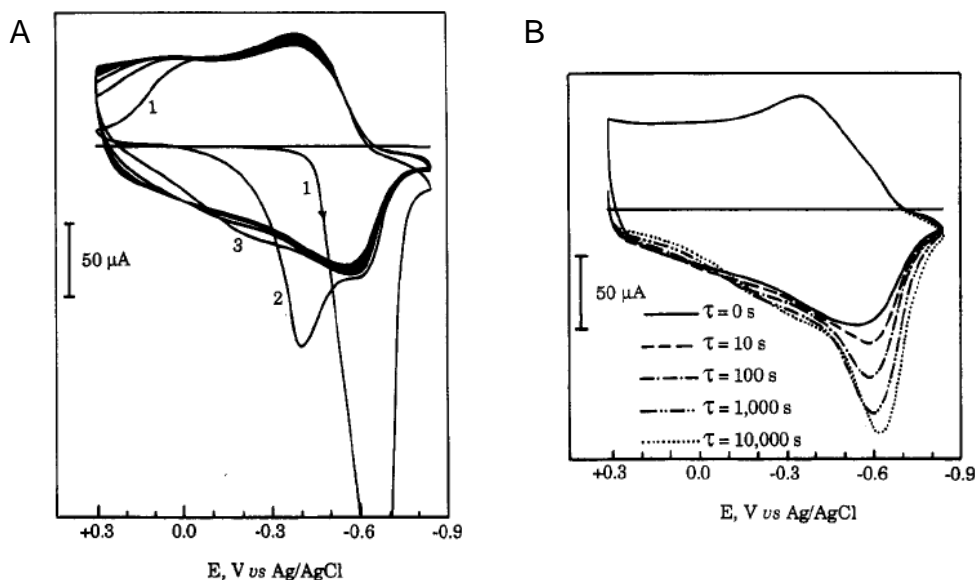


Figure 4-4) Cyclic voltammograms of **A)** freshly deposited PPy(DBS) and **B)** PPy(DBS) after being held at the positive potential 0.3 V for τ seconds. Films were immersed in 0.1 M NaDBS and were subjected to voltage sweeps at 100 mV/s. Reproduced from Pei *et al.* [9].

these spaces remain open, even after subsequent ion expulsions, until the surrounding polymer chains have time to relax to fill the voids again. The cyclic voltammograms in Figure 4-4A illustrate the initial hysteresis effect in freshly deposited PPy films. Several cycles are necessary before the voltammograms begin to overlap. To illustrate that this phenomenon is due to polymer chain relaxation, a PPy(DBS) film was held at an oxidizing potential for time τ , to expel cations from the matrix and allow the polymer chains to fill the void. The films were then immediately subjected to voltage sweeps and the resulting cyclic voltammograms are shown in Figure 4-4B. The longer the polymer chains were allowed to fill the void, the more pronounced the hysteresis effect, as shown by the progressively large reduction peaks for progressively longer hold times, τ .

The movement of solvent molecules into and out of the polymer matrix in response to ionic movements also has an effect on polymer actuation [3]. The forces driving solvent movements are due to imbalances in solvent activities between the polymer matrix and the surrounding electrolyte. The effect is similar to the osmotic pressure difference between two solutions separated by a semi-permeable membrane. Changes in the number of free ions within the polymer lead to changes in the osmotic pressures between the two phases. Free ion concentration changes are, of course, due to oxidation and reduction of the polymer backbone. Solvent is driven from/to the electrolyte to/from the polymer to counteract the pressure differences. Measurements of PPy volume change show that volume expansion decreases with increasing electrolyte

concentration (~30% decrease between 0.1 and 1.0 M). This change is attributed to polymer volume expansion due to osmotic pressure differences. The electrolyte concentration and solvent play a significant role in volume change that must be accounted for.

To summarize, polypyrrole is an electrically actuatable polymer that undergoes volume change when oxidized or reduced. The volume change is driven by the insertion and expulsion of ions within the polymer matrix to balance electrical charges on the π -conjugated backbone. Changes in the oxidation state of PPy are typically driven by electrochemical techniques. By electrochemically depositing PPy on the sidewalls of vertically aligned carbon nanofibers it may be possible to controllably alter the diameter of the nanofibers. This would enable the ability to modulate the permeability of membranes constructed from stochastic forests of VACNFs. First, a greater understanding of certain PPy actuation characteristics is required.

4.2 *Actuation to Alter the Permeability of VACNF Membranes*

To evaluate polypyrrole actuation characteristics, films were synthesized in an electrolyte that contained a large anion, dodecyl benzenesulfonate (DBS⁻) [191]. During polymerization, this anion was incorporated within the PPy matrix to balance the positive charge of the oxidized polymer. The anions are relatively large and became trapped as the polymer chains extended. Actuation of the polymer/anion matrix was controlled in a sodium dodecyl benzenesulfonate (NaDBS) electrolyte. When the PPy(DBS) film was electrochemically reduced, Na⁺ cations from the surrounding electrolyte would rush in to the polymer matrix to balance the charge, resulting in an increase in volume and swelling of the polymer. Upon a return to the neutral state, the cations were expelled from the polymer matrix and a corresponding decrease in volume occurred.

Nanoscale actuation experiments involving PPy(DBS) films have been previously reported by Smela *et al.* [112, 162]. In these experiments, the volume changes of the polymer films were characterized by atomic force microscopy. The AFM was essentially used as a highly sensitive profilometer, measuring the height difference between the underlying electrodes and the tops of the polymer films. The AFM is a preferred characterization tool for these types of experiments because it allows for *in situ* measurements in aqueous solution at high resolutions. For initial actuation experiments,

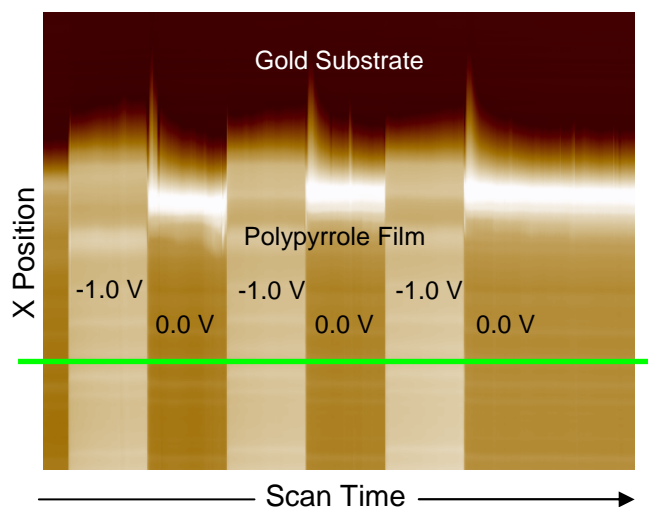


Figure 4-5) AFM image collected by continuously rastering the scan head over the same polymer area. The polymer was subjected to a series of voltages, -1.0 V followed by 0.0 V, and the resulting volume changes were observed. Longitudinal cross-sections (represented by the green line) provided accurate measurements of the magnitude of volume changes.

polypyrrole was synthesized on gold planar electrodes and film measurements were evaluated with an AFM. The stability of volume change under prolonged actuation, the reproducibility of the volume expansion/contraction after multiple consecutive actuations, and the effects of applied potential were all examined. Polypyrrole films were then deposited on the sidewalls of VACNF membrane structures. The ability to alter the permeability of these membranes was evaluated.

4.2.1 Actuation of Polypyrrole on Planar Electrodes

Planar electrodes were prepared by coating SiO₂ wafers with thin layers of metal. A 50 Å Ti adhesion layer and a 2000 Å Au conductive layer were deposited on the wafers using an electron beam evaporator. Then, the wafers were cleaved into rectangular chips ~4 cm² in area. A copper wire was affixed to the corner of each individual chip using silver-loaded epoxy to provide electrical connectivity. The silver-loaded epoxy connection was strengthened and insulated by coating with a non-conductive epoxy. To reduce current flow, the active electrode area was reduced by painting with finger nail polish (an insulator). Polypyrrole films were then electrochemically deposited on the surfaces of the gold planar electrodes. Pyrrole

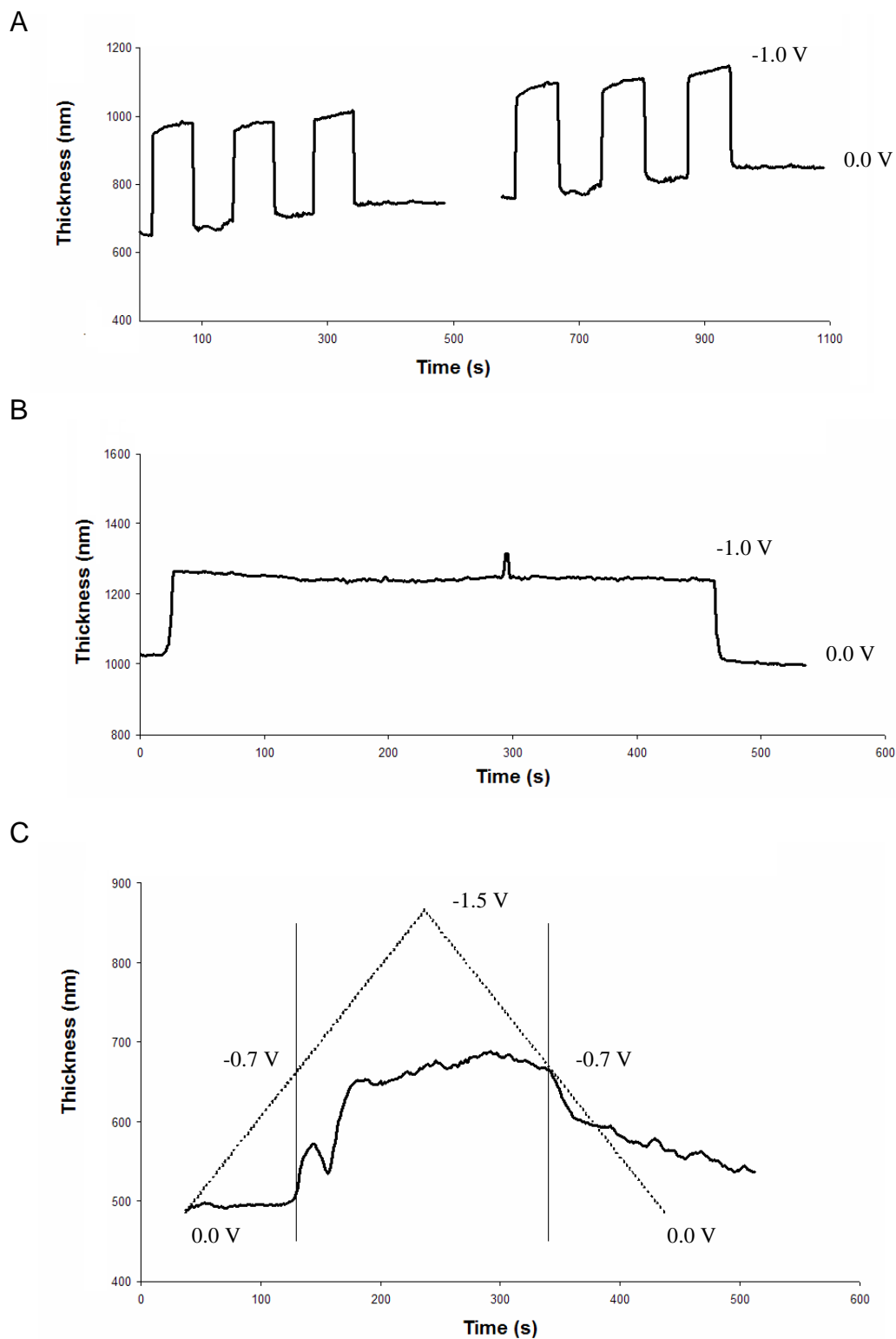


Figure 4-6) Longitudinal cross sections of a PPy(DBS) film measured by continuous line scans using an AFM. The PPy film swells when -1.0 V is applied and shrinks when 0.0 V is applied. A) Repeated actuations by applying -1.0 V for 30 s followed by 0.0 V for 30 s. B) An extended actuation by applying -1.0 V for 400 s. C) PPy actuation by applying a voltage sweep from 0.0 V to -1.0 V back to 0.0 V. The dotted line represents the corresponding voltage. The vertical lines denote where volume change occurs.

monomer was prepared as solutions of 0.1 M monomer in 0.1 M NaDBS. To oxidize the monomer, a constant voltage of 700 mV versus a Ag/AgCl reference electrode was applied for 30 seconds using an electrochemical workstation. Current at the working electrode surface was controlled through a platinum wire counter electrode.

Polypyrrole films were characterized by scraping an area of the polymer from the center of the sample with forceps. Film thickness measurements were made from the exposed electrode to the top of the films. Polypyrrole films were deposited to a ~500 nm thickness. This was on the order of the anticipated thicknesses of PPy films to be deposited on VACNFs. Polypyrrole actuation experiments were conducted in 0.1 M NaDBS solutions. Swelling and shrinking of the PPy(DBS) film was controlled by applying -1.0 V and 0.0 V versus a known reference. An AFM system operated in contact mode was used to observe the volume changes in the polymer films. Data was obtained from longitudinal cross sections of continuous line scans (see Figure 4-5). The AFM cantilever tip would raster over the same portion of PPy film for a predetermined amount of time. This allowed for accurate measurements of volume changes in the polymer. Software was written in The Mathworks Inc. Matlab 6.5.0 to extract accurate film characteristics from the resulting line scans.

A series of 6 actuations was measured by continuous line scans using the AFM. The resulting changes in film thickness versus time can be seen in Figure 4-6A. There is a slight upward tilt to the graph that is attributed to the tilt of the AFM stage. Voltages were applied to the PPy(DBS) film as a series of step potentials: -1.0 V for 30 seconds followed by 0.0 V for 30 seconds. There was an irreversible increase in film thickness, 17% larger than the original thickness, after the first actuation. This is the previously described hysteresis effect [9, 162]. When cations are first inserted into the polymer matrix, the polymer chains have to bend and shift to form voids to accommodate the inserted ions. If the cations are then expelled from the polymer, the polymer chains slowly fill the vacated voids. This process is relatively slow and until it occurs, there is an irreversible increase in the film thickness. Subsequent actuations are fully reversible with the reduced (swollen) state of the film 35% thicker than the oxidized (shrunken) state. The polypyrrole film would swell by 35% in every direction (x, y, and z planes). Continuous line scans revealed that the expansion and contraction of PPy(DBS) films being doped and undoped with Na⁺ cations occurred at a rate of about ± 100 nm/s. In Figure 4-6B, the PPy(DBS) film was swollen for an extended period of time (400 seconds). The polymer appears to remain swollen over this time period, as the volume

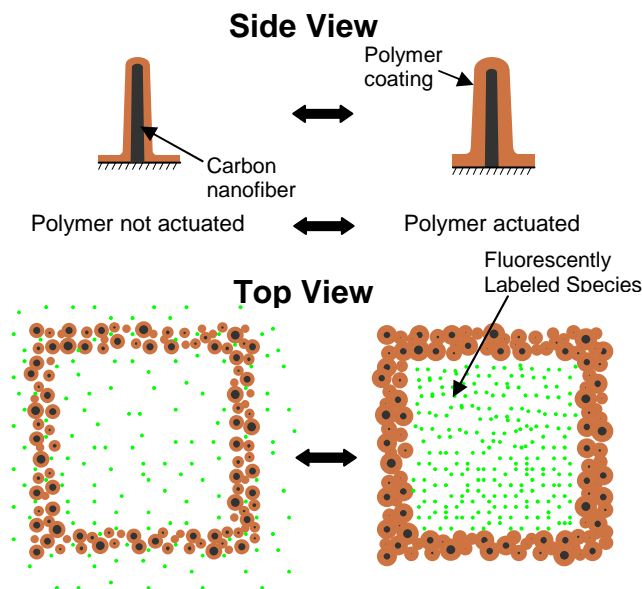


Figure 4-7) Graphical representation of a VACNF membrane structure coated with PPy before actuation of the pores (LEFT) and after (RIGHT). Transport of fluorescent species through the VACNF membrane is restricted in the actuated state.

does not significantly change during actuation. A voltage sweep, from 0.0V to -1.5 V at 10 mV/s, was applied to the PPy(DBS) film to evaluate the effect of applied bias. The resulting actuation is presented in Figure 4-6C. Volume changes do not appear to follow the applied bias. Instead, the polymer film swells and shrinks at ~ -0.7 V, close to the reported reduction potential of PPy(DBS) films in 0.1 M NaDBS solutions [192]. Further reductions in the applied potential had negligible effects on the polymer volume.

4.2.2 Actuation of Polypyrrole on VACNFs

Polypyrrole was electrochemically deposited on the sidewalls of VACNFs. Transport of variously sized fluorescent species through membranes constructed from the VACNFs was altered by actuating the polymer. The swelling of the PPy films would increase the diameter of the coated VACNFs, effectively reducing interfiber spacings. The swelling would result in a reduction in the pore sizes of the VACNF membranes, restricting flow of species through them (see Figure 4-7). The VACNF membrane structures were constructed within multi-scale devices, to allow for external application of electrical stimuli. The membranes were relatively thin, as compared to other reported

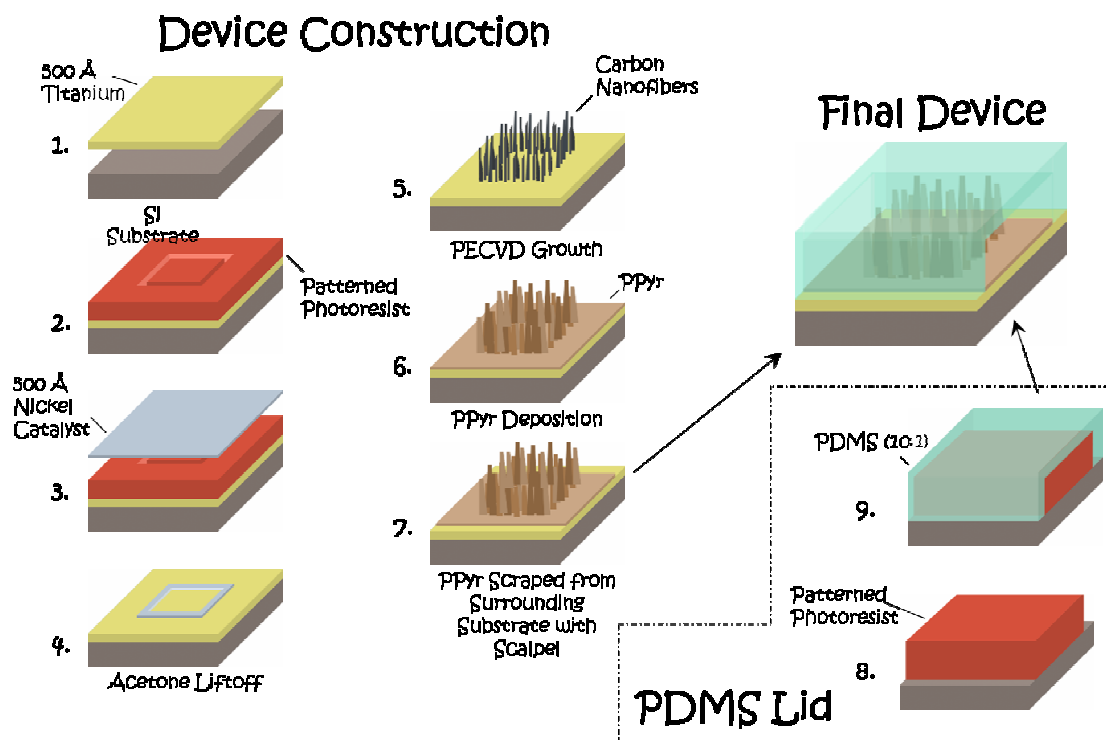


Figure 4-8) Graphical description of the fabrication process for constructing PPy-VACNF membrane structures. Steps are described within the text.

synthetic nanoporous membranes [20, 46, 73-77], allowing species to rapidly diffuse through them.

To test membrane actuation, vertically aligned carbon nanofiber membranes were first fabricated on silicon wafers. A 500 Å Ti layer was deposited on the wafers with an electron beam evaporator for bulk electrical addressability (see Figure 4-8, step 1). Generally, titanium is avoided for electrochemical applications because it will anodically oxidize in some electrolytes. For applications that require repeated voltage cycling or the application of relatively high (or low) potentials ($> \pm 1.0$ V), titanium is not an ideal choice for electrode material. However, for the proof-of-principle membrane actuation experiments described here, titanium was a cheap, readily available, effective electrode material. Nickel catalyst stripes were patterned in photoresist by contact photolithography (see Figure 4-8, step 2). The stripes were 2 μm wide, in the shape of squares with sides of 10, 25, 50, 100, or 150 μm . Then, 30 nm of nickel catalyst was deposited with an electron beam evaporator (see Figure 4-8, step 3) and excess metal was lifted off in acetone (see Figure 4-8, step 4). Carbon nanofibers were grown in a dc-PECVD vacuum chamber. Wafers were heated to 600 $^{\circ}\text{C}$ and nanofiber synthesis was performed with 188 sccm NH_3 and 70 sccm C_2H_2 at 10 torr and 1.0 A of plasma current

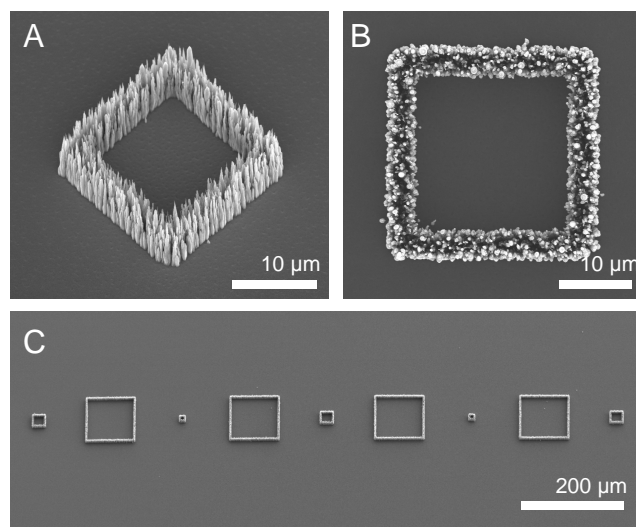


Figure 4-9) Electron micrographs of a 25 μm square VACNF membrane structure taken at **A)** a 30° tilt and **B)** from directly above. **C)** The array of different sized membrane structures, taken from the top.

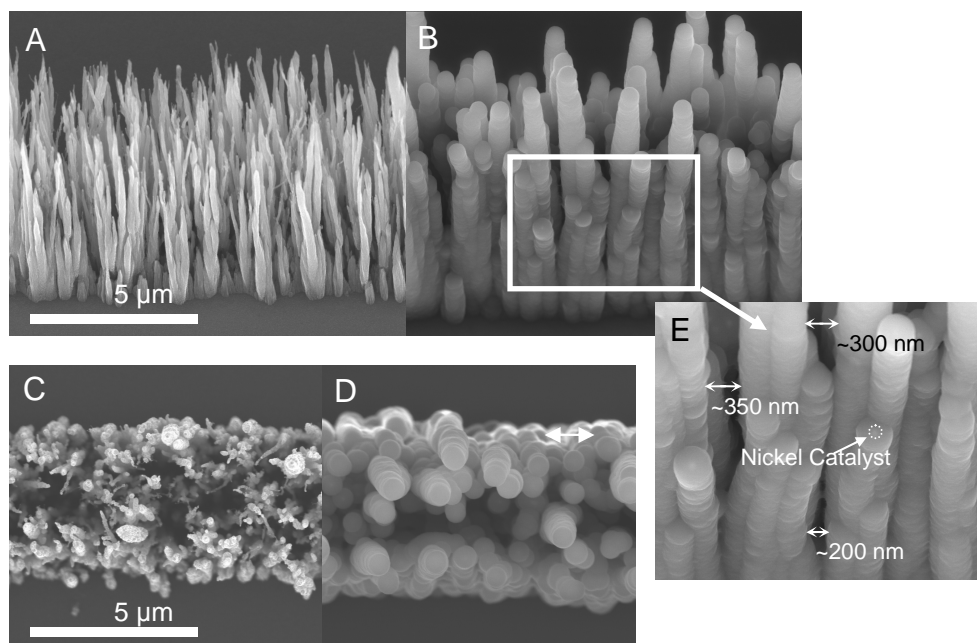


Figure 4-10) Electron micrographs of a membrane structure prior to PPy polymerization (**A, C**) and after (**B, D, E**). Images were taken **A, B, E**) at a 30° tilt and **C, D**) from directly above. Thickness measurements were made relative to the diameter of the nickel catalyst highlighted in **E**.

(see Figure 4-8, step 5). Nanofibers grown on a titanium substrate under these conditions were $\sim 8.5 - 9.5 \mu\text{m}$ tall with nominal diameters of 500 nm at the base and 300 nm at the tip. Scanning electron micrographs of the resulting structures are shown in Figure 4-9.

The wafers with the VACNF membrane structures were cleaved into rectangular chips $\sim 6 \text{ cm}^2$ in area. Copper wires were affixed to the corners of each chip with silver-

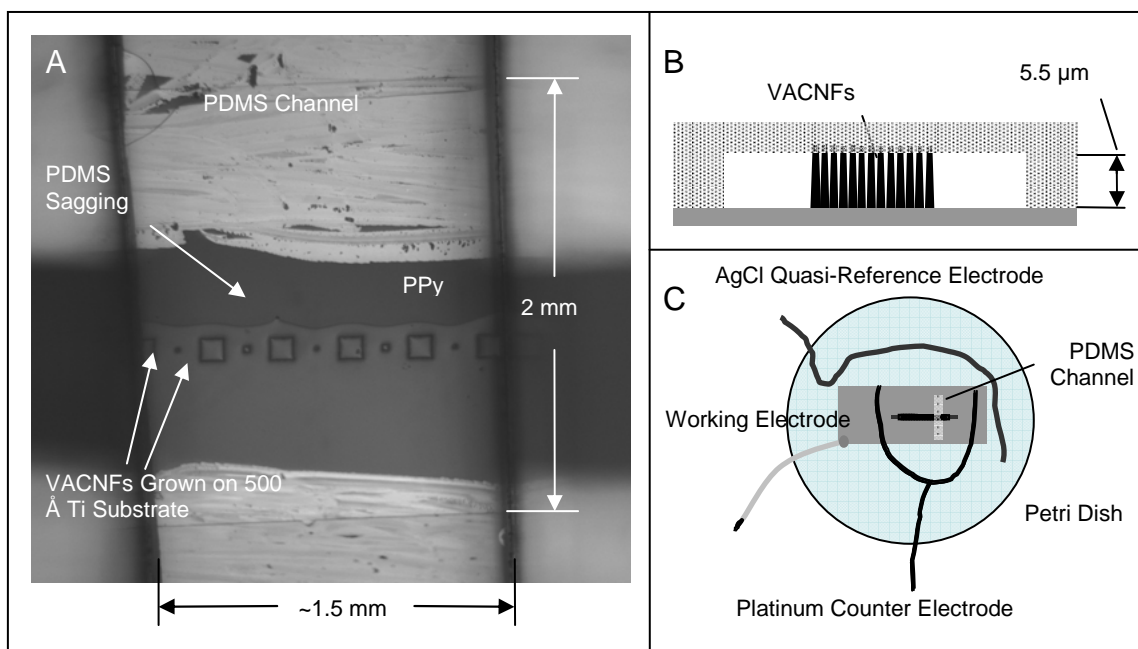


Figure 4-11) A) An optical micrograph of the VACNF membrane structures encapsulated within a PDMS microfluidic channel. Prior to mating, excess PPy was scraped from the substrate. The substrate still coated with PPy is darker colored than the substrate no longer coated with PPy. The channel was 2 mm wide and 1.5 mm long and flow was from left to right. Graphical representations of **B)** the channel interior and **C)** the experimental set up.

loaded epoxy and then were insulated by coating with a non-conductive epoxy. To reduce the current flowing to the working electrode, active electrode area was reduced by painting with finger nail polish. A rectangular shaped area ($\sim 2 \text{ cm}^2$) immediately surrounding the VACNF membrane structures was left unpainted.

Polypyrrole films were deposited on the VACNF membranes (see Figure 4-8, step 6). Pyrrole monomer was prepared as 0.1 M monomer in 0.1 M NaDBS. Polymerization was conducted in a three electrode cell, with a Ag/AgCl reference and a gold counter electrode (equivalent electrically active area to working), at 700 mV for 30 seconds. After deposition, membrane structures were imaged in an electron microscope. It was possible to image the nickel catalyst buried under the PPy by using the upper detector of the SEM at an acceleration voltage of 10.0 kV (see Figure 4-10E). This allowed for taking measurements of the resulting PPy film thicknesses using the catalyst as a reference. The nominal thickness of PPy, polymerized under the described conditions, was $\sim 150 - 200 \text{ nm}$. The interfiber spacings of the VACNFs were reduced from $\sim 600 - 800 \text{ nm}$ to $\sim 250 - 350 \text{ nm}$. Longer deposition times would result in the PPy films on individual nanofibers growing together to close the pores of the membrane. Electron micrographs of the VACNF membranes, before and after polymerization, are shown in Figure 4-10.

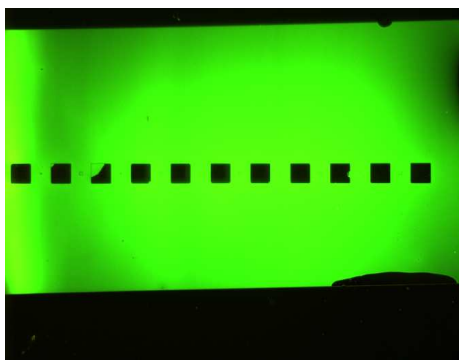


Figure 4-12) Fluorescence micrographs of VACNF membrane structures encapsulated within a PDMS channel. The channel is filled with fluorescein. The VACNF membrane structures fill slowly relative to the channel.

Simple fluidic channels were created from polydimethylsiloxane (PDMS). Molds for the channels, 2 mm wide and 4 cm long, were patterned on silicon wafers by using a photomask and contact photolithography (see Figure 4-8, step 8). Areas of exposed silicon were etched down 5.5 μm by inductively coupled SF_6 -based plasma RIE. Prior to use, the silicon molds were primed with hexamethyldisilazane (HMDS) priming agent to prevent the PDMS from sticking to the substrate during curing. PDMS was mixed at a 10:1 resin to curing agent ratio and poured over the silicon channel mold (see Figure 4-8, step 9). After curing at 60 $^{\circ}\text{C}$ for 90 minutes, channels were cut from the mold with a scalpel to a length of ~ 1.5 mm, long enough to encapsulate 5-7 membrane structures (see Figure 4-11A).

Because the entire chip was bulk addressed, PPy would deposit on the substrate as well as the VACNFs during polymerization. During actuation experiments, the PPy on the substrate, as well as on the nanofibers, would undergo volume changes. The swelling and shrinking of the PPy on the substrate would adversely affect sealing with the PDMS channels. This problem was solved by scraping the PPy from the substrate with a scalpel, except for a thin (~ 1 mm) strip of polymer immediately surrounding the VACNF membrane structures (see Figure 4-8, step 7 and Figure 4-11A). After scraping excess PPy from the substrate, both the substrate and the PDMS channel were placed in an oxygen plasma. Exposure to the plasma enhanced the number of carboxyl groups on the surfaces of both the substrate and the PDMS. When the surfaces were placed in contact after exposure to the plasma, a stronger bond would form. However, the actuation performance of PPy exposed to oxygen plasma for prolonged periods (> 10 s, 100 W, 10 sccm O_2) was noticeably degraded.

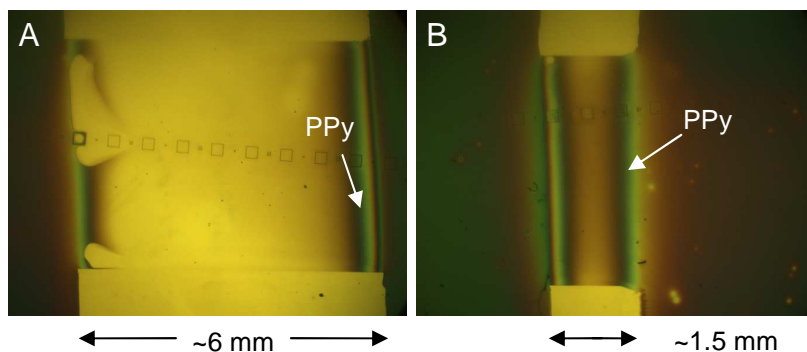


Figure 4-13) Optical micrographs of PPy films synthesized within **A)** a wide and **B)** narrow microfluidic channel.

VACNFs were typically grown to a height of $8.5 - 9.5 \mu\text{m}$, while the channels were molded to a depth of $5.5 \mu\text{m}$. The height discrepancy was intentional so that the tips of the carbon fibers would become embedded within the PDMS lid upon mating. This ensured a good seal between the top of the VACNF membrane and the PDMS lid (see Figure 4-11B). For actuation experiments, the VACNF membrane structures were placed in a Petri dish, along with a platinum wire counter and a AgCl quasi-reference ($+10 \text{ mV}$ vs Ag/AgCl in 0.1 M NaDBS) electrode (see Figure 4-11C). Fluorescently labeled species were suspended in 0.1 M NaDBS solutions. In a typical experiment, 50 nm fluorescently labeled latex beads diluted in NaDBS would fill the Petri dish until the PDMS fluidic channels would wet. Fluorescent species would rapidly diffuse, completely wetting the channel and the VACNF membrane structures within ~ 10 seconds (see Figure 4-12). Voltage would then be potentiostatically applied to shrink and swell the PPy films (-1.0 V to swell and 0.0 V to shrink). Fluorophore transport was observed by fluorescence microscopy.

Very narrow ($\sim 1.5 \text{ mm}$) sections of PDMS channel were used to encapsulate the VACNF membrane structures for actuation experiments. The narrow length allowed for rapid transport of species into and out of the channels without necessitating further fluidic controls. To illustrate this concept, polypyrrole was polymerized on the channel substrate of both a long ($\sim 6 \text{ mm}$) and short ($\sim 1.5 \text{ mm}$) length of microfluidic channel. A monomer solution of 0.1 M pyrrole and 0.1 M NaDBS was prepared. A VACNF membrane structure was placed in a Petri dish in an experimental setup similar to the one outlined above and depicted in Figure 4-11C. Polypyrrole was synthesized by applying a constant potential of 0.70 V for 20 seconds. Optical micrographs of the resulting polymer films can be seen in Figure 4-13. The polymerization reaction was severely limited by

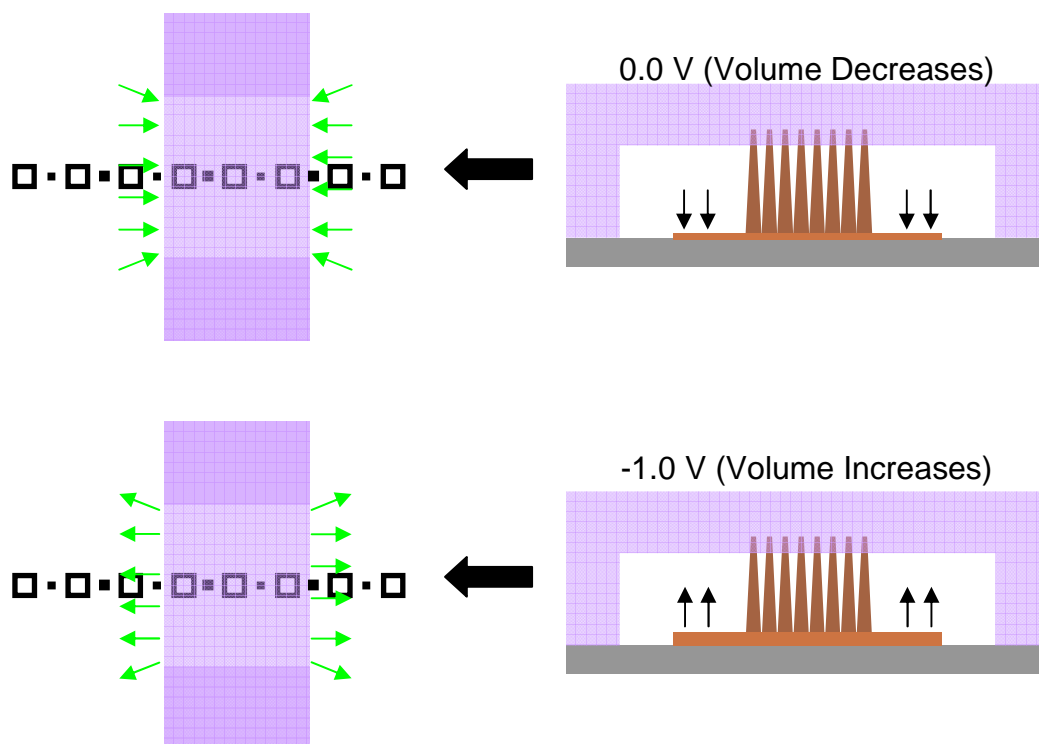


Figure 4-14) Graphical representation of the pumping action introduced by actuation of PPy on the channel substrate. The volume increase of the PPy during actuation pushes fluids out of the channel while the volume decrease allows surrounding fluids to reenter the channel.

diffusion within the longer microfluidic channel, as evidenced by the thinner layer of deposited PPy (see Figure 4-13A). The polymer film was much thicker in the shorter channel because the monomer consumed by the polymerization reaction within the channel was more rapidly replenished by diffusion (see Figure 4-13B). The availability of ionic species is also important in polypyrrole actuation. For longer lengths of microfluidic channels, the diffusion limited transport of ions into the channels would inhibit polymer actuation. For these reasons, shorter lengths of microfluidic channels (~1.5 mm) were preferred for actuation experiments.

The volume change of the PPy on the channel substrate introduced a pumping action to the microfluidic channel (see Figure 4-14). When swollen, the increased volume of the PPy would displace fluids in the channel, pushing the fluids out along with fluorescent species. Upon shrinking, surrounding fluids and fluorescent species would rush back into the channel. The pumping action alleviated the need to introduce other flow control mechanisms.

Fluorescent micrographs of an actuation experiment involving 50 nm fluorescently labeled latex beads can be seen in Figure 4-15. In Figure 4-15A, the PPy

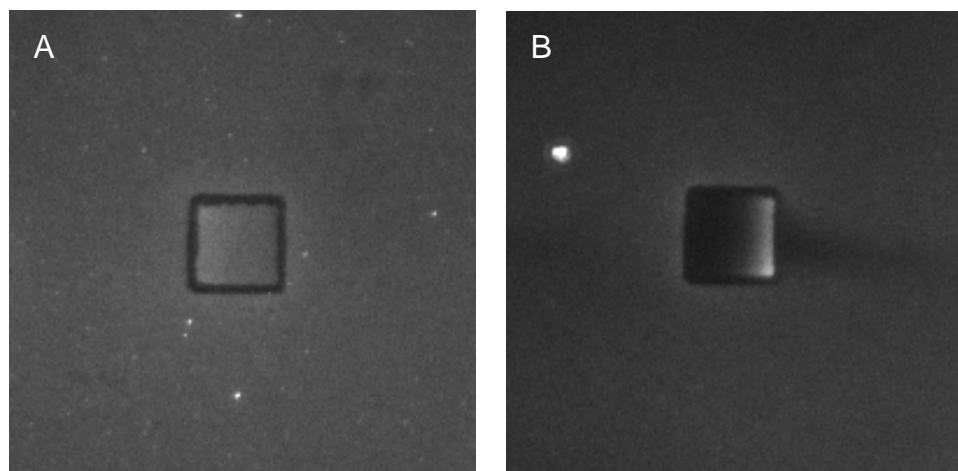


Figure 4-15) Fluorescence micrographs of a VACNF membrane structure encapsulated within a PDMS microfluidic channel. 50 nm fluorescently labeled latex beads are **A)** flowing freely through the membrane structure because the PPy film is not actuated. **B)** Upon actuation, flow of latex beads through the VACNF membrane structure becomes restricted.

film on the VACNF membrane structure was not actuated. The membrane pores were thus “open” and latex beads flowed freely through the membrane walls. When a reducing potential (-1.0 V) was applied to the membrane structure, the PPy coatings on the VACNFs and on the channel substrate increased in volume. The interfiber spacings of the VACNFs were reduced by the swollen PPy films and flow through the pores of the membrane was “restricted” (see Figure 4-15B). In this state, flow was primarily around the membrane structures, rather than through them. However, fluid flow through the membrane did continue as evidenced by the accumulation of beads on the membrane surface. The membrane is not completely size selective, as some of the trapped beads leak over time.

The membranes were leaky because of the stochastic placement of the VACNFs within the membrane walls. Prior to growth, the stripes of catalyst metal were subjected to an ammonia plasma etch. During this etch, the catalyst film broke up into catalyst nanoparticles several hundred nanometers in diameter at spacings several hundred nanometers apart. While the catalyst stripes were patterned and the VACNFs were grown using microscale techniques, the resulting structures possessed nanoscale functionality. However, the spatial positioning of the resultant carbon nanofibers was dependent on the stochastic dispersion of catalyst nanoparticles. The interfiber spacings of nanofibers would vary significantly, with regions of the VACNF membranes with relatively high permeability and regions with relatively low permeability.

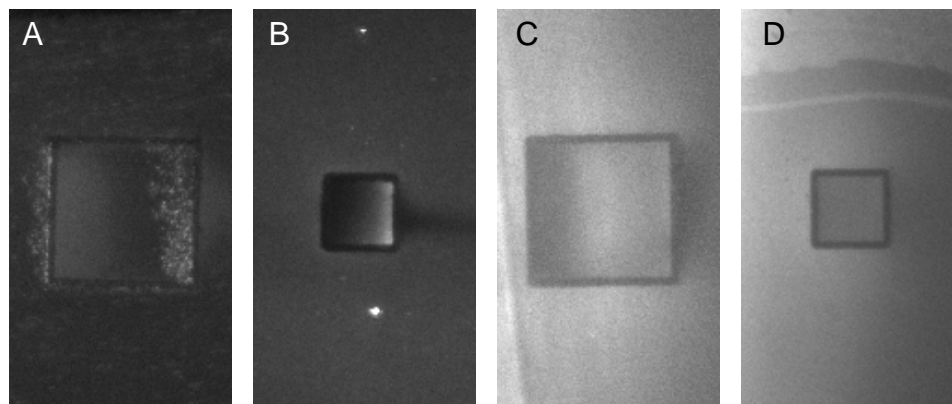


Figure 4-16) Fluorescence micrographs of **A)** 200 nm and **B)** 50 nm fluorescently labeled latex beads, **C)** fluorescently labeled streptavidin, and **D)** fluorescein isothiocyanate flowing through a VACNF membrane structure in the “restricted” flow state. The VACNF structures **A, C)** are 150 μm or **B, D)** 50 μm squares.

Despite these limitations, the transport of a wide range of species was modulated by PPy actuation. Changes in permeability of the VACNF membranes were observed for 200 nm and 50 nm fluorescently labeled latex beads, fluorescently labeled streptavidin (F-SA), and fluorescein isothiocyanate (FITC). Fluorescence micrographs showing the flow of each of these species through VACNF membrane structures can be seen in Figure 4-16. The micrographs in Figures 4-16A and 4-16B were taken ~10 seconds after actuation was initiated. In these two experiments, the fluorescent species are relatively large (200 and 50 nm latex beads). When the micrographs were captured, freely flowing beads within the microfluidic channel were largely evacuated while a higher concentration of fluorescent species remained within the VACNF membrane structures. The micrographs in Figures 4-16C and 4-16D were taken ~5 seconds after actuation of PPy. The particles in these experiments were relatively small (F-SA and FITC), so transport through the VACNF membrane structures was more rapid. The degree of restriction introduced by actuation of PPy on the VACNFs was less than the degree of restriction for the larger particles depicted in Figures 4-16A and 4-16B. As a result, the micrographs had to be captured more quickly (~5 seconds rather than ~10 seconds) to visualize the flow restriction. A high concentration of fluorescent species still remained within the microfluidic channels, as reflected in the brighter background fluorescence of the images. VACNF membrane structures could be actuated ~5 times on average before failing. The most common source of failure was from fluidic leaks between the PDMS channel and the underlying substrate. The bond between the PDMS and the titanium substrate was relatively weak and would break from the pressures of fluidic flow.

4.3 *Conclusions*

Actuable membranes were fabricated by depositing polypyrrole on the sidewalls of vertically aligned carbon nanofibers. The VACNFs were patterned and grown in the shape of hollow square cells, with relatively thin (2 μm) walls. Polypyrrole was then electrochemically deposited on the nanofibers to reduce their diameters and, thus, their interfiber spacings. The interfiber spacings formed the pores of the VACNF membranes. The polymer coatings were then actuated (increasing and decreasing in volume) by externally applied electrical stimuli. This modulated the interfiber spacings and opened and restricted the pores of the VACNF membranes. The ability to alter the permeability of the membranes was then demonstrated by flowing fluorescently labeled species through. When actuated, the membranes were shown to restrict the flow of the particles based on their size. When not actuated, species were shown to freely flow through the membranes.

However, the VACNF membranes did demonstrate two limitations. Because of the stochastic placement of nanofibers within the membrane walls, there were areas that would leak. This phenomenon might be alleviated by defining catalyst sites using nanoscale lithographic techniques, such as electron beam patterning. Accurate placement of individual membrane components would allow for better control of membrane permeability and actuation properties. The devices would also fail relatively quickly (after ~ 5 actuations) because of the primitive design of the fluidic system. One solution would be to incorporate all of the electrodes within the microfluidic channel. This would allow for more robust microfluidic systems to be designed with better sealing and flow control. Despite the relative fragility of the devices, VACNF membrane structures showed promising results as membranes that modulate permeability by external electrical control.

Chapter 5

Capture of Particles within Membrane Structures

Impeding the flow of particles as small as biological macromolecules (DNA, proteins) requires membranes with extremely precise, well defined pores. In this chapter, synthetic membranes were constructed from metal-coated, anisotropically etched silicon posts modified with polypyrrole. Better definition of membrane pores was sought by patterning individual membrane components with electron beam lithography in precise patterns at well defined spacings. Silicon posts were then etched to heights, widths, and aspect ratios similar to previously described VACNFs. The posts were coated with a thin layer of metal to provide electrical connectivity. Polypyrrole was electropolymerized on the surfaces of the metal coated silicon posts to modify their diameters and to further reduce membrane pore sizes. Membranes constructed from the silicon posts were fabricated within intricate microfluidic devices. The permeability of the membranes was controlled using external electrical controls to shrink and swell the polypyrrole coating. The ability to impede the flow of particles as small as proteins was demonstrated.

5.1 *Limitations of VACNFs as Membrane Components*

Thus far, catalyst metals for the growth of VACNFs have been patterned using relatively simple microscale fabrication techniques (contact lithography). Patterns have been imprinted in photoresists by exposure to UV illumination through photomasks. Although the resolution of contact lithography can be enhanced to allow the definition of extremely small features (< 50 nm), typically the lower limits are 1 to 2 μm . However, patterns are transferred extremely quickly (~5 minutes to completely process a wafer) using readily available equipment. In addition, the resulting stochastic forests of carbon nanofibers feature emergent nanoscale properties. Individual nanofibers within the VACNF forests are, on average, several hundred nanometers in diameter spaced several hundred nanometers apart. The pores of the membranes, defined by the

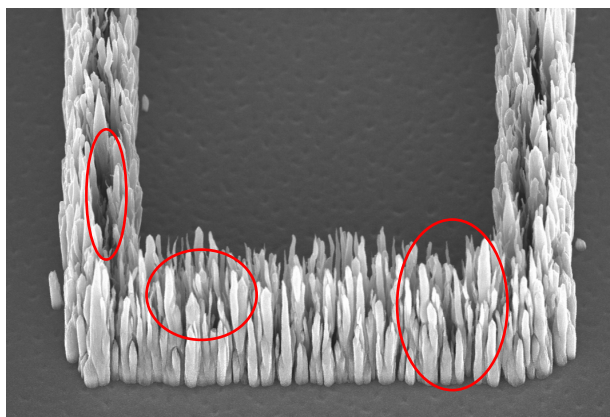


Figure 5-1) An electron micrograph of a membrane structure constructed from stochastic forests of VACNFs. Areas of the forest with significantly lower densities of nanofibers are circled in red. The permeability of the membrane in these areas is higher.

interfiber spacings between carbon nanofibers, are on the order of 600-800 nm. The ability to synthesize membranes with nanoscale pores using simple microscale patterning techniques is enabled by PECVD growth of vertically aligned carbon nanofibers.

While the stochastic growth of VACNFs from patterned metal catalysts has the described advantages, it also has disadvantages. If the metal catalyst is patterned as a continuous thin film (>500 nm in at least one dimension), then the film has to be broken up into nanoparticles prior to growth. An ammonia plasma etch at 700 °C is used to break the films up into nanoparticles of a wide range of sizes at a wide range of spacings. The spatial orientation and diameter of resulting VACNFs is determined by the placement and size of the resulting catalyst nanoparticles. Variability in the interfiber spacings and nanoparticle sizes results in variability in membrane permeability (see Figure 5-1). Regions of VACNF membranes can have relatively higher permeability while other regions can have relatively lower permeability. As a result, the VACNF membranes are susceptible to leaking at certain discrete locations.

One solution to this problem is to define individual catalyst sites of predetermined sizes at specific locations using an electron beam lithography system. This form of lithography uses a beam of electrons to generate patterns in a photosensitive polymer. Patterns are written by rastering the electron beam over a polymer-coated surface. Electrons change the solubility of polymer exposed to the beam. The exposed polymer is then dissolved in a solute that does not affect the unexposed polymer. Features can be written as small as 10 nm using electron beam lithography because the technique is not affected by the diffraction limit of light [193]. However, electron beam lithography is much

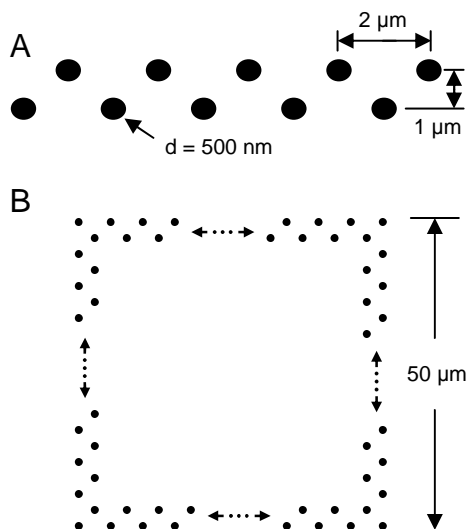


Figure 5-2) Graphical representations of the electron beam patterned catalyst sites. **A)** Catalyst sites were 500 nm diameter dots **B)** patterned as a four-sided box, 50 μm on each side.

slower than a parallel patterning technique such as contact photolithography. A single wafer can take hours to fully process.

By defining the spatial locations of catalyst nanoparticles using electron beam lithography, it was possible to define the interfiber spacings of resulting VACNF membranes with nanometer precision. Catalyst sites were defined as 500 nm diameter dots, patterned in double staggered rows (see Figure 5-2A). The dots were spaced $2\ \mu\text{m}$ apart and the staggered rows were spaced $1\ \mu\text{m}$ apart. The double staggered rows formed the walls of a four-sided box, 50 μm on each side. A graphical description of the catalyst pattern is presented in Figure 5-2. To grow VACNFs, silicon wafers were first spin coated with polymethyl methacrylate (PMMA), a polymer sensitive to electron beam irradiation. Wafers were then loaded into a JEOL JBX-9300 electron beam lithography system and catalyst dots were patterned in the PMMA. Exposure to the electron beam created chain scissions within the PMMA chains, allowing for selective removal of the exposed polymer by chemical developer. After development, wafers were cleaned of residual photoresist by oxygen plasma. Then, catalyst metals were deposited using an electron beam evaporator: 100 Å Ti and 300 Å Ni. Excess metal was lifted off in an acetone solution. Carbon nanofibers were synthesized in a dc-PECVD process. Wafers were placed on a substrate heater within a vacuum chamber. The wafers were heated to

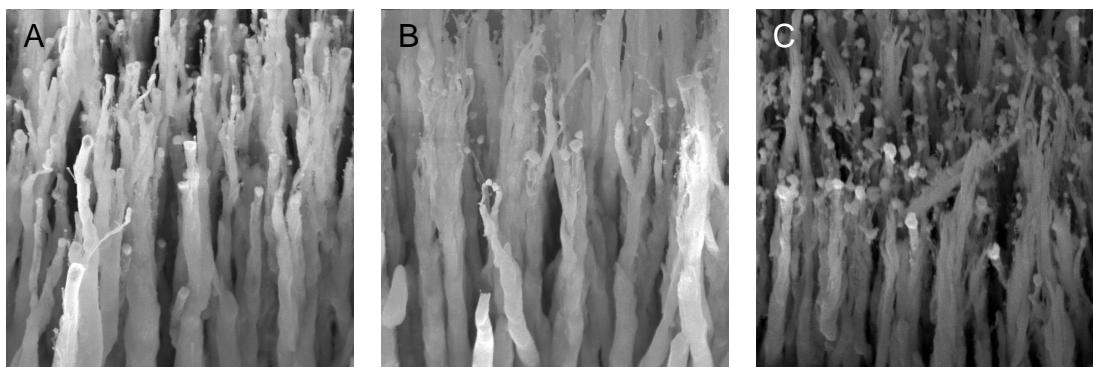


Figure 5-3) Electron micrographs of carbon nanofibers grown in three separate, consecutive processes. Plasma power, substrate temperature, gas flow rates, and gas ratios were the same for all three growths.

700 °C and fibers were grown with 185 sccm NH_3 and 115 sccm C_2H_2 at 400 mA plasma current and at 2.5 torr chamber pressure.

Carbon nanofiber synthesis is typically directed by easily adjustable parameters such as the ratio of carbon to etchant gases, gas flow rates, chamber pressures, substrate temperatures, and plasma powers. However, other variables that are more difficult to control also have a considerable effect on VACNF growth. These include the condition of the inner surface of the vacuum chamber, the position of the plasma in relation to the growth substrate, the dispersion of heat across the substrate, local interactions between carbon atoms and interactions between the carbon and catalyst metals, and any number of other poorly understood or undiscovered factors. Because carbon nanofiber synthesis is a directed self-assembly process, many variables affecting resultant nanofiber geometries are currently beyond control. While the height, aspect ratio, and spatial orientation of carbon nanofibers can be generally specified, a degree of stochasticity in the process still remains. To illustrate, a series of three consecutive VACNF growths were conducted on three separate wafers using the same controllable growth parameters. Electron micrographs of the resulting nanofibers can be seen in Figure 5-3. The nanofibers appear to become progressively more etched, particularly at the tips, with each subsequent growth. The carbon underneath the catalyst nanoparticles at the tips of the VACNFs in Figure 5-3C is almost completely undercut, while the effect is less pronounced in the nanofibers depicted in Figure 5-3A. During synthesis, gas molecules deposit on the inner surface of the PECVD vacuum chamber. One source of the phenomenon depicted in Figure 5-3 could be carbon, and/or other contaminants present on the chamber walls from previous processes, coming free from the chamber walls to affect the carbon to etchant gas ratio during VACNF synthesis.

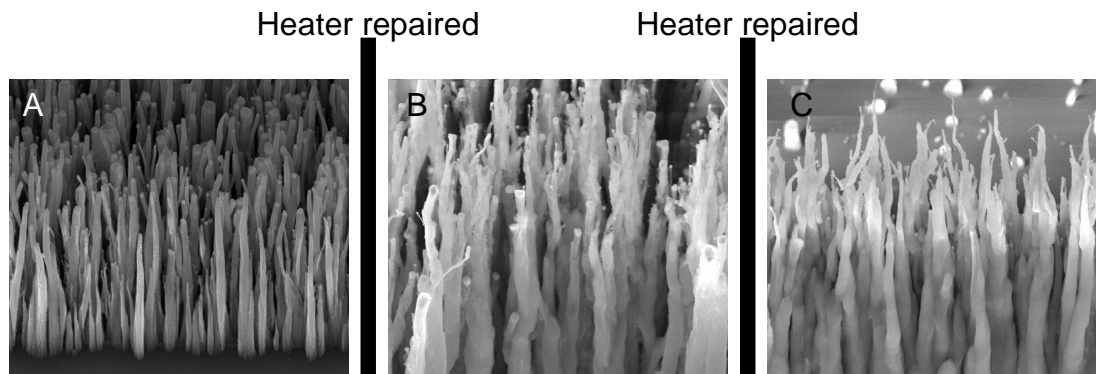


Figure 5-4) Electron micrographs of carbon nanofibers grown in three separate, consecutive processes. Plasma power, substrate temperature, gas flow rates, and gas ratios were the same for all three growths. The substrate heater malfunctioned and had to be repaired between the growth of fibers depicted in **A)** and **B)** and between the growth of fibers depicted in **B)** and **C)**.

On one occasion, the substrate heater in the PECVD chamber malfunctioned immediately after a growth process was completed. After the heater was repaired, VACNFs grown under similar process conditions had significantly different geometries than the VACNFs grown prior to the malfunction. VACNFs grown before and after heater repairs are shown in Figures 5-4A and 5-4B. Immediately after the growth depicted in Figure 5-4B, the heater malfunctioned again. VACNFs synthesized after the substrate heater was repaired a second time are shown in Figure 5-4C. For each of the depicted growths, the substrate heater was functioning properly and heating the substrate to the appropriate temperature. Differences could be due to any number of other factors. One possibility is that the substrate heater was contaminated during repair.

For some growths, there was a significant difference in the structure of VACNFs grown at different locations on the wafer. One of the main sources of this variability is likely due to variations in substrate temperatures. There could be more resistive areas on the substrate heater due to contaminants or there might be poor contact between the growth substrate and the heater. To demonstrate the influence of substrate temperatures on VACNF synthesis, a 4" diameter wafer with patterned metal catalyst was placed on a 2" diameter substrate heater. VACNF synthesis was conducted and the resultant nanofibers are shown in Figure 5-5. Nanofibers grown near the center of the 2" substrate heater have relatively uniform geometries. Changes in the geometries of the VACNFs become progressively more dramatic further from the center of the heater, where temperatures are progressively cooler.

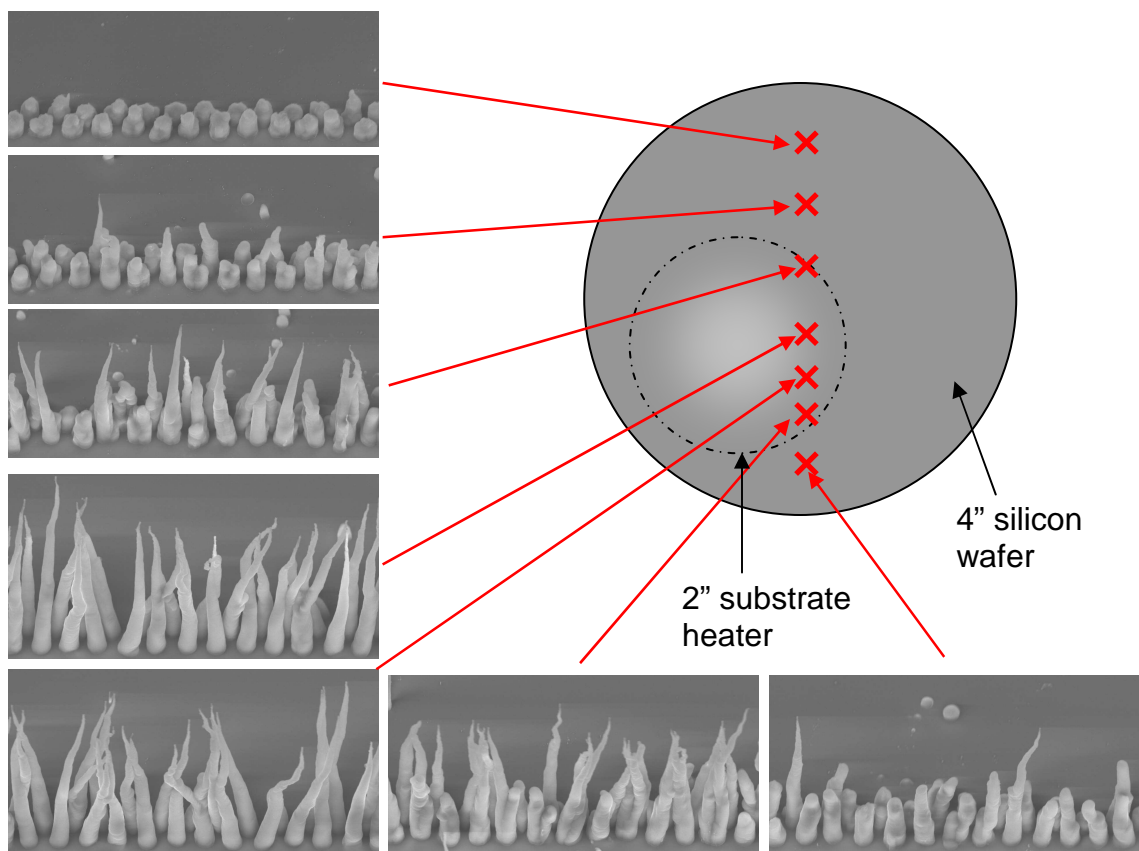


Figure 5-5) In the upper right, a graphical depiction of a 4" silicon wafer on a 2" substrate heater. Red Xs denote the locations of VACNFs grown on the silicon substrate. Corresponding electron micrographs of the VACNFs are shown.

The high number of uncontrollable variables affecting carbon nanofiber synthesis complicates the use of VACNFs in some applications. For membranes constructed from stochastic forests of VACNFs, a great deal of variability in nanofiber geometry can be tolerated. The important dimensions are interfiber spacings and nanofiber heights. The occasional defect can be compensated for by the high density (low interfiber spacings) of VACNF membrane components within the membrane wall. Nanofiber forests depicted in Figures 5-3 and 5-4 would function adequately in this capacity. However, there is a significantly lower tolerance for variations in membrane component geometries when the components are patterned in specific spatial locations at larger interfiber spacings. If, for instance, a nanofiber does not grow from one of the catalyst sites depicted in Figure 5-2A, then there is a space in the membrane wall that cannot be compensated for. If a nanofiber is shorter than the others, or is not vertically aligned, or if there is more than one nanofiber at a site, then the efficacy of the membrane is compromised.

Because so many uncontrollable variables affect the self-assembly of carbon nanofibers, there is always a degree of stochasticity in the resultant geometries of the

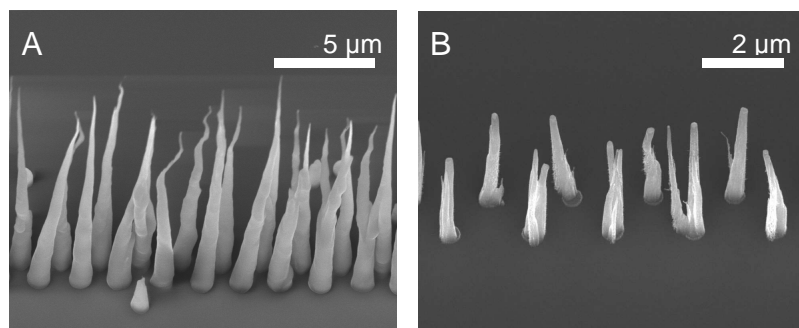


Figure 5-6) Electron micrographs of VACNFs grown from catalyst sites defined by electron beam lithography.

nanofibers. This variability in geometries is illustrated in Figure 5-6. VACNFs were patterned by electron beam lithography in the pattern depicted in Figure 5-2A and were grown in a PECVD. There was a deviation of $\sim \pm 2 \mu\text{m}$ from the average height of $10 \mu\text{m}$ for the VACNFs depicted in Figure 5-6A. In addition, most of the fibers were not vertically aligned, particularly at the tips. These carbon nanofibers form a membrane with poorly defined pores. In Figure 5-6B, multiple nanofibers grew from individual catalyst sites. As a result, the base diameters of the fibers varied from 300 nm to $1 \mu\text{m}$. The permeability of membranes formed from these VACNFs would vary accordingly.

In summary, the construction of membranes with nanoscale pores using microscale techniques is enabled by the deterministic growth of stochastic forests of vertically aligned carbon nanofibers. However, this same enabling process introduces limitations to the application of VACNFs within more precisely defined membranes. The high number of uncontrollable variables that affect growth lead to an inherent amount of stochasticity in resultant carbon nanofiber geometries. The use of VACNFs is impractical for applications requiring membranes with components of relatively uniform geometries at precisely defined interfiber spacings.

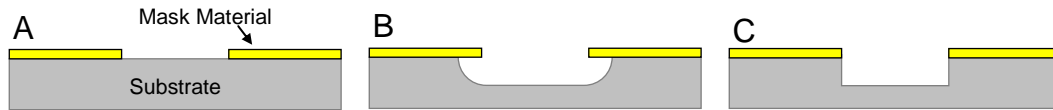


Figure 5-7) Graphical representation of **A)** a substrate partially protected by a masking material prior to etching. **B)** After an isotropic etch, the sidewalls are rounded. **C)** An anisotropic etch results in vertical sidewalls.

5.2 *Anisotropic Etching*

Because of the described limitations of VACNFs for this application, an alternative vertically aligned membrane component was used. Silicon posts, with similar aspect ratios and heights to the previously described VACNFs, were anisotropically etched from a silicon substrate using a well established deep reactive ion etch process [194-198]. Etching is a microfabrication process in which layers are chemically removed from the surface of a wafer [193]. Part of the wafer is protected from the etch using a “masking” material that is resistant to the etch process (see Figure 5-7A). Some common mask materials include photosensitive polymers, oxides, and metals. The mask material typically etches at a much slower rate than the unprotected substrate and the ratio of these etch rates is referred to as the selectivity of the etchant. Many etchants are poorly selective and will erode the substrate equally in all directions. As the etch proceeds, the mask material is undercut and the sidewalls become more rounded (see Figure 5-7B). Etches of this type are referred to as isotropic etches. By protecting or passivating the sidewalls of etch features from subsequent etching or by preferentially etching in one direction, it is possible to perform deep etches with nearly vertical sidewalls ($\sim 88^\circ - 92^\circ$, see Figure 5-7C). These etches are called anisotropic etches.

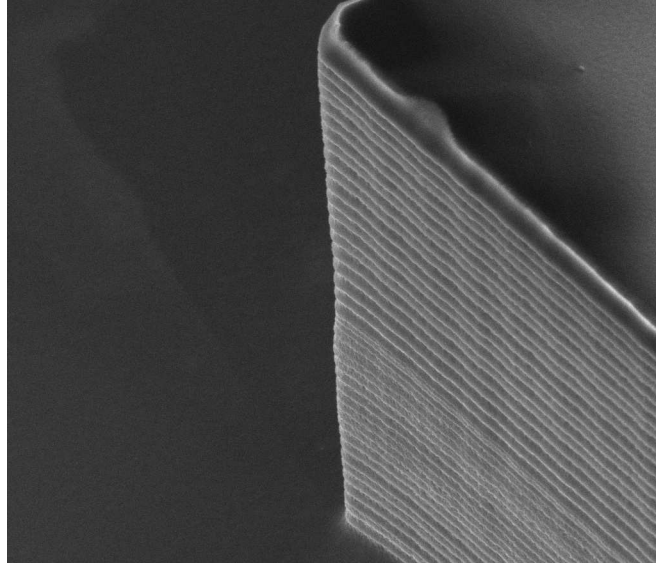


Figure 5-8) An electron micrograph of the step planes in the sidewalls of a Bosch etched feature. Image courtesy of Scott Retterer.

Etchants are either liquid (“wet”) or plasma (“dry”) based. Most commonly used wet etchants produce isotropic profiles because they have a tendency to etch materials at equal rates in all directions. A notable exception is buffered oxide etchant, which etches downwards more quickly than it etches laterally. Anisotropic wet etching is also possible when the etchants preferentially etch along certain crystal planes of the substrate or when regions of the substrate are doped with “stop materials” resistant to the etchant [199]. Some commonly used wet etchants include hydrofluoric acid, hydrogen peroxide, hydrochloric acid, and photoresist developer. Anisotropic etches are almost exclusively dry and are typically conducted within reactive ion etch (RIE) systems. In an RIE, chlorinated or fluorinated precursors dissociate and ionize in low pressure plasmas to form neutrals, electrons, photons, radicals, and positive and negative ions [196]. Reactive ions diffuse to the substrate (almost entirely from the normal direction) and adsorb to it. A reaction between the adsorbed species and surface molecules occurs to form volatile products that desorb into the gas phase. Spontaneous etching also takes place between long-lived radicals and the surface molecules on the sidewalls of etched features [198]. Because of these secondary reactions involving long-lived radicals, RIE processes are typically isotropic. Anisotropic RIE processes require sidewall passivation schemes to inhibit spontaneous etching. Highly selective and highly anisotropic RIE processes are referred to as deep reactive ion etches (DRIE). There are two types of DRIE processes, cryogenic and Bosch, distinguished by their sidewall passivation schemes.

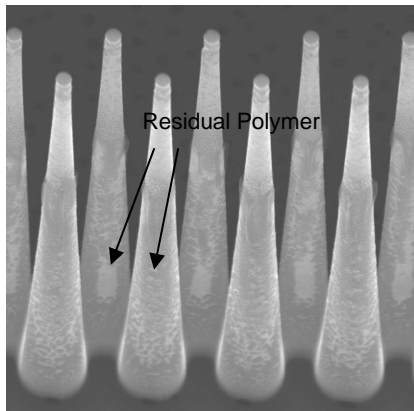


Figure 5-9) An electron micrograph of cryogenically etched silicon posts. The polymer passivation layer can be seen on the sidewalls of the posts.

The Bosch process consists of two repeated steps. The first step is a standard isotropic RIE plasma etch. In the second step, a chemically inert passivation layer is deposited on the sidewalls and bottoms of the etch features, to protect them from secondary reactions initiated by long-lived radicals. When the first step is repeated, ions bombard the bottom of the etch feature while leaving the sidewalls virtually undisturbed. The passivation layer is sputtered off, leaving the bottom exposed to further etching. Steps one and two are sequentially repeated many times until the features are etched to a desired depth. Because of the large number of sequential isotropic etches, the sidewalls of etch features typically feature step planes (see Figure 5-8). Smoother sidewalls can be produced by shortening the cycle time between steps, but Bosch etches are usually used to etch larger ($> 1 \mu\text{m}$) features because of this phenomenon.

The sidewall protection mechanism in cryogenic deep reactive ion etches is a combination of the deposition of a passivation layer and the reduction of secondary reaction rates [194]. The substrate is cooled to low (-110°C for Si etching) temperatures, to reduce the reaction rate between long-lived radicals and surface molecules [198]. This protects the sidewalls from spontaneous etching while only slightly affecting ion etching at the bottom of the etch feature [200]. An inhibitor layer is also deposited in parallel with the etch process. For fluorine-based plasmas, oxygen is added to the plasma to enable the formation of a silicon oxyfluoride (SiO_xF_y) inhibitor layer (see Figure 5-9). Cations from the fluorine plasma etch the passivation layer as they strike the surface. Because ion bombardment is almost entirely normal to the substrate, the blocking layer on the sidewalls is largely unaffected while the layer at the bottom of the etch feature is continuously removed. Deposition of the passivation layer, its removal from the bottom

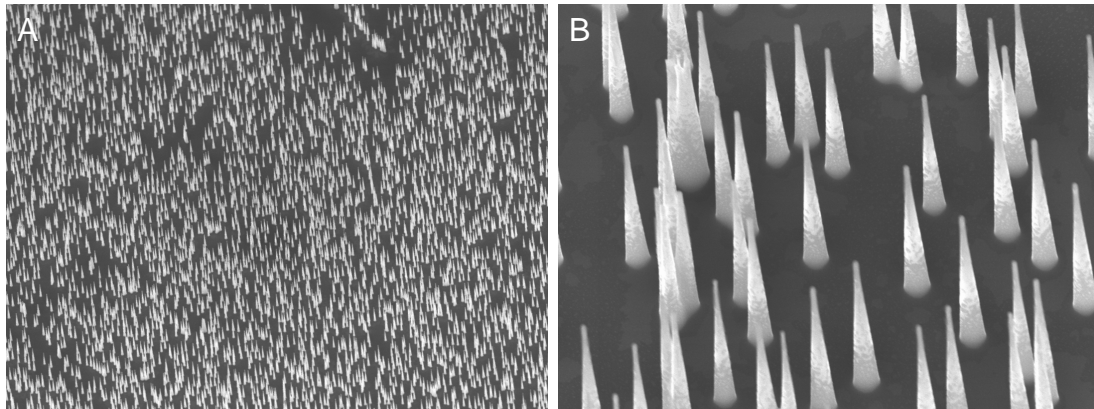


Figure 5-10) Electron micrographs of black silicon, viewed at **A)** x 1k and at **B)** x 10k magnification.

of the etch feature, and etching of the silicon surface occur simultaneously. As a result, the sidewalls of etch features are much smoother than the sidewalls resulting from Bosch processing. Cryogenic DRIE processes are preferred for etching very small features ($< 1 \mu\text{m}$).

Mask materials are patterned using conventional micro- and nano- scale lithography techniques. Two commonly used mask materials in cryogenic processes are chromium and photoresist. Chromium is preferred over other metals because it can be easily removed in highly selective wet etches, is cheap and readily available, and is unreactive in fluorine-based plasmas. At low ($< -90 \text{ }^{\circ}\text{C}$) temperatures, photoresist is nearly as unreactive as chromium, with erosion rates on the order of $\sim 2 - 10 \text{ nm/min}$ [194]. At higher temperatures, polymer species from the photoresist will deposit on etch features and contribute to the passivation layer. The erosion rate of the photoresist mask increases (up to 100 nm/min at $0 \text{ }^{\circ}\text{C}$) and the oxygen content of the plasma has to be reduced accordingly. Photoresist also has a tendency to crack at cryogenic etch temperatures ($-110 \text{ }^{\circ}\text{C}$) because the polymer shrinks as it is cooled.

In cryogenic DRIE, the simultaneous deposition and etch processes are in delicate balance. To complicate matters, the balance can be affected by external factors such as the material composition of the mask and contaminants within the plasma chamber. As a result, frequent optimization of process conditions is necessary, requiring many test runs (> 5 test runs). A method was developed to speed the optimization of silicon cryogenic etch processes in fluorine-based plasmas, called the Black Silicon Method (BSM) [195]. This method is based on the fact that silicon turns black when process conditions are nearly optimal. When a balance is achieved between the fluorine radicals that etch the silicon and the oxygen radicals that passivate it, the resulting etch

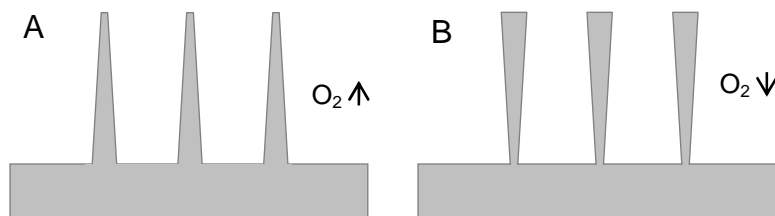


Figure 5-11) Graphical representation of silicon posts featuring sidewalls with **A)** positive and **B)** negative taper. The taper of the sidewalls is controlled by adjusting the oxygen content of the plasma.

profile is nearly vertical. The surface of a silicon wafer is always contaminated with a certain amount of particulates such as native oxides, dust, and organic materials. These contaminants act as nanoscale masks, protecting the underlying silicon. When etch conditions produce a nearly vertical profile, spikes appear with the contaminants at the tips (see Figure 5-10). The underlying silicon body is coated with a thin passivating SiO_xF_y layer. As the spikes become taller at higher etch times, their heights eventually exceed the wavelength of incoming light. This light is refracted by the spikes and becomes trapped, making the silicon wafer appear to be black [195]. The process conditions that produce black silicon are a good starting point for developing anisotropic etch recipes. Further adjustments are typically necessary when mask materials are used to define etch features, as the mask materials alter the etch. Small adjustments to process parameters are usually made by changing the oxygen content of the plasma. Altering the oxygen content changes the taper of the sidewalls of etch features. An increased oxygen content results in a more positive taper (see Figure 5-11A) and a decreased oxygen content results in a more negative taper (see Figure 5-11B) to the sidewalls. Other process parameters that can be adjusted to affect the etch process include the plasma power, substrate temperature, fluorine content, and chamber pressure.

To summarize, silicon etches at cryogenic temperatures in fluorine-based plasmas are highly selective and highly anisotropic. By patterning 500 nm chromium dots with an electron beam lithography system and adjusting process parameters, it is possible to etch silicon posts with diameters, heights, and aspect ratios similar to the previously described vertically aligned carbon nanofibers. There is little to no variation in the geometry and spacing of features etched from silicon. This is a significant advantage in constructing membranes with well defined pores.

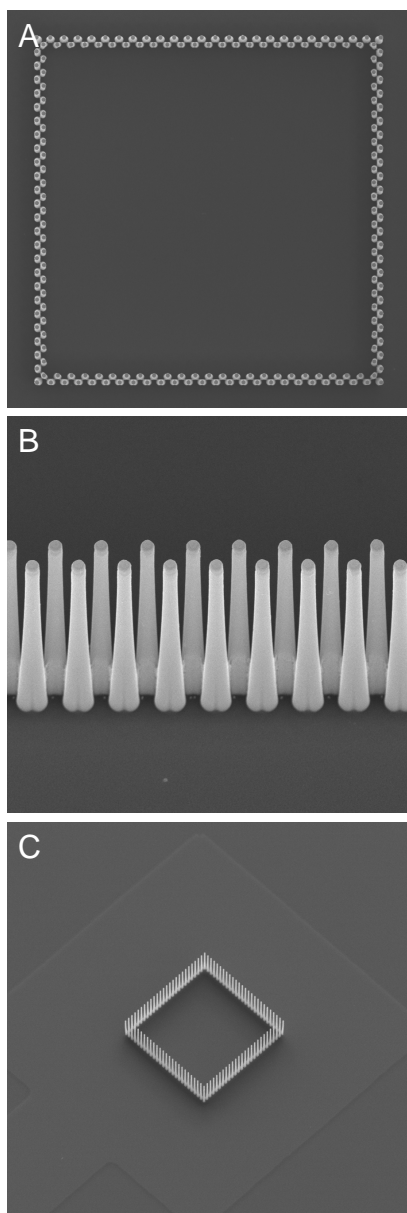


Figure 5-12) Electron micrographs of a membrane structure viewed from **A)** above and **B, C)** at a 30° angle.

5.3 *Capture of Particles within Membrane Structures*

Synthetic membranes with well defined pores were constructed from metal-coated, anisotropically etched silicon posts modified with polypyrrole. To etch silicon posts, silicon wafers were first spin coated with PMMA. Dots, 500 nm in diameter, were patterned in the PMMA by electron beam lithography using the catalyst dot pattern depicted in Figure 5-2. Polymer was selectively removed in chemical developer and then

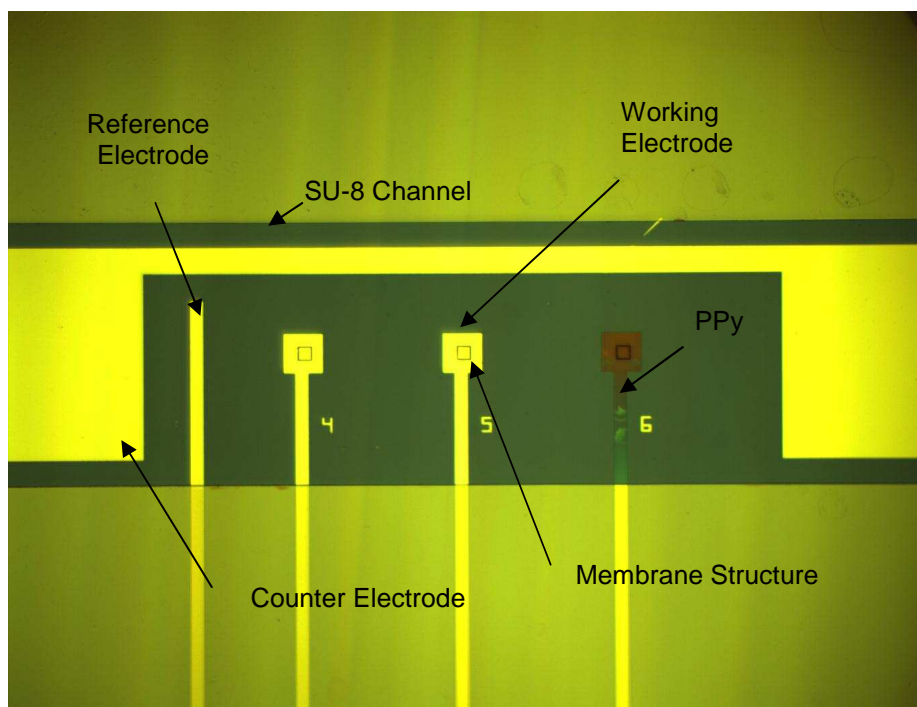


Figure 5-13) Optical micrographs of the reference, working, and counter electrodes viewed at 5x magnification. The electrodes were patterned by contact lithography so that the membrane structures would be at the center of the working electrodes.

the wafers were cleaned in an oxygen plasma. Chromium (150 Å) was deposited using an electron beam evaporator, to act as a masking material for subsequent etch processes. Excess metals were lifted off in an acetone solution. Silicon posts were etched using a cryogenic deep reactive ion etch process. Briefly, wafers were loaded in an RIE and were cryogenically cooled to -110 °C. 13 sccm of O₂ and 80 sccm of SF₆ were maintained at 10 torr before a 1250 W RF plasma was struck. Residual silicon oxyfluoride was removed in a high powered (400 W) oxygen plasma. There was some variability in the geometries of the posts between wafers because of subtle differences between the etch process conditions. Depending on the wafer, silicon posts had base widths between 870 to 1370 nm, tip widths between 390 and 560 nm, and heights between 11.7 and 12.5 μm. However, the silicon posts etched on each wafer were uniform in geometry. Deviations from the average silicon post dimensions were within 1.5% for base widths, within 3% for tip widths, and within 0.25% for heights. Electron micrographs of resulting silicon posts can be seen in Figure 5-12.

Next, electrodes and a microfluidic manifold were fabricated around the membrane structures. Electrodes were integrated within a microfluidic channel to direct the actuation of PPy while the microfluidic manifold was designed to regulate fluid flow

through the system. To fabricate the electrodes, wafers with the etched membrane structures were coated with a passivating layer of silicon dioxide in a PECVD process. The wafers were loaded into a vacuum chamber and were heated to 350 °C. SiH_4/Ar (85 sccm) and N_2O (157 sccm) gas flows were maintained at 1 torr before a 20 W RF plasma was struck. Silicon dioxide layers were deposited to a 50 nm thickness, increasing the diameters of the silicon posts by 100 nm. The oxide layer was deposited to prevent current flow between electrodes. Electrode metals were then deposited on the substrate. Wafers were first spin coated with a positive tone photoresist. After soft baking, metal electrodes were patterned in the polymer by exposure to UV illumination through a photomask. The pattern was developed and residual photoresist was cleaned from the substrate in an oxygen plasma. Then, electrode metals (100 Å Ti adhesion layer, 500 Å Au conductive layer) were deposited by electron beam evaporation. Excess metal was lifted off in an acetone solution. The silicon posts were completely coated by the deposition process and became electrically addressable. Optical micrographs of the electrodes are shown in Figure 5-13. Reference electrodes were patterned as 50 μm wide leads. Working electrodes were defined as 150 μm square pads, with the 50 μm square membrane structures at the center of each individual pad. A single counter electrode, 23.1 mm long and 6330 mm^2 in area, was patterned around the working and reference electrodes. Electrical leads extended from each electrode, terminating in peripheral wirebonding pads for connection to a custom printed circuit board.

To pattern microfluidic channels, wafers were spin coated with a negative tone photoresist (SU-8) to a thickness of ~ 10 μm . After a soft bake, microfluidic channels, 1 mm wide and 24 mm long with fluidic wells 1.5 mm in diameter at each end, were patterned by contact lithography. The patterns were developed and residual resist was cleaned in an oxygen plasma. The SU-8 layer was then heated to 180 °C, to reflow and planarize the SU-8. Pictures of the membrane structures and electrodes, integrated within the microfluidic channel, are shown in Figures 5-13 and 5-14A. The ability of the reference and counter electrodes to control voltages and currents at the working electrode surface deteriorates as the distance between them increases [132]. The counter electrode was patterned to run the length of the channel, snaking around reference and working electrodes, to prevent this. One reference electrode was also patterned for every three working electrodes.

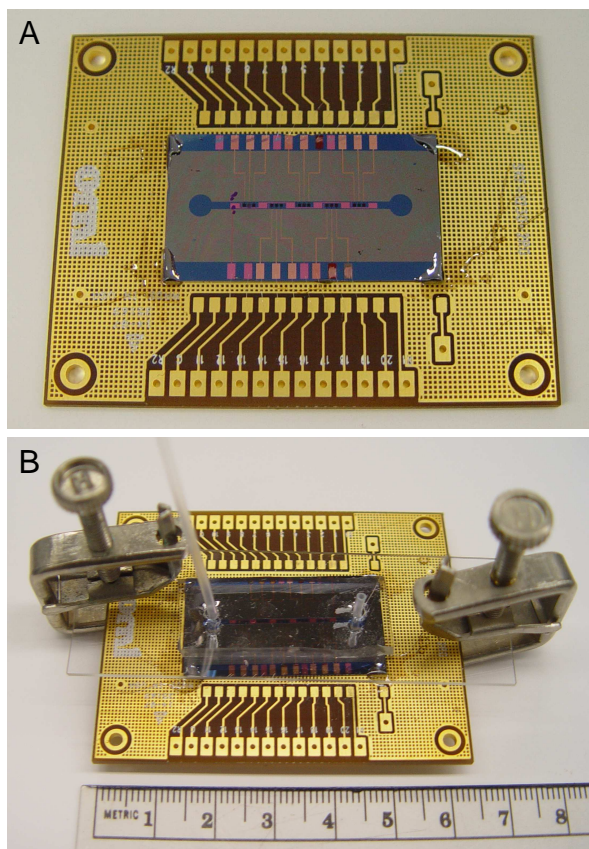


Figure 5-14) Membrane device attached to a printed circuit board. Electrodes terminate in peripheral pads that are wire-bonded to a printed circuit board. Pictures show the wire-bonded device **A)** before a PDMS lid is placed on top and **B)** after.

Pyrrole monomer was prepared as 100 mM monomer in 100 mM NaDBS solutions. Membrane devices were immersed in solution and polypyrrole was deposited on silicon posts by applying an oxidizing potential (0.7 V) to the peripheral wirebonding pads connected to them. Voltages were applied versus a Ag/AgCl reference electrode and current was controlled by a gold counter electrode. In Figure 5-13, the right pad is darker than the adjacent pads because it is coated with polypyrrole while the adjacent pads are not. Polypyrrole was deposited on both the electrode surface and the silicon posts at the center of the pad. The adjacent pads do not have a polymer film because they were not subjected to the oxidizing potential. Voltage was applied exclusively to the right pad. Because membrane structures were individually addressed, they could be selectively oxidized and reduced to deposit and actuate polymer films. Polypyrrole was typically deposited to a 350 ± 25 nm thickness, increasing the diameters of the silicon posts by 700 ± 50 nm. Electron micrographs of the membrane structures, before and after polymer deposition, are shown in Figure 5-15.

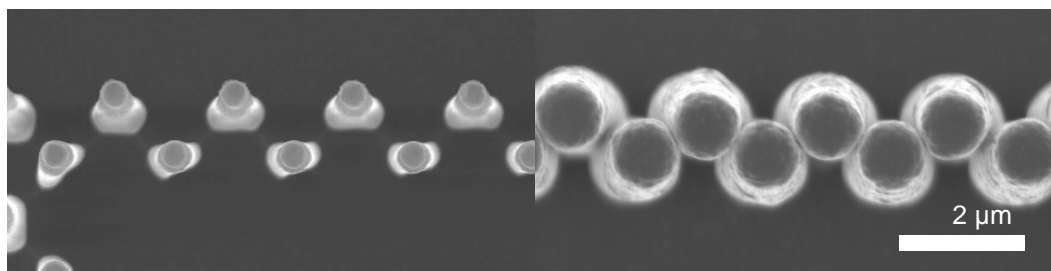


Figure 5-15) Electron micrographs of silicon posts, viewed from the top, prior to polypyrrole polymerization (LEFT) and after (RIGHT).

The membrane device was affixed to a printed circuit board with wax. Wirebonds were then made between the peripheral pads connected to the electrodes and the printed circuit board (see Figure 5-14A). Membrane structures were sealed with a 5 mm thick PDMS lid. PDMS was mixed at a 1:10 curing agent to epoxy ratio and was cured at 70 °C for 90 minutes. Sections of the PDMS were cut into rectangular lids, ~2.5 cm wide and ~3.5 cm long. Holes were punched through the PDMS and polyethylene tubing (OD 0.060") was fed through, to provide fluidic access to the underlying wells at the ends of the microfluidic channels. The PDMS lids were then aligned with the microfluidic channels and were clamped in place using small vices. A photograph of a fully assembled device is shown in Figure 5-14B. Fluid transport through the microfluidic channels was controlled by applying light finger pressure to a 3 cubic centimeter syringe through a 16 gauge needle.

To demonstrate membrane actuation, 50 nm fluorescently labeled latex beads diluted in 100 mM NaDBS, were flowed through the microfluidic channel of a membrane device. Once the channel was filled with beads, a reducing potential was applied to a single membrane structure, swelling the volume of its polymer coating. The pores of the membrane structure were closed, restricting the flow of beads through the membrane. When the reducing potential was removed, the volume of the polymer coating shrunk and the pores of the membrane structure reopened. The membrane structure refilled with beads within 30 seconds. Fluorescence micrographs of the described experiment are presented in Figure 5-16. When the pores were closed, fluorescence in the interior of the membrane structure was significantly lower than the ambient fluorescence (62% lower fluorescence intensity inside cell relative to outside the cell) (see Figure 5-16B). After the pores were reopened, the interior of the membrane structure refilled with fluorescent beads (fluorescence intensity roughly equal inside and outside the cell) (see Figure 5-16C).

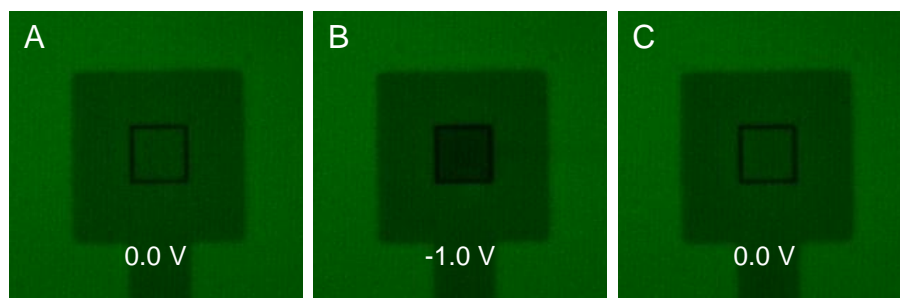


Figure 5-16) Fluorescence micrographs of a membrane structure with **A)** “opened”, **B)** “closed”, and **C)** “opened” pores. The micrograph **B)** was taken 30 seconds after -1.0 V was applied and the micrograph **C)** was taken 30 seconds after 0.0 V was applied.

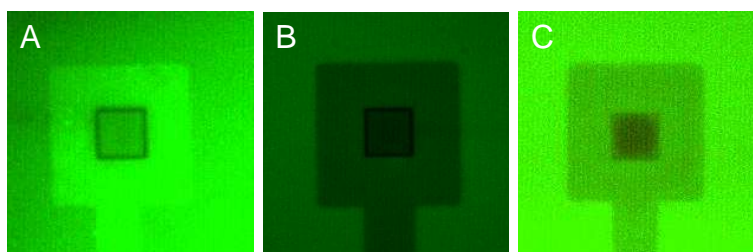


Figure 5-17) Fluorescence micrographs of membrane structures with “closed” pores. The micrographs were taken after -1.0 V was applied. Fluorescent species were **A)** fluorescently labeled streptavidin, **B)** 50 nm, **C)** and 100 nm latex beads.

The pores of the membrane structures were 100 ± 20 nm when the polypyrrole coating was in a neutral, unoxidized state. Upon reduction, the pores were reduced to ~ 0 nm, sufficiently small enough to restrict the transport of biological macromolecules through the membrane structures. On return to an unoxidized state, the pores were large enough in the open state to allow the flow of comparatively large species through. Fluorescence micrographs illustrating the size limits of the membrane structures are shown in Figure 5-17. When the pores were closed, the flow of particles as small as fluorescently labeled bovine serum albumin (~ 7 nm in diameter) through the membranes was restricted (see Figure 5-17A). When the membranes were open, particles as large as 100 nm diameter fluorescently labeled latex beads could still flow through (see Figure 5-17C).

The pores of the membranes can be made larger by depositing thinner polypyrrole films, with limits defined by the actual diameters of the silicon posts and their spacings. By tailoring the thickness of the polypyrrole films, it is possible to adjust the range of particle sizes whose transport through the membranes is affected by polymer actuation. For example, if the deposited polypyrrole film is ~ 100 nm thick, the pores of the membrane are ~ 600 nm and swelling the polymer coating dilates the pores to ~ 525 nm. If the polymer film is ~ 200 nm thick, the pores are ~ 400 nm and the dilated pores

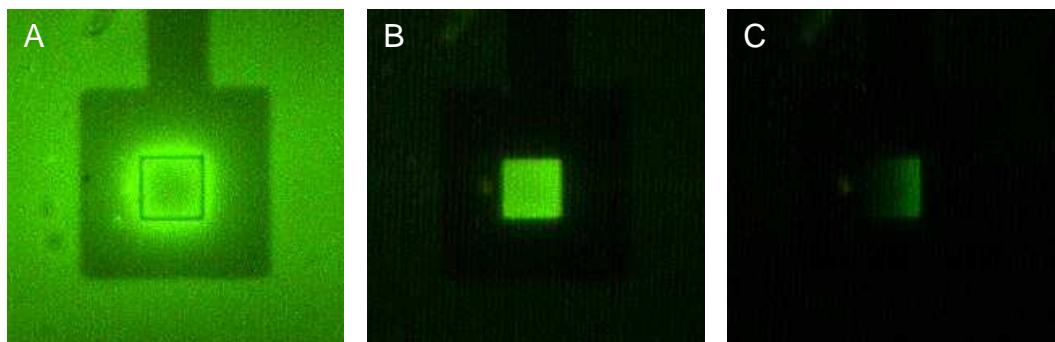


Figure 5-18) Fluorescence micrographs of a membrane structure filled with fluorescently labeled bovine serum albumin. The micrographs were taken **A)** before and **B)** 5 seconds after a -1.0 V reducing potential was applied. After 30 seconds, the reducing potential was removed. The micrograph **C)** was taken 5 seconds later.

are ~250 nm. If the polymer film is 350 nm thick, the pores are ~100 nm and the dilated pores are effectively closed (~0 nm). Depending on the thickness of the deposited polypyrrole film, the transport of particles from 25 nm to 600 nm in diameter can be affected by polymer actuation (data not shown).

Fluorescent species can be captured within and released from the membrane structures. To demonstrate, the structures were first filled with fluorescently labeled bovine serum albumin diluted in 100 mM NaDBS (see Figure 5-18A). The polypyrrole-coated silicon posts were then subjected to a reducing potential, closing the pores of the membrane structures. The channel was washed with 100 mM NaDBS to clear the channel of fluorescent species while fluorescently-labeled protein remained contained within the membrane structures (see Figure 5-18B). Captured species were contained within the structures for ~45 seconds, with a small amount of leakage occurring over that time period (1% decrease in fluorescence). Fluorescent protein was then released from the membrane structures by returning the polypyrrole-coated silicon posts to a neutral oxidation state (see Figure 5-18C). Fluorescent species were immediately released from the membrane structures (20% decrease in fluorescence after 1 second). Within 10 seconds, captured protein was completely evacuated from the membrane structures, with fluorescence within the structures equal to ambient fluorescence.

The underlying oxide passivation layer that was deposited during device fabrication was of poor quality. Reducing potentials (-1.0 V), applied for prolonged periods or in multiple sequential actuations, would cause the oxide layer to break down and current leakage to occur between electrodes. As a result, devices would fail relatively quickly (3-4 actuation experiments). The fragility of the device hindered the measurement of characteristics such as the maximum hold times for captured species.

However, the devices still demonstrate excellent potential as a platform for lab-on-a-chip based cell cultures, systems biology studies, and biosensing and drug delivery applications. Species, as small as proteins, were contained in and released from the membrane structures. Membranes constructed from silicon posts were robust enough to withstand high temperature (350 °C) and relatively caustic chemical processing. As a result, the membrane structures were readily integrated within multi-scale microfluidic and electronic devices.

5.4 *Conclusions*

Vertically aligned carbon nanofibers can be grown from catalyst metals patterned using micro-scale lithographic techniques. The resulting forests of nanofibers can be used to form membranes with nano-scale pores. However, the inherently stochastic nature of VACNF synthesis limits their application as pore-forming structures within synthetic membranes. Alternatively, membrane components can be patterned and anisotropically etched from silicon to form membranes with well defined, nano-scale pores. The main advantage of synthesizing membranes this way is that the resulting pore-forming structures have uniform dimensions, geometries, alignments, and interfiber spacings. Resulting pores are well defined at precise spatial locations. Membrane structures, constructed by anisotropically etching silicon, were robust enough to withstand caustic chemical and high temperature processing. As a result, the membrane structures readily integrated within multi-scale systems. By depositing the actuable polymer, polypyrrole, on the membrane structures, it was possible to modulate the permeability of the membranes. Species as small as proteins were contained in and released from the membrane structures.

The resulting devices were relatively fragile and would break upon prolonged or rigorous use. However, this problem might be solved by improving the passivation layer deposited during device fabrication. Higher quality thermal oxides or thicker layers of PECVD oxides would be more resistant to breakdown. The design of the membrane could also be improved. Membranes were constructed from relatively small post structures (cylinders 500-800 nm in diameter and 12 μm in height). The resulting membranes have extremely high permeabilities, so transport of species is extremely rapid relative to other synthetic nanoporous membranes. However, the membranes were

constructed from a large number (~200) silicon posts. If a single post was flawed, the efficacy of the device was severely affected. As a result, the yield from the fabrication process was relatively low and resulting membrane structures were relatively fragile. The design of the device could be improved to increase process yield and device robustness.

Chapter 6

Conclusions

The work presented in this dissertation describes the synthesis and testing of a novel platform for studying biochemical reactions within synthetic cellular-scale structures. The platform features robust, nanoporous membranes that readily integrate within microfabricated structures and devices. Initially, membranes were constructed from stochastic forests of vertically aligned carbon nanofibers. VACNFs could be patterned and synthesized using micro-scale fabrication techniques to form membranes with nanoscale pores. The pores of the membrane were defined by the spacings between fibers, with the fibers acting as obstacles to the flow of species perpendicular to the substrate. Size selective transport of species through the VACNF membranes was demonstrated. Particles, as small as 500 nm, were totally restricted from passing through the membranes while smaller particles were allowed to flow through.

An actuatable polymer, polypyrrole, was then electrochemically deposited on the active surface areas of the VACNFs. The dimensions of the fibers were altered by the polymer coatings. Polymerization reaction parameters were evaluated to determine which parameter produced the most linear, reproducible response in film growth rate and quality. Polymerization time was found to be easily adjustable and to have a linear relationship with polymer film thickness. The ability to tailor the dimensions of the VACNFs was demonstrated by controllably coating the fibers with nanoscale thin films of polypyrrole. Individual and/or small groups of fibers within a larger array were modified with the polymer films.

Nanoporous actuatable membranes were then fabricated by coating stochastic forests of VACNFs with polypyrrole. The stochastic forests were patterned and grown in the shape of hollow square cells. Polypyrrole was then electrochemically deposited on the nanofibers to reduce their diameters and their interfiber spacings. The polymer coatings were oxidized and reduced by externally applied electrical potentials, resulting in volume shrinking and swelling of the polymer. The volume changes modulated the interfiber spacings of the VACNF membranes. As a result, the pores of the membranes

could be induced to open and dilate by externally applied electrical stimuli. To evaluate the effect of the polymer volume changes on the permeability of the membranes, fluorescently labeled species were flowed through and were observed. When the polymer coatings on the VACNFs were electrochemically reduced, the membranes were shown to restrict the flow of the particles according to their size. When the polymer coatings were in the oxidized or neutral state, species were shown to more freely flow through the membranes.

Membranes constructed from stochastic forests of VACNFs demonstrated a couple significant limitations. The stochastic placement of nanofibers led to leaks within the membrane walls at discrete locations. This problem could be corrected by defining catalyst sites using nanoscale lithographic techniques. Accurate placement of individual membrane components allowed for better definition of interfiber spacings and for the synthesis of nanofibers with more uniform geometries. However, the VACNF synthesis process is affected by parameters currently beyond control and/or understanding. The geometries of resulting carbon nanofibers always feature a certain degree of inherent stochasticity, limiting their application as pore-forming structures within nanoporous membranes.

Alternatively, membranes were constructed by patterning and anisotropically etching features in silicon. Resulting membranes were formed from structures with extremely uniform dimensions, geometries, alignments, and interfiber spacings. The pores were well defined at precise spatial locations. Additionally, the membrane structures were robust enough to withstand caustic chemical and high temperature processing. As a result, the membrane structures were readily integrated within multi-scale systems. Membranes were integrated within a microfluidic channel with working, counter, and reference electrodes. The resulting microfluidic system had better flow control and tighter sealing than previous iterations of the device. Depositing polypyrrole on the membrane structures enabled the ability to modulate the permeabilities of the membranes.

Devices were relatively fragile and would break down upon prolonged or rigorous use. However, this problem can be solved by making improvements to the device fabrication process. Specifically, attempts should be made to synthesize devices with higher quality thermal oxides or thicker layers of PECVD oxides. The design of the membrane could also be improved. The size of the membrane structures should be further reduced and alternative pore-forming structures should be considered. The small

post structures that formed the pores of the membranes described within this dissertation were cylinders, 500-800 nm in diameter and 12 μm in height. The resulting membranes had extremely high permeabilities and extremely rapid transport of species relative to other synthetic nanoporous membranes. However, the membranes were subject to failure if a single membrane component was flawed or damaged. As a result, process yield was relatively low and resulting membrane structures were relatively fragile.

Despite the described limitations, the membrane structures were capable of containing and releasing species as small as biological macromolecules, suggesting their possible application as small volume reaction containers for chemical sensing and protein production. While the size of the membrane structures (50 μm squares) is roughly an order of magnitude larger than the typical size of biological cells, the potential of the nanoporous membranes to form cellular scale systems is apparent. Several challenges were overcome including the engineering of features on multiple length scales, the integration and control of nanoscale systems, and the characterization of resulting devices. The work described in this dissertation represents a first step toward realizing the engineering ideals represented by the biological cell. Further developments will lead to technologies capable of integrating functionality within nanoscale systems for medical diagnostics and treatment.

References

1. A.V. Melechko, V.I. Merkulov, T.E. McKnight, M.A. Guillorn, K.L. Klein, D.H. Lowndes, and M.L. Simpson, *J. Appl. Phys.*, 97 (2005) 041301.
2. Y. Mao, S. Chang, S. Yang, Q. Ouyang, and L. Jiang, *Nature Nanotechnology*. 2 (2007) 366.
3. L. Bay, T. Jacobsen, S. Skaarup, and K. West, *J. Phys. Chem. B*. 105 (2001) 8492.
4. S.H. Cho, K.T. Song, and J.Y. Lee, *Conjugated Polymers: Theory, Synthesis, Properties, and Characterization*, 3rd ed., *Handbook of Conducting Polymers*, CRC Press, New York, 2007.
5. V.I. Merkulov, D.H. Lowndes, Y.Y. Wei, G. Eres, and E. Voelkl, *Appl. Phys. Lett.*, 76 (2000) 3555.
6. E. Smela, *Adv. Mater.*, 15 (2003) 481.
7. H. Cui, X. Yang, M.L. Simpson, D.H. Lowndes, and M. Varela, *Appl. Phys. Lett.*, 84 (2004) 4077.
8. S. Sadki, P. Schottland, N. Brodie, and G. Sabouraud, *Chem. Soc. Rev.*, 29 (2000) 283.
9. Q. Pei and O. Inganäs, *J. Phys. Chem.*, 97 (1993) 6034.
10. K.L. Klein, A.V. Melechko, T.E. McKnight, S.T. Retterer, P.D. Rack, J.D. Fowlkes, D.C. Joy, and M.L. Simpson, *J. Appl. Phys.*, 103 (2008) 061301.
11. V.I. Merkulov, A.V. Melechko, M.A. Guillorn, M.L. Simpson, D.H. Lowndes, J.H. Whealton, and R.J. Raridon, *Appl. Phys. Lett.*, 80 (2002) 4816.
12. T.E. McKnight, A.V. Melechko, M.A. Guillorn, V.I. Merkulov, M.J. Doktycz, C.T. Culbertson, S.C. Jacobson, D.H. Lowndes, and M.L. Simpson, *J. Phys. Chem. B*. 107 (2003) 10722.
13. O.B. Barbara Walker, Stephen Cheley, Hagan Bayley, *Chemistry and Biology*. 2 (1995) 99.
14. S. Helveg, C. Lopez-Cartes, J. Sehested, P.L. Hansen, B.S. Clausen, J.R. Rostrup-Nielsen, F. Abild-Pedersen, and J.K. Nerskov, *Nature*. 427 (2004) 426.
15. V.I. Merkulov, M.A. Guillorn, D.H. Lowndes, M.L. Simpson, and E. Voelkl, *Appl. Phys. Lett.*, 79 (2001) 1178.
16. T.E. McKnight, A.V. Melechko, B.L. Fletcher, S.W. Jones, D.K. Hensley, D.B. Peckys, G.D. Griffin, M.L. Simpson, and M.N. Ericson, *J. Phys. Chem. B*. 110 (2006) 15317.
17. B.J. Hinds, N. Chopra, T. Rantell, R. Andrews, V. Gavalas, and L.G. Bachas, *Science*. 303 (2004) 62.
18. G. Che, S.A. Miller, E.R. Fisher, and C.R. Martin, *Anal. Chem.*, 71 (1999) 3187.
19. P.J. Kemery, J.K. Steehler, and P.W. Bohn, *Langmuir*. 14 (1998) 2884.
20. J. Li, D. Stein, C. McMullan, D. Branton, M.J. Aziz, and J.A. Golovchenko, *Nature*. 412 (2001) 166.
21. M. Banghart, K. Borges, E. Isacoff, D. Trauner, and R.H. Kramer, *Nat. Neurosci.*, 7 (2004) 1381.
22. A. Kocer, M. Walko, W. Meijberg, and B.L. Feringa, *Science*. 309 (2005) 755.
23. H.C. Berg and D.A. Brown, *Nature*. 239 (1972) 500.
24. L. Bousse, *Sensors and Actuators B*. 34 (1996) 270.

25. J.W. Costerton, Z. Lewandowski, D.E. Caldwell, D.R. Korber, and H.M. Lappin-Scott, *Annu. Rev. Microbiol.*, 49 (1995) 711.
26. M. Farina, D.M.S. Esquivel, and H.G.P.L. DeBarros, *Nature*. 343 (1990) 256.
27. N.H.H. James D. Watson, Jeffrey W. Roberts, Joan Argetsinger Steitz, Alan M. Weiner, *Molecular Biology of the Gene*, Third ed, Benjamin/Cummings, Menlo Park, CA, 1987.
28. C.C.R. M. J. Engler, *The Enzyme*, Third ed, Academic Press, New York, NY, 1982.
29. L.M. Adleman, *Science*. 266 (1994) 1021.
30. R.C. Merkle, *Nanotechnology*. 4 (1993) 21.
31. T.D. Schneider, *J. Theor. Biol.*, 148 (1991) 125.
32. F.M. Harold, *Microbiol. Mol. Biol. Rev.*, 69 (2005) 544.
33. P.W. Hochachka, *Proceedings of the National Academy of Science of the United States of America*. 96 (1999) 12233.
34. D.B. Bruce Alberts, Julian Lewis, Martin Raff, Keith Roberts, James D. Watson, *Molecular Biology of the Cell*, Third ed, Garland, New York, NY, 1994.
35. F.M. A. Hernandez, J. A. Ibanez, J. I. Arribas, A. F. Tejerina, *Separation Science and Technology*. 21 (1986) 665.
36. L.F.L. Joseph D. Henry, C. H. Alex Kuo, *AIChE Journal*. 23 (1977) 851.
37. M.L. Marianne Nystrom, Einar Matthiasson, *Colloids and Surfaces*. 36 (1989) 297.
38. C.J.B. Barbara Ballarin, Del R. Lawson, Wenbin Liang, Leon S. VanDyke, Charles R. Martin, *Analytical Chemistry*. 64 (1992) 2647.
39. K.K. Masao Sugawara, Hiroyuki Sazawa, Yoshio Umezawa, *Analytical Chemistry*. 59 (1987) 2842.
40. C.R.M. Yoshio Kobayashi, *Analytical Chemistry*. 71 (1999) 3665.
41. J.L.T. Zheng Yan Wu, Zhi Lang Cheng, Xiu Rong Yang, Erkang Wang, *Analytical Chemistry*. 72 (2000) 6030.
42. G.B.K. J. C. Keister, *Journal of Membrane Science*. 71 (1992) 257.
43. J.C. Lorraine M. A. Nolan, Owen I. Corrigan, *Journal of the Chemical Society - Faraday Transactions*. 89 (1993) 2839.
44. G.L.A. Steven P. Schwendeman, Mark E. Meyerhoff, Robert J. Levy, *Macromolecules*. 25 (1992) 2531.
45. R.E.B. Sandeep K. Dalvie, *Journal of Membrane Science*. 71 (1992) 247.
46. C.R. Martin, *Science*. 266 (1994) 1961.
47. W.R. Pornphan Makphon, Somporn Chongkum, Supawan Tantayanon, *Journal of Applied Polymer Science*. 101 (2006) 982.
48. R.M.C. Li Sun, *Journal of the American Chemical Society*. 122 (2000) 12340.
49. V.Y.Y. Scott A. Miller, Charles R. Martin, *Journal of the American Chemical Society*. 123 (2001) 12335.
50. J.H.C. A. J. Storm, X. S. Ling, H. W. Zandbergen, C. Dekker, *Nature Materials*. 2 (2003) 537.
51. D.S. Jiali Li, Ciaran McMullan, Daniel Branton, Michael J. Aziz, Jene A. Golovchenko, *Nature*. 412 (2001) 166.
52. E.C.C. Lotien Richard Huang, Robert H. Austin, James C. Sturm, *Science*. 304 (2004) 987.

53. J.T. S. Bhakdi, *Microbiological Reviews*. 55 (1991) 733.
54. G. Menestrina, *Journal of Membrane Biology*. 90 (2005) 177.
55. H. Bayley, *Bioorg. Chem.*, 23 (1995) 340.
56. M.K. G. S. Gray, *Infection and Immunity*. 46 (1984) 615.
57. T.N. Hajime Ikigai, *Biochemical and Biophysical Research Communications*. 130 (1985) 175.
58. R.F. S. Bhakdi, J. Tranumjensen, *Proceedings of the National Academy of Science of the United States of America - Biological Sciences*. 78 (1981) 5475.
59. B. Walker and H. Bayley, *Protein Eng.*, 7 (1994) 91.
60. J.K. Barbara Walker, Musti Krishnasastry, Hagan Bayley, *Protein Engineering*. 7 (1994) 655.
61. N.M. Tracy Milburn, Andrew P. Billington, Jayant B. Udgaonkar, Jeffery W. Walker, Barry K. Carpenter, Watt W. Webb, Jeffrey Marque, Winfried Denk, James A. McCray, George P. Hess, *Biochemistry*. 28 (1989) 49.
62. B.N. Chung-yu Chang, Barbara Walker, Hagan Bayley, *Chemistry and Biology*. 2 (1995) 391.
63. W. Denk, *Proceedings of the National Academy of Science of the United States of America*. 91 (1994) 6629.
64. C.M. Niemeyer and C.A. Mirkin, *Nanobiotechnology*, Wiley-VCH, Weinheim, 2004.
65. R.O. Blaustein, P.A. Cole, C. Williams, and C. Miller, *Nat. Struct. Biol.*, 7 (2000) 309.
66. G.A. Woolley, A.S.I. Jaikaran, Z. Zhang, and S. Peng, *J. Am. Chem. Soc.*, 117 (1995) 4448.
67. V. Borisenko, Z. Zhang, and G.A. Woolley, *Biochimica et Biophysica Acta - Biomembranes*. 1558 (2002) 26.
68. A.S. Arseniev, I.L. Barsukov, V.F. Bystrov, A.L. Lomize, and Y.A. Ovchinnikov, *FEBS Lett.*, 186 (1985) 168.
69. R. Smith, D.E. Thomas, F. Separovic, A.R. Atkins, and B.A. Cornell, *Biophys. J.*, 56 (1989).
70. F. Kovacs, J. Quine, and T.A. Cross, *Proceedings of the National Academy of Science of the United States of America*. 96 (1999) 7910.
71. E. Kleinpeter, M. Kretschmer, R. Borsdorf, R. Widera, and M. Muhlstadt, *Journal fur Praktische Chemie*. 322 (1980) 793.
72. O. Muraoka, T. Minematsu, J. Tsuruzawa, and T. Momose, *Heterocycles*. 23 (1985) 853.
73. S.K. Dalvie and R.E. Baltus, *J. Membr. Sci.*, 71 (1992) 247.
74. P. Makphon, W. Ratanatongchai, S. Chongkum, and S. Tantayanon, *J. Appl. Polym. Sci.*, 101 (2006) 982.
75. S.A. Miller, V.Y. Young, and C.R. Martin, *J. Am. Chem. Soc.*, 123 (2001) 12335.
76. L. Sun and R.M. Crooks, *J. Am. Chem. Soc.*, 122 (2000) 12340.
77. A.J. Storm, J.H. Chen, X.S. Ling, H.W. Zandbergen, and C. Dekker, *Nature Materials*. 2 (2003) 537.
78. C. Nardin, J. Widmer, M. Winterhalter, and W. Meier, *European Physical Journal E*. 4 (2001) 403.

79. D.D. Lasic, *Liposomes: From Physics to Applications*, Elsevier Science Publications, Amsterdam, 1993.
80. C. Nardin, S. Thoeni, J. Widmer, M. Winterhalter, and W. Meier, *Chem. Commun.*, (2000) 1433.
81. H. Nikaido, *Mol. Microbiol.*, 6 (1992) 435.
82. C. Daubresse, T. SergentEngelen, E. Ferain, Y.J. Schneider, and R. Legras, *Nuclear Instruments and Methods in Physics Research Section B - Beam Interactions with Materials and Atoms*. 105 (1995) 126.
83. P. Gais, J. Jakes, and H. Schraube, *Radiat. Measur.*, 25 (1995) 767.
84. I.M. Yamazaki, R. Paterson, and L.P. Geraldo, *J. Membr. Sci.*, 118 (1996) 239.
85. A. Alves, P.N. Johnston, P. Reichart, D.N. Jamieson, and R. Siegele, *Nuclear Instruments and Methods in Physics Research Section B - Beam Interactions with Materials and Atoms*. 260 (2007) 431.
86. T. Nenadovic, B. Perraillon, Z. Bogdanov, Z. Djordjevic, and M. Milic, *Nuclear Instruments and Methods in Physics Research Section B - Beam Interactions with Materials and Atoms*. 48 (1990) 538.
87. T.-C. Kuo, L.A. Sloan, J.V. Sweedler, and P.W. Bohn, *Langmuir*. 17 (2001) 6298.
88. K.-Y. Chun and P. Stroeve, *Langmuir*. 18 (2002) 4653.
89. Z.Z. Huo, N.L. Abbott, and P. Stroeve, *Langmuir*. 16 (2000) 2401.
90. P. Kohli, C.C. Harrell, Z. Cao, R. Gasparac, W. Tan, and C.R. Martin, *Science*. 305 (2004) 984.
91. I. Vlassiounk, C.-D. Park, S.A. Vail, D. Gust, and S. Smirnov, *Nano Lett.*, 6 (2006) 1013.
92. F. Buyukserin, P. Kohli, M.O. Wirtz, and C.R. Martin, *Small*. 3 (2007) 266.
93. P. Nednoor, N. Chopra, V. Gavalas, L.G. Bachas, and B.J. Hinds, *Chem. Mater.*, 17 (2005) 3595.
94. J.L. Bahr and J.M. Tour, *Chem. Mater.*, 13 (2001) 3823.
95. M.A. Hamon, H. Hui, P. Bhowmik, H.M.E. Itkis, and R.C. Haddon, *Applied Physics A - Materials Science and Processing*. 74 (2002) 333.
96. C.V. Nguyen, L. Delzeit, A.M. Cassell, J. Li, J. Han, and M. Meyyappan, *Nano Lett.*, 2 (2002) 1079.
97. R. Karnik, K. Castelino, and A. Majumdar, *Appl. Phys. Lett.*, 88 (2006) 123114.
98. B. Samel, P. Griss, and G. Stemme, *Journal of Microelectromechanical Systems*. 16 (2007) 50.
99. X. Duan, Y. Huang, Y. Cui, J. Wang, and C.M. Lieber, *Nature*. 409 (2001) 66.
100. M.H. Huang, Y. Wu, H. Feick, N. Tran, E. Weber, and P. Yang, *Adv. Mater.*, 13 (2001) 113.
101. W.I. Park, D.H. Kim, S.-W. Jung, and G.-C. Yi, *Appl. Phys. Lett.*, 80 (2002) 4232.
102. B.L. Fletcher, E.D. Hullander, A.V. Melechko, T.E. McKnight, K.L. Klein, D.K. Hensley, J.L. Morrell, M.L. Simpson, and M.J. Doktycz, *Nano Lett.*, 4 (2004) 1809.
103. J.D. Fowlkes, B.L. Fletcher, E.D. Hullander, K.L. Klein, D.K. Hensley, A.V. Melechko, M.L. Simpson, and M.J. Doktycz, *Nanotechnology*. 16 (2005) 3101.
104. J.D. Fowlkes, E.D. Hullander, B.L. Fletcher, S.T. Retterer, A.V. Melechko, D.K. Hensley, M.L. Simpson, and M.J. Doktycz, *Nanotechnology*. 17 (2006) 5659.

105. G.T.A. Kovacs, N.I. Maluf, and K.E. Petersen, *Proceedings of the IEEE*. 86 (1998) 1536.
106. B.L. Fletcher, T.E. McKnight, J.D. Fowlkes, D.P. Allison, M.L. Simpson, and M.J. Doktycz, *Synth. Met.*, 157 (2007) 282.
107. A.F. Diaz and J.I. Castillo, *J. Chem. Soc. - Chem. Comm.*, (1980) 397.
108. A.F. Diaz, K.K. Kanazawa, and G.P. Gardini, *J. Chem. Soc. - Chem. Comm.*, (1979) 635.
109. A.F. Diaz, J.M.V. Vallejo, and A.M. Duran, *IBM Journal of Research and Development*. 25 (1981) 42.
110. K.K. Kanazawa, A.F. Diaz, R.H. Geiss, W.D. Gill, J.F. Kwak, J.A. Logan, J.F. Rabolt, and G.B. Street, *J. Chem. Soc. - Chem. Comm.*, (1979) 854.
111. R.C.D. Peres, M.A. De Paoli, and R.M. Torresi, *Synth. Met.*, 48 (1992) 259.
112. E. Smela and N. Gadegaard, *Adv. Mater.*, 11 (1999) 953.
113. R.M. Torresi, S.I.C. de Torresi, T. Matencio, and M.A. De Paoli, *Synth. Met.*, 72 (1995) 283.
114. M. Endo, Y.A. Kim, T. Hayashi, Y. Fukai, K. Oshida, M. Terrones, T. Yanagisawa, S. Higaki, and M.S. Dresselhaus, *Appl. Phys. Lett.*, 80 (2002) 1267.
115. A. Krishnan, E. Dujardin, M.M.J. Treacy, J. Hugdahl, S. Lynam, and T.W. Ebbesen, *Nature*. 388 (1997) 451.
116. B.L. Fletcher, T.E. McKnight, A.V. Melechko, D.K. Hensley, D.K. Thomas, M.N. Ericson, and M.L. Simpson, *Advanced Materials*. 18 (2006) 1689.
117. W.D.J. Callister, *Materials Science and Engineering an Introduction*, Sixth ed, Wiley, New York, 2003.
118. B. McEnaney, *Encyclopedia of Materials: Science and Technology*, Amsterdam, New York, 2001.
119. R. Gao, Z.L. Wang, Z. Bai, W.A. de Heer, L. Dai, and M. Gao, *Phys. Rev. Lett.*, 85 (2000) 622.
120. B.L. Fletcher, T.E. McKnight, A.V. Melechko, M.L. Simpson, and M.J. Doktycz, *Nanotechnology*. 17 (2006) 2032.
121. Y. Lin, F. Lu, Y. Tu, and Z. Ren, *Nano Lett.*, 4 (2004) 191.
122. T.E. McKnight, A.V. Melechko, G.D. Griffin, M.A. Guillorn, V.I. Merkulov, F. Serna, D.K. Hensley, M.J. Doktycz, D.H. Lowndes, and M.L. Simpson, *Nanotechnology*. 14 (2003) 551.
123. M.S. Dresselhaus, *Carbon: Bonding*, in *Encyclopedia of Materials: Science and Thechnology*. 2001, Elsevier Science: New York, NY.
124. T.E. McKnight, A.V. Melechko, D.W. Austin, T. Sims, M.A. Guillorn, and M.L. Simpson, *J. Phys. Chem. B*. 108 (2004) 7115.
125. T.E. McKnight, A.V. Melechko, D.K. Hensley, D.G.J. Mann, G.D. Griffin, and M.L. Simpson, *Nano Lett.*, 4 (2004) 1213.
126. M.A. Guillorn, X. Yang, A.V. Melechko, D.K. Hensley, M.D. Hale, V.I. Merkulov, M.L. Simpson, L.R. Baylor, W.L. Gardner, and D.H. Lowndes, *Journal of Vacuum Science & Technology B*. 22 (2004) 35.
127. F. Hoshi, K. Tsugawa, A. Goto, T. Ishikura, S. Yamashita, M. Yumura, T. Hirao, K. Oura, and Y. Koga, *Diamond Relat. Mater.*, 10 (2001) 254.
128. J.S. Moon, P.S. Alegaonkar, J.H. Han, T.Y. Lee, J.B. Yoo, and J.M. Kim, *J. Appl. Phys.*, 100 (2006).

129. B.L. Fletcher, J. Fern, K. Rhodes, T.E. McKnight, J.D. Fowlkes, S.T. Retterer, D.J. Keffer, M.L. Simpson, and M.J. Doktycz, *Electrochem. Commun.*, (2008).
130. S.-B. Lee, K.B.K. Teo, M. Chhowalla, D.G. Hasko, G.A.J. Amaratunga, W.I. Milne, and H. Ahmed, *Microelectron. Eng.*, 61-62 (2002) 475.
131. L. Zhang, D. Austin, V.I. Merkulov, A.V. Melechko, K.L. Klein, M.A. Guillorn, D.H. Lowndes, and M.L. Simpson, *Appl. Phys. Lett.*, 84 (2004) 3972.
132. A.J. Bard and L.R. Faulker, *Electrochemical Methods: Fundamentals and Applications*, John Wiley and Sons, New York, NY, 2001.
133. R.L. McCreery, *Electroanalytical Chemistry*, Marcel Dekker, New York, 1991.
134. Y. Tu, Y. Lin, and Z. Ren, *Nano Lett.*, 3 (2003) 107.
135. J. Li, H.T. Ng, A. Cassell, W. Fan, H. Chen, Q. Ye, J. Koehne, J. Han, and M. Meyyappan, *Nano Lett.*, 3 (2003) 597.
136. M.A. Correa-Duarte, N. Wagner, J. Rojas-Chapana, C. Morszeck, M. Thie, and M. Giersig, *Nano Lett.*, 4 (2004) 2233.
137. T.J. Webster, M.C. Waid, J.L. McKenzie, R.L. Price, and J.U. Ejiofor, *Nanotechnology*. 15 (2004) 48.
138. S. Iijima, *Nature*. 354 (1991) 56.
139. W. Kratschmer, L.D. Lamb, K. Fostiropoulos, and D.R. Huffman, *Nature*. 347 (1990) 354.
140. H.W. Kroto, J.R. Heath, S.C. O'Brien, R.F. Curl, and R.E. Smalley, *Nature*. 318 (1985) 162.
141. M. Chhowalla, K.B.K. Teo, C. Ducati, N.L. Rupesinghe, G.A.J. Amaratunga, A.C. Ferrari, D. Roy, J. Robertson, and W.I. Milne, *J. Appl. Phys.*, 90 (2001) 5308.
142. V.I. Merkulov, A.V. Melechko, M.A. Guillorn, D.H. Lowndes, and M.L. Simpson, *Appl. Phys. Lett.*, 80 (2002) 476.
143. Z. Ren, Z.P. Huang, D.Z. Wang, J.G. Wen, J.W. Xu, J.H. Wang, L.E. Calvet, J. Chen, J.F. Klemic, and M.A. Reed, *Appl. Phys. Lett.*, 75 (1999) 1086.
144. R.T.K. Baker, *Carbon*. 27 (1989) 315.
145. N.M. Rodriguez, *J. Mater. Res.*, 8 (1993) 3233.
146. P.M. Ajayan, *Nature*. 427 (2004) 402.
147. J.H. Yim, S. Choi, S. Lee, and K.H. Koh, *Journal of Vacuum Science & Technology B*. 22 (2004) 1308.
148. C. Bower, W. Zhu, S.H. Jin, and O. Zhou, *Appl. Phys. Lett.*, 77 (2000) 830.
149. K.B.K. Teo, M. Chhowalla, G.A.J. Amaratunga, W.I. Milne, D.G. Hasko, G. Pirio, P. Legagneux, F. Wyczisk, and D. Pribat, *Appl. Phys. Lett.*, 79 (2001) 1534.
150. H. Shirakawa, E.J. Louis, A.G. MacDiarmid, C.K. Chiang, and A.J. Heeger, *J. Chem. Soc. - Chem. Comm.*, (1977) 578.
151. J.H. Burroughes, D.D.C. Bradley, A.R. Brown, R.N. Marks, K. Mackay, R.H. Friend, P.L. Burns, and A.B. Holmes, *Nature*. 347 (1990) 539.
152. C.D. Dimitrakopoulos and P.R.L. Malenfant, *Adv. Mater.*, 14 (2002) 99.
153. S.R. Forrest, *Nature*. 428 (2004) 911.
154. R.H. Friend, R.W. Gymer, A.B. Holmes, J.H. Burroughes, R.N. Marks, C. Taliani, D.D.C. Bradley, D.A. Dos Santos, J.L. Bredas, M. Logdlund, and W.R. Salaneck, *Nature*. 397 (1999) 121.

155. D.J. Gundlach, Y.Y. Lin, T.N. Jackson, S.F. Nelson, and D.G. Schlom, *IEEE Electron Device Lett.*, 18 (1997) 87.
156. O. Mermer, G. Veeraraghavan, T.L. Francis, Y. Sheng, D.T. Nguyen, M. Wohlgenannt, A. Kohler, M.K. Al-Suti, and M.S. Khan, *Phys. Rev. B.* 72 (2005).
157. O.A. Sadik, *Electroanalysis.* 11 (1999) 839.
158. M. Shtein, J. Mapel, J.B. Benziger, and S.R. Forrest, *Appl. Phys. Lett.*, 81 (2002) 268.
159. B.L. Groenendaal, F. Jonas, D. Freitag, H. Pielartzik, and J.R. Reynolds, *Adv. Mater.*, 12 (2000) 481.
160. Y. Kudoh, S. Tsuchiya, T. Kojima, M. Fukuyama, and S. Yoshimura, *Synth. Met.*, 41 (1991) 1133.
161. E. Smela, *J. Micromech. Microeng.*, 9 (1999) 1.
162. E. Smela and N. Gadegaard, *J. Phys. Chem. B.* 105 (2001) 9395.
163. T.A. Skotheim, *Handbook of Conducting Polymers*, Marcel Dekker, New York, 1986.
164. J.L. Bredas, J.C. Scott, K. Yakushi, and G.B. Street, *Phys. Rev. B.* 30 (1984) 1023.
165. J.L. Bredas, B. Themans, J.M. Andre, R.R. Chance, and R. Silbey, *Synth. Met.*, 9 (1984) 265.
166. A.F. Diaz and J. Barcon, *Handbook of Conducting Polymers*, Marcel Dekker, New York, NY, 1986.
167. C.P. Andrieux, P. Audebert, P. Hapiot, and J.M. Saveant, *J. Phys. Chem.*, 95 (1991) 10158.
168. G.B. Street, T.C. Clarke, M. Krounbi, K.K. Kanazawa, V. Lee, P. Pfluger, J.C. Scott, and G. Weiser, *Molecular Crystals and Liquid Crystals.* 83 (1982) 1285.
169. J. Rodriguez, H.J. Grande, and T.F. Otero, *Conductive Polymers: Synthesis and Electrical Properties. Handbook of Organic Conductive Molecules and Polymers*, John Wiley and Sons, New York, 1997.
170. S.P. Armes, *Synth. Met.*, 20 (1987) 365.
171. V. Bocchi and G.P. Gardini, *J. Chem. Soc. - Chem. Comm.*, (1986) 148.
172. Y. Kudoh, *Synth. Met.*, 79 (1996) 17.
173. M. Omastova, M. Trchova, J. Kovarova, and J. Stejskal, *Synth. Met.*, 138 (2003) 447.
174. J. Stejskal, M. Omastova, S. Fedorova, J. Prokes, and M. Trchova, *Polymer.* 44 (2003) 1353.
175. M. Salmon, K.K. Kanazawa, A.F. Diaz, and M. Krounbi, *Journal of Polymer Science Part C - Polymer Letters.* 20 (1982) 187.
176. V. Tabard-Cossa, M. Godin, P. Grutter, I. Burgess, and R.B. Lennox, *J. Phys. Chem. B.* 109 (2005) 17531.
177. M. Ogasawara, K. Funahashi, T. Demura, T. Hagiwara, and K. Iwata, *Synth. Met.*, 14 (1986) 61.
178. T.F. Otero and C. Santamaria, *Electrochim. Acta.* 37 (1992) 297.
179. A.F. Diaz and B. Hall, *IBM Journal of Research and Development.* 27 (1983) 342.
180. J.M. Ko, H.W. Rhee, S.-M. Park, and C.Y. Kim, *J. Electrochem. Soc.*, 137 (1990) 905.

181. K. Imanishi, M. Satoh, Y. Yasuda, R. Tsushima, and S. Aoki, *J. Electroanal. Chem.*, 242 (1988) 203.
182. S. Biallozor and A. Kupniewska, *Synth. Met.*, 155 (2005) 443.
183. M. Schirmeisen and F. Beck, *J. Appl. Electrochem.*, 19 (1989) 401.
184. J.H. Chen, Z.P. Huang, D.Z. Wang, S.X. Yang, J.G. Wen, and Z. Ren, *Applied Physics A - Materials Science and Processing*. 73 (2001) 129.
185. T.D.B. Nguyen-Vu, H. Chen, A.M. Cassell, R. Andrews, M. Meyyappan, and J. Li, *Small*. 2 (2006) 89.
186. J.A. Dean, *Lange's Handbook of Chemistry*, 14th ed, McGraw-Hill, New York, 1992.
187. T.W. Lewis, G.G. Wallace, C.Y. Kim, and D.Y. Kim, *Synth. Met.*, 84 (1997) 403.
188. T. Osaka, T. Momma, S. Komaba, H. Kanagawa, and S. Nakamura, *J. Electroanal. Chem.*, 372 (1994) 201.
189. J.B. Schlenoff and H. Xu, *J. Electrochem. Soc.*, 139 (1992) 2397.
190. J.M. Pernaut, R.C.D. Peres, V.F. Juliano, and M.A. Depaoli, *J. Electroanal. Chem.*, 274 (1989) 225.
191. B.L. Fletcher, S.T. Retterer, T.E. McKnight, A.V. Melechko, J.D. Fowlkes, M.L. Simpson, and M.J. Doktycz, *ACS Nano*. 2 (2007) 247.
192. M.R. Gandhi, P. Murray, G.M. Spinks, and G.G. Wallace, *Synth. Met.*, 73 (1995) 247.
193. M.J. Madou, *Fundamentals of Microfabrication: The Science of Miniaturization*, 2nd ed, CRC Press, New York, 2002.
194. M.J. de Boer, H. Gardeniers, H.V. Jansen, E. Smulders, M.-J. Gilde, G. Roelofs, J.N. Sasserath, and M. Elwenspoek, *Journal of Microelectromechanical Systems*. 11 (2002) 385.
195. H. Jansen, M. de Boer, R. Legtenberg, and M. Elwenspoek, *J. Micromech. Microeng.*, 5 (1995) 115.
196. H. Jansen, H. Gardeniers, M. de Boer, M. Elwenspoek, and J. Fluitman, *J. Micromech. Microeng.*, 6 (1996) 14.
197. W. Lang, *Materials Science and Engineering R-Reports*. 17 (1996) 1.
198. S. Tachi, K. Tsujimoto, and S. Okudaira, *Appl. Phys. Lett.*, 52 (1988) 616.
199. H. Seidel, L. Csepregi, A. Heuberger, and H. Baumgartel, *J. Electrochem. Soc.*, 137 (1990) 3612.
200. A. Bensaoula, A. Ignatiev, J. Strozier, and J.C. Wolfe, *Appl. Phys. Lett.*, 49 (1986) 1663.

Vita

Benjamin Luke Fletcher was born on October 20th, 1980 in Indianapolis, Indiana to Charles Dean Fletcher, a logistics officer in the US Army, and Kum Soon Fletcher, an accountant at the US Forest Service. Charles Fletcher's professional responsibilities took the Fletcher family around the World. Ben attended his first years of school in Pusan, South Korea before finishing elementary school in Chester, Virginia. For middle school, Ben was a student at the American International School of Rotterdam in Rotterdam, Holland before transferring to the American School of the Hague in Den Hague, Holland. He finished his secondary school studies at Cleveland High School in Cleveland, Tennessee.

Ben majored in Computer Engineering at the University of Tennessee, obtaining his Bachelor of Science in May of 2004. He then enrolled in the Materials Science and Engineering graduate program at the University of Tennessee. Ben completed his dissertation research under the advisement of Michael Simpson and Mitchel Doktycz as a member of the Molecular Scale Engineering and Nanoscale Technologies research group at Oak Ridge National Laboratory. He earned his Ph. D in Materials Science and Engineering in May of 2008. Ben currently resides in Cleveland, Tennessee.